CRANFIELD UNIVERSITY

AIKATERINI PSARRA

GAS TURBINE SHAFT FAILURE MODELLING
FRICTION AND WEAR MODELLING OF TURBINES IN CONTACT

SCHOOL OF ENGINEERING
Department of Power and Propulsion

PhD
Academic Year: 2007- 2010

Supervisor: V.Pachidis/ R.Singh
December 2010

CRANFIELD UNIVERSITY

SCHOOL OF ENGINEERING
Department of Power and Propulsion

PhD Thesis

Academic Year 2007- 2010

AIKATERINI PSARRA

Gas Turbine Shaft Failure Modelling
Friction and Wear Modelling of Turbines in Contact

Supervisor: V.Pachidis / R.Singh
December 2010

Abstract

A possible shaft failure event can trigger a number of mechanisms affecting the mechanical integrity particular of turbine discs and blades. A predominant aim in engine design and development is to satisfy that passenger lives are not to be endangered by the release of high energy debris. In a typical Intermediate Pressure shaft failure scenario of a 3-spool high bypass ratio turbofan engine, a potential mechanism to limit the terminal speed of the free running turbine, within acceptable values, is proven to be the impact of the free running turbine with the following stationary arrangement.

In the presence of the rapid development of affordable computer technology, the implementation of finite element analysis solver is provided to be an efficient tool in simulating dynamic impact between turbines following a shaft failure. This project aims to introduce a new methodology to predict terminal speed based on mechanical analysis. This methodology explores the effect of structure interaction and energy dissipated as friction between free running turbine and the surrounding stationary arrangement (nozzle guide vanes and seal segment) on the evolution of shaft failure event.

In the view of deriving a modelling approach capable to predict the behaviour of the free rotor, extensive parametric studies were carried out in demand of exploring finite elements' tool capabilities to simulate the severe impact between turbines. Since no turbine interaction analysis has been reported in the past, these studies contributed in the research area and provided 'learn how' techniques. These studies highlighted the importance of conducting coupled thermal-structural analysis in order to attain wear of the structure due to the dissipation

of frictional energy into heat. The mass loss derived from high interface stresses and temperature gradients determines the time required for the seal segment to melt away leading to blade tangling and affecting, subsequently, rotational speed. In parallel with the parametric analysis, a number of impact studies simulating the interaction between a target and a penetrator were compared with data in public domain to provide a feedback on the importance of input parameters and confidence in distinguishing variety of computational errors.

The main obstacle of the finite element analysis is the excessive computational requirement in modelling turbines' interaction. Although, computational times are not restrictive considering the continuous evolution of computer's capabilities, a generic simulation strategy of turbines' structural interaction would tackle the constraint of time and power, while it has the potential to be integrated into a multidisciplinary tool. In the light of this, special attention was drawn on the development of a geometry based model which combines LS-DYNA simulations of steady input conditions and a numerical model of structural dynamics equations. This approach provides the capability to capture possible discontinuities, to be easily coupled with other available models and to be applicable to other engine geometries without involving huge computational effort during certification test.

Acknowledgements

First of all, I would like to express my gratitude to my supervisors Dr. Pachidis and Prof. Singh, for their continuous support, in every aspect, over these three years.
I would, also, like to thank A.Rowe, S.Brown and R.Tunstall for all the technical meetings we had and the MSc students that have worked closely with me in the past years and made this project a success:

- Paolo Cappozzi
- Irune Rojo
- Alex Aviles
- Ramon Pardo

I feel really lucky for meeting certain people during my stay in Cranfield and I would like to say a big thank you to them for all the good moments.

My special gratitude goes, of course, to my family and Georgios for supporting me all of these years.

Contents

List of Figures

List of Tables

Nomenclature

Acronyms

EOS	Equation of State
FAR	Federal Aviation Regulations
FBO	Fan Blade Off
FE	Finite Element
FEA	Finite Element Analysis
GE	General Electric
HBR	High Bypass Ratio
HP	High Pressure
HPC	High Pressure Compressor
HPT	High Pressure Turbine
IP	Intermediate Pressure
IPC	Intermediate Pressure Compressor
IPT	Intermediate Pressure Turbine
LP	Low Pressure
LPC	Low Pressure Compressor
LPT	Low Pressure Turbine
NGV	Nozzle Guide Vanes
$Non-D$	Non-dimensional
VSV	Variable Stator Vanes
$2D$	Two Dimensional
$3D$	Three Dimensional

Symbols

A	Area, $[m^2]$

A	Material Constant
a	Thermal Diffusivity, $[\frac{m^2}{sec}]$
B	Material Constant
C	Material Constant
C	Wear Coefficient
C_0	Polynomial EOS Constant
c	Specific Heat, $[\frac{J}{kg \cdot K}]$
D	Fracture Ratio
D_1	Fracture Constant
D_2	Fracture Constant
D_3	Fracture Constant
D_4	Fracture Constant
D_5	Fracture Constant
E	Energy, $[Joule]$
F	Load, $[N]$
FD	Dynamic Friction Coefficient
H_o	Material Hardness, $[Pa]$
I	Moment of inertia, $[kg \cdot m^2]$
k	Interface Stiffness
k	Thermal Conductivity, $[\frac{W}{Km}]$
K	Material Bulk Modulus, $[Pa]$
l_b	Linear Diffusion Distance, $[m]$
$\dot{Q}$	Frictional Power, $[W]$
$\dot{q}$	Heat Generation Rate, $[W]$
r	Radius, $[m]$
r_o	Nominal Radius, $[m]$
SE	Sliding Energy, $[Joule]$
T	Temperature, $[K]$
T	Period of Oscillation, $[sec]$
$T_{applied}$	Applied Torque, $[Nm]$
T_{driv}	Driving Torque, $[Nm]$
t	Time, [s]
u	Rotational Speed, $[\frac{rad}{s}]$

v	Relative Sliding Velocity, $[\frac{m}{s}]$
V	Volume, $[m^3]$
W	Wear Rate, $[\frac{m^3}{m}]$
x	Spatial Variable, $[m]$
y	Spatial Variable, $[m]$
z	Spatial Variable, $[m]$

Subscripts

b	Bulk
$crit$	Critical
cum	Cumulative
$driv$	Driving
f	Friction
fin	Final
$fric$	Frictional
in	Initial
j	Iteration variable
m	Melt
N	Normal
n	Normalised
p	Plastic
S	Shear
t	Blade Tangling

Superscripts

pl	Plastic
f	Failure
$*$	Equivalent

Greek

β	Hardening Constant
$\dot{\epsilon}$	Equivalent Plastic Strain Rate
η	Coefficient
μ	Friction Coefficient
ξ	Damping Ratio

μ	Friction Coefficient
π	3.14159265
ρ	Density, $[\frac{kg}{m^3}]$
σ	von Mises Tensile Flow Stress, [Pa]

1

Introduction

The prevention of primary failure, particularly of the type that may lead to the release of high energy debris, has always been a predominant aim in engine design and development. Figure 1.1 illustrates an example of non-contained engine failure on an American Airlines 767 that occurred during a ground maintenance test run. The HPT stage one disk of GE CF6-80A2 broke into several pieces; however there were no reported injuries.

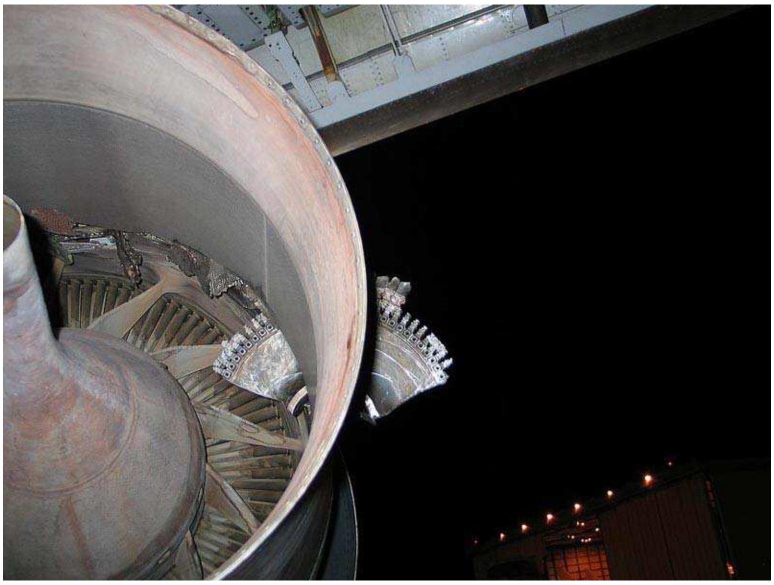

Figure 1.1: AA 767 engine failure(1)

Although, in the past, only a small percentage of aircraft accidents have been accompanied with uncontrollable release of energy adequate to cause non-containment failure, a degree of risk of this type of failure continues to exist. This risk is related to the structure of gas turbine engines which involve high energy rotating masses surrounded by lightweight casings.The idea of designing a casing strong enough to contain the highest energy fragments would result in an unacceptable engine weight with the consequent drawbacks in engine performance and increased loads in the engine mountings. Nevertheless, this option is contrary to today's demand for even higher engine efficiency and lower weight.

The development of aero gas turbines demands a rigorous effort to prepare and integrate computational models and hardware, generate analysis results and post process data in order to assess the operational safety of the machine and generally its airworthiness. Proving the mechanical integrity of an aero engine under various nominal and non-nominal operating conditions is crucial for satisfying safety and reliability requirements.

The interest of the current project is focused on some particular shaft failure scenarios of modern 3-spool HBR engines, in which the arrangement of shaft bearings allows the axial displacement of the IPT. The result of the turbine's axial dislocation is the contact interaction with the following surrounding stationary structure (nozzle guide vanes and seal segment). This interaction may assist in slowing down the rotational speed of the free turbine through blade tangling avoiding in this way rotor overspeeding and any possible release of high energy fragments.

1.1 Project Background

The development of gas turbine technology is evolving continuously the last decades. Engine manufacturers attempt to demonstrate advanced engine models which successfully pass the certification process. During the certification process,the engine manufacturer must successfully demonstrate that, in any shaft failure scenario, an engine can reduce the power of the free running turbine as quickly as possible. This can be succeeded by either a rapid and non recoverable rundown in stall or destruction of the compressor or turbine blading. However, in the lack of the aforementioned events, fuel flow change, variable geometry and bleed settings play a significant role in the reduction of the power of the free turbine.To avoid overspeed conditions, desirable techniques and design features in the engine are to be employed in different shaft failure scenarios.

In the case of 3-spool large turbofan engines, there are different acceptable paths for the avoidance of overspeed conditions in the event of shaft failure. The intention of this project is to focus on a possible scenario of a shaft failure in the intermediate pressure shaft and analyze the effect of a possible structural impact between the free turbine rotor and the following stationary arrangement in preserving the free rotor rotational speed within acceptable limits.

Certification process of 3-spool turbofan engines indicates that, in the extreme case of a intermediate pressure shaft failure, the axial displacement and impact of the free rotor with the following low pressure nozzle guide vanes may act as a braking force on the free rotor by means of converting kinetic energy into heat dissipation between structures. Providing a complete description of the event, when shaft breaks, the free turbine becomes axially dislocated due to the loads arising from the core gas flow and the dynamics of the secondary air system. As a consequence, the free turbine is axially displaced downstream with subsequent mechanical interaction between the rotor and the surrounding stationary structure (NGVs and seals). In this case, the frictional energy that is dissipated between the structures may have a critical effect on the evolution of the event. Quick wear propagation of the seal segment leads to a consequent blade tangling which is possible to cause a significant increase in the frictional energy, affecting the maximum rotational speed attained by the IPT.

Figure 1.2 illustrates an artistic 2D image of the rotors and stators, however the scale of the dimensions correspond to those of a real turbofan engine. It is noticeable that the distance between the IPT and the structure of the NGVs is adequate short to justify an abrupt impact in a few milliseconds after the shaft break. The first structure interaction is to occur between the lock-plate of the disc and the seal segment of the stationary arrangements. The impact takes place under high load and rotational speed conditions and encourages the increase of temperature on the contact interfaces resulting in melt wear of the seal segment. After the structural damage of the seal segment and the vane platform, the blade tips of the free running turbine are going to come in contact with the NGVs' tips leading to high load on surfaces and ,as a consequence, material deformation and possible failure. The speed of the wear propagation is considered to be a determinant factor of the prediction of the timing of blade tangling.

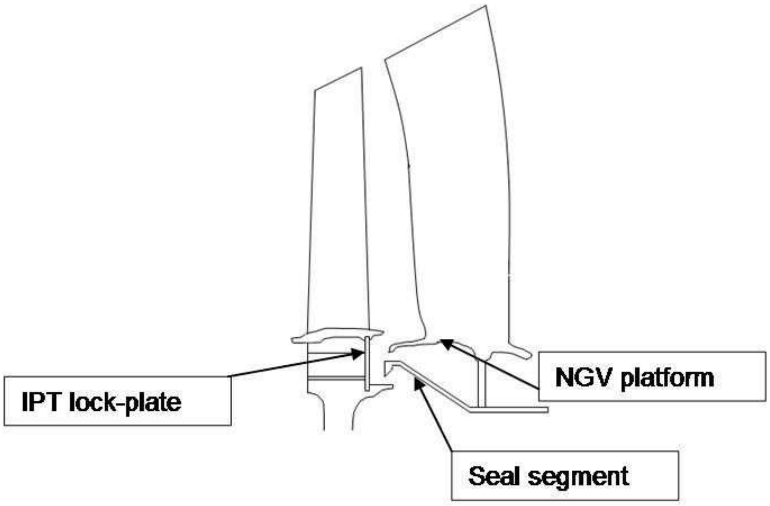

Figure 1.2: Schematic of the IPT and the NGV structure

To fully understand and capture the dynamics of the impact event, it is vital to develop a high fidelity simulation tool that can be efficiently integrated in a multidisciplinary tool able to investigate the aero-thermodynamic performance of the engine. In-house industrial software is available that has the potential to provide prediction of the rotational speed accounting for the effects of structural interaction. Nevertheless, nowadays, the development of finite element codes provide the capability to investigate the impact between turbines using an accurate representation of the 3D structure. Within the benefits of the FEA achieved in the investigated case are the accurate representation of pressure and temperature distribution as well as the evolution of wear propagation and the occurrence of material failure/fracture.

1.2 Project Objectives

Although, FEA solvers have been extensively used in modelling the fan failure event, there is no comprehensive investigation on the turbine interaction following a shaft failure event. This project thesis aims to provide a better understanding of the severe impact of turbine rotor on following static structure and to quantify the effect of heat dissipation and wear propagation on the rotational speed and consequently power of the free turbine rotor. In achieving this aim it is hoped that advanced design rules can be established for future engine designs to prevent any undesirable release of high energy debris. A number of key objectives have therefore been established to achieve this target:

1. Design and build the FE models of turbines in contact
2. Successfully apply a modelling approach able to quantify heat dissipation and wear propagation.
3. Conduct an extensive parametric analysis on the FEA models
4. Distinguish the most vital factors that have an influence in frictional work and melt wear and ,as a consequence, in rotational speed of the free running turbine rotor and occurrence of blade tangling, relatively.
5. Quantify the effect of the most vital parameters and represent them in a non-dimensional form.
6. Develop non-dimensional maps which can indicate friction power and material wear rate with respect to dimensionless axial pressure (load) and relative sliding speed.
7. Establish a generic numerical tool which can implement the maps derived for high-fidelity FEA models to derive the friction torque, rotational speed, mass loss and axial displacement of the turbine.
8. Interpret map based numerical model with respect to real engine data

1.3 Thesis Structure

This thesis is divided into 8 chapters, with each chapter consisting of several sections and subsections.

The second chapter 'Literature Review' contains the findings of a literature research that has been conducted on shaft failure background and applicable methods.It starts with the description of shaft failure event for every shaft in a three-spool high bypass ratio turbofan. It continues with a discussion on finite element analysis implementation on gas turbine components and concludes with an insight on the fundamentals of friction and wear mechanisms.

The third chapter 'Modelling Approach and Methodology' presents the method that has been chosen for the study of the turbines-in-contact event following a shaft failure. It starts with the description of the simulation strategy using a commercial non-linear finite element package (LSDYNA), and continues with the creation of high fidelity three-dimensional models. Such models have been developed for mechanical but also thermo-mechanical analysis of the impact of lock-plate on seal segment. Finally, the chapter includes the description of the development of models for the blade to vane interaction.

In the fourth chapter 'Generic Modelling', the development of a novel map-based method for assessing the effect of lock-plate/seal segment interaction on turbine rotational speed, wear rate and axial displacement. Of particular importance is the generic nature of such method, due to the implementation of non-dimensional maps, the derivation of which, is, also, described in this chapter. The chapter concludes with the description of the suggested numerical model that allows the design engineer to have an initial assessment at preliminary design stage (WENSAT).

The fifth chapter 'Process of Result Evaluation' examines the applicability of the chosen commercial package and boundary conditions on the scientific problem that this thesis is focused on. Due to lack of experimental data, two different studies that bear common characteristics with the turbines-in-contact event have been undertaken. In the first case, the method has been successfully validated against experimental results from a pin-on-disc scenario. On the second case, the method has demonstrated its ability to accurately predict a ballistic scenario.

The sixth chapter 'Wear Propagation' details the generation of the non-dimensional wear maps, as a result of several numerical experiments with the use of LSDYNA code. The effect of the main map parameters, such as axial load and rotational speed, is analysed in addition to additional parameters, such as friction and collision.

The seventh chapter 'Discussion' presents and analyses the main findings of this research study. It starts with the results of the Wear Estimation Numerical Structural Analysis of Turbines in Contact (WENSAT). The results show a close agreement to industrial results, for the engine A which is called base case while the engine B commands the integration with SAS in order to capture the dynamics of the impact event. Several scenarios are analysed, including the effect of friction, geometry and impact.

Finally, the eigth chapter 'Conclusions' includes a general discussion on the results of this project. Additionally, recommendations for further improvement are listed and discussed in depth.

2

Literature Review

A concise review of published work related to the investigation of turbines in contact is presented in this chapter. The literature review is structured into the following three key areas of interest which are identified to be linked to the main objectives of the research activity:

- *Shaft failure scenarios*: A comprehensive review of the shaft failure scenarios is reported emphasizing the case of the IP shaft failure.
- *FEA studies on gas turbine components*: This part of the review discusses the broad use of the commercial FEA codes to analyze structural interaction within a gas turbine engine as a result of components' failure. The FEA solver is also presented and some basic features are reported.
- *Friction and wear mechanism analysis*: This section has a discussion about friction and the wear mechanism. It presents the parameters affecting the tribological process, as well as the wear mechanism. In addition, a short reference in empirical and physical models capable of capturing wear propagation is included.

The chapter concludes by summarizing the contribution of commercial computational codes in structural dynamics and impact phenomenon and the contribution of FEA in this particular research activity.

2.1 Shaft failure scenario

In the event of a shaft failure, the compressor and the turbine are mechanically decoupled resulting in a sudden acceleration of the turbine. If no action is taken to decrease the power of the free running turbine, it is imminent to achieve overspeed condition with a possible release of high energy debris. Therefore, in such cases, a predominant requirement is to decrease the power of the free turbine rotor within acceptable limits as quickly as possible.

In modern 3-spool HBR turbofan engines, failure is possible to occur in any of the shafts, HP, IP or LP. However, in every failure scenario, the behavior of the engine varies and, thus, different patterns are followed in order to avoid overspeed conditions. This subsection aims to provide a brief overview of the every shaft failure scenario concentrating the attention on the case of IP shaft failure.

2.1.1 HP shaft failure

This event can be extremely hazardous, because the HPT is the one that keeps its pressure ratio for the longest period of time. In a three spool engine in fact, the turbine system will unchoke starting from the low pressure stage. Therefore, it will take a while before the pressure ratio across the HPT drops to a sufficiently low value.

The consequences of a failure of the HP shaft of an engine are very much dependent on its geometric characteristics. The destruction of the HP compressor or turbine blading could be the key in attaining acceptable terminal speed.

Desirable design features assisting in limiting the rotational speed are the lack of bearing between the compressor and the turbine and the absence of static seals bearing the rotating parts of the HP shaft system between connection at the compressor and the turbine end. These features encourage the existence of blade tangling between structures which can be considered as a prevailing mechanism for the destroy of the blading.

2.1.2 LP shaft failure

This is considered to be the most common form of the shaft failure. In most of the engines, the LP location bearing enables the axial displacement of the turbine and therefore the blade tangling is inevitable due to the closely spaced blades and stators.This failure scenario tends to lead to a non-contained debris in the absence of fuel shutoff devices.

To achieve an acceptable terminal speed the fuel flow must be quickly shut off and the mass flow through the engine has to be sharply reduced. There are some desirable features that can assist in limiting speed:

- *Low design loading.* This implies a low value of the loading parameter $\Delta H/U^2$, although this is in contrast with the demand of high LPT loading in modern engines.
- *Low ratio of core spool to LPT kinetic energy.* The core spool slows down quicker than the LP spool accelerates, after fuel shut off, thus allowing a quick reduction in mass flow through the LP turbine.
- *Movement of bleeds and variable stator vanes.* If this is included in the control system, then it enables the reduction in the mass flow and the pressure ratio of the LPT.
- *Low design pressure ratio.* Since a relatively low pressure ratio can keep the LPT well above its design speed, it is desirable to reduce as much as possible the pressure ratio at design point.

A feature of this case is that most of the times it is suggested to design the LPT capable of withstanding the overspeed condition, since the LPT disc is not usually designed at its maximum strength and is relatively easy to increase it. In this case, however, the control system must be able to stop the LPT. Blade tangling is another reasonable option to avoid overspeed. This is aided by the fact that the LP shaft is usually mounted in a way that a shaft failure results in a loss of the LPT axial position. This will greatly ease blade tangling. Nevertheless, fuel shut off and mass flow reduction should always be allowed, in order to avoid excessive and dangerous uncontained debris.

2.1.3 IP shaft failure

IP shaft failure event tends to be a challenging condition basically because it is yet to be investigated in depth. When an IP shaft failure event takes place in order to avoid undesirable situation such as release of a whole blade set to the turbine casings, the turbine rotational speed should be limited to an acceptable terminal speed (: maximum speed the turbine should attain). There are three acceptable ways of eliminated turbine speed:

- *Engine surge and no recovery.*: This scenario tends to be the most desirable since it results in a safe rundown of the engine. This scenario is likely to occur in the case of the shaft failure event, where there is residual vibration due to ultimate failures of the shaft. The vibration leads the compressor to surge while it prevents the recovery from surge. A quick modification of the thermodynamic matching can also be beneficial avoiding the engine from recovering, regarding that the engine has run out of surge margin a the time of surge recovery.

- *Engine surge and recovery, second surge controlled by thermodynamics.*: This scenario actually occurs in the case of reasonably 'clean' failure caused probably by an oil fire.In this event, the engine recovers from the first surge and the second surge needs to occur rapidly enough. The recovery from the second surge is not controllable by the residual vibration and therefore, the thermodynamics plays its role. In theses scenarios, the rapid VSV closure and IP bleed valve opening are considered to be helpful factors. A low ratio between the IPC and the IPT inertia is considered to be beneficial since the IPC inertia determines the compressor rundown and the decrease in engine mass flow, while the IPT inertia will determine the turbine acceleration.

- *Engine surge and recovery, second surge controlled by blade tangling.*: Heavy contact between the IP turbine blades and some static structure behind them particularly a set of nozzle guide vanes is possible to lead to a violent shedding of the blade tips. The vibration pulse caused by this event is large enough to induce HPC surge. Furthermore, a residual vibration due to the out of balance turbine is large enough to prevent recovery. The turbine blade tangling is a desirable condition before the engine recovers from the surge. The viability of this mechanism to limit turbine power depends on the axial load behavior of the engine.

Concluding, the progress of the event and the limiting of the terminal speed are significantly connected to the effectiveness of particular design features. The desirable features that are likely to limit terminal speed and satisfy a safe failure progression are included to the following:

- ’Dirty’ break giving high level of residual vibration
- A relatively low ratio of IP compressor to turbine inertia (promotes timely HPC surge)
- Rapid opening of core bleed valves and closure of VSVs (promotes HPC surge)
- High Fuel Flow (promotes HPC surge)
- Low mass of metal between IPT rotor and LP1 NGV (promotes rapid tangling)

The aforementioned IP shaft failure is based on the analysis of the turbine shaft failure.Except for the turbine shaft failure, it is possible to have stubshaft failure, where the turbine remains in its position and basic mechanism to obtain acceptable terminal speed is either a quick modification of the thermodynamic matching or an induced compressor surge by means of residual vibrations. Lastly, there is also the scenario of the spline coupling between the compressor and the turbine where the first surge does not necessarily occur.

The focal point is the case of a IP turbine shaft failure and, in particular, the case when the turbine is allowed to move rearwards and interact with the following static arrangement.Moreover, the analysis is based on some engine data available from an IP shaft failure event, occurred during a Rolls-Royce engine development. The failure occurred during the development of the engine and the collected data have been reported in (2).

2.1.4 Shaft failure events during engine development

Shaft failure tends to be a challenging problem, which combines a number of complex dynamic phenomena. The prevailing requirement is to reduce the power of the 'free turbine' within acceptable limits as quickly as possible. In order to satisfy this requirement, it is essential to ensure either a rapid and non recoverable rundown in stall or destruction of the compressor or turbine blade tangling. The analysis of shaft failure events needs to account for fuel flow, variable geometry, bleed settings and the secondary air system dynamics, which play a significant role in the gas turbine engine operation under severe conditions as shaft failure.

During engine development tests, two accidental shaft failure events occurred and contributed to the understanding of the events. A picture of the events is included providing evidence from hardware, dynamic vibration and transient performance data. These events are used as a background for the investigation of turbines' clashing.

2.1.4.1 Engine A shaft failure analysis

During a development test, the engine suffered an ultimate failure on the first fuel strike at maximum power leading to a surge and finally the engine ran down safely in stall, showing no sign of recovery. After the shaft failure, the free rotor moved rearward and there was an evidence of severe impact between the rotor and following stator.

It is evident in Fig.2.1 that there were signs of axial displacement of the IP turbine. Figure 2.1depicts a 2D schematic of the failure on turbine stages observed after the axial displacement and the impact. Firstly, the LPNGV inner platform and the seal segment melt away by the IPT lock-plate due to high load and relative velocity impact. The IP surface temperature is of the order of 1000 K leading to melt wear due to the existence of excessive values of temperature and load. When part of the mass of the seal segment and platform melts away, the IP turbine is free to move further rearwards forced by the gas pressure difference. The outcome of the further IPT displacement is the contact interaction between blades and vanes damaging trailing and leading edges, relatively.

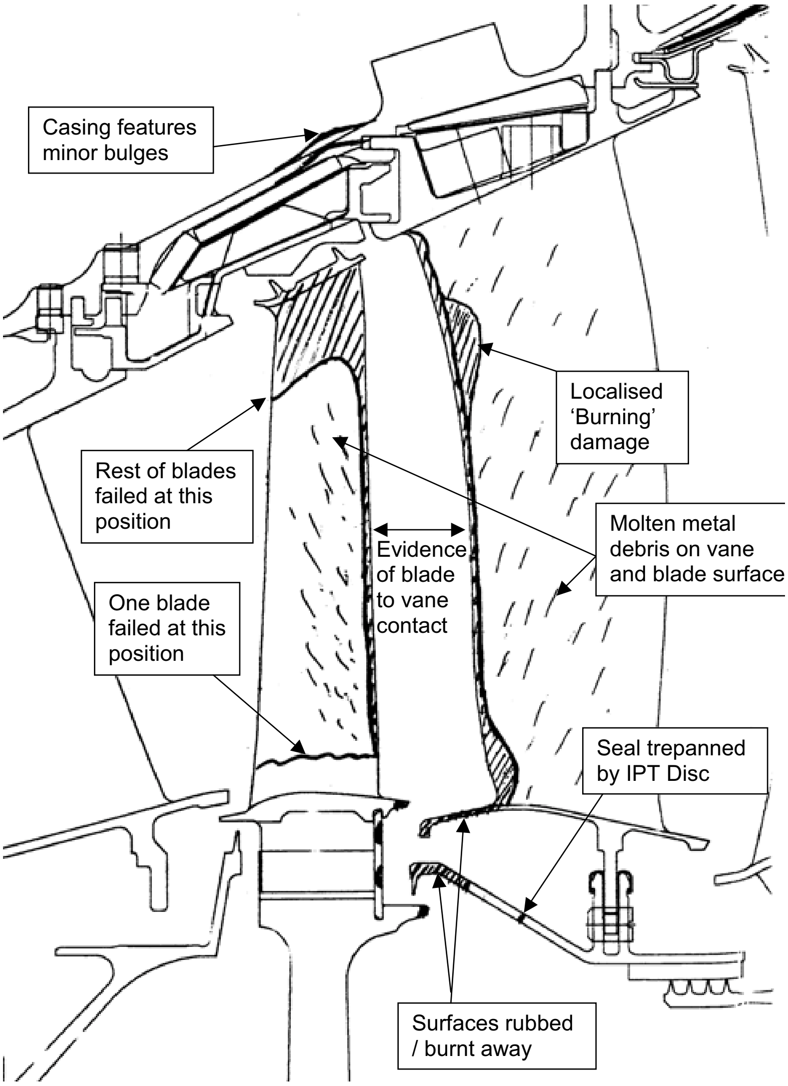

Figure 2.1: 2D schematic of the turbine stages after shaft failure(2)

Even though blade tangling decreases turbine power through the dissipation of friction energy, it is not the only factor assisting in attaining acceptable terminal speed. The vibration of the turbine is considered as significant parameter which causes engine surge and the presence of a high vibration level for sufficient time could be act as a check on the recovery from surge.

The vibration history is depicted in Fig.2.2. Immediately after the shaft failure the signal is flat because the sensors are out of range due to violence of the event. When the signal becomes available again is the IPC that makes itself visible. This vibration tends to decay with time, until another big event happens. As indicated in Fig.2.2 the new signal, whose frequency is close to an HP order, is due to the IPT that now is unbalanced because of blade tips failure.As indicated in Fig. 2.2 the new signal, whose frequency is close to an HP order, is due to the IPT that now is unbalanced because of blade tips failure. Vibrations have a direct impact on the surge margin of the HPC. In particular, the vibration level influences the tip clearance and the latter influences the surge margin. An IP order vibration of 1/sec will erode, roughly, 7% of the HPC surge margin, while an HP order vibration of the same amplitude will erode 10% of the HPC surge margin. If the level of vibration is sufficiently high to consume the 30% surge margin of the HPC at the end of the first surge blowdown cycle, then the engine will not recover from surge. In the case of engine A, the vibration level is estimated as 17/sec, high enough to prevent recovery from surge.

The aforementioned discussion on the outcomes of turbines in contact needs to be connected to the imposed pressure and its effect on the rotational speed. The axial load applied on the turbine depends on both the gas pressure of the core engine and the pressure applied on the disc of the rotor from the secondary air system. Immediately after the shaft failure, high load is applied on the turbine rotor as derived for the gas path of the core engine and the secondary air system. The load follows a decreasing progress with respect to time. This is an expected reaction due to the decoupling of the turbine from the compressor and the surge of the second one. The decrease of pressure and the increase of rotational speed with time are depicted in Fig.2.3. It is worth to point out that there is a steep increase in rotational speed immediately after the failure followed by an asymptotic behaviour.

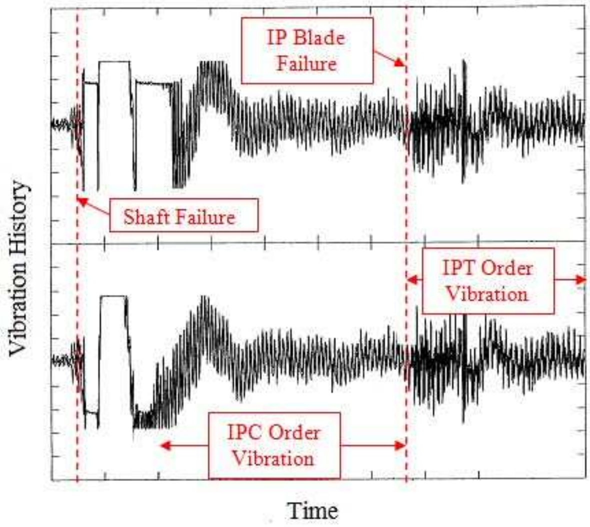

Figure 2.2: Engine A vibration history(2)

Blade tangling is not absolutely necessary to achieve an acceptable terminal speed. Nevertheless it can be an effective solution to avoid dangerous overspeed conditions. A desirable condition is, however, that blade tangling starts quickly enough after the first surge. If blade tangling is to be used as the mechanism for limiting terminal speed, it is necessary to understand what are the factors controlling frictional wear.

The main factor governing the friction between the IPT and LP1 NGV is the axial load acting on the rotor. This is made up of two components, the gas load on the disc and the gas load on the blades. Without considering the effect of the secondary air system (SAS) it could be assumed that the net axial load simply depends on the pressure drop across the IPT. However, if the rotor comes in contact with the LP1 NGV, the pressure inside the LPT cavity can increase. This has a negative effect on the net axial load, since it will decrease to a much lower value. Consequently, the frictional torque on the IPT rotor and the wear rate of the NGV platform and seal are greatly reduced. In such a case blade tangling is less likely to occur. This highlights the importance of the dynamic behavior of the SAS in order to properly estimate the frictional torque. Therefore, the net axial load acting on the IPT rotor is calculated in two different ways. In one case it is assumed that the IPT cavity is not sealed (F crude), and in the other that the cavity is sealed (F net) by the rearward movement of the rotor. The resultant axial loads are reported in Fig. 2.4.

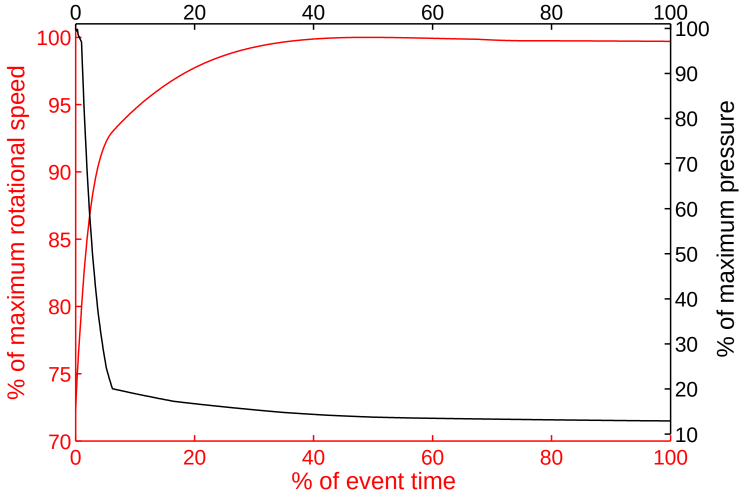

Figure 2.3: Change of pressure and rotational speed with time after the shaft failure(2)

Based on these loads it is possible to derive the frictional torque and also the energy dissipated by friction during the contact. The frictional energy absorbed during the impact is calculated multiplying the current axial load by an empirical friction coefficient, by the mean radius of the IPT stop ring. The comparison of the different results is shown in Fig.2.5. The graph includes also information about the point where blade failure occurred, since it is known that at the time of blade failure at least that quantity of energy was absorbed to melt the NGV platform and seal. Looking at the results it appears that the unsealed cavity assumption aligns better with the known value of energy absorbed at the moment of blade failure.

2.1.4.2 Engine B shaft failure analysis

In engine B, there was detected heavy shooting in the LP turbine cavity as a consequence of the oil fire which caused the shaft failure. There was a axial displacement of the free rotor and the area around the IPT blades had similar

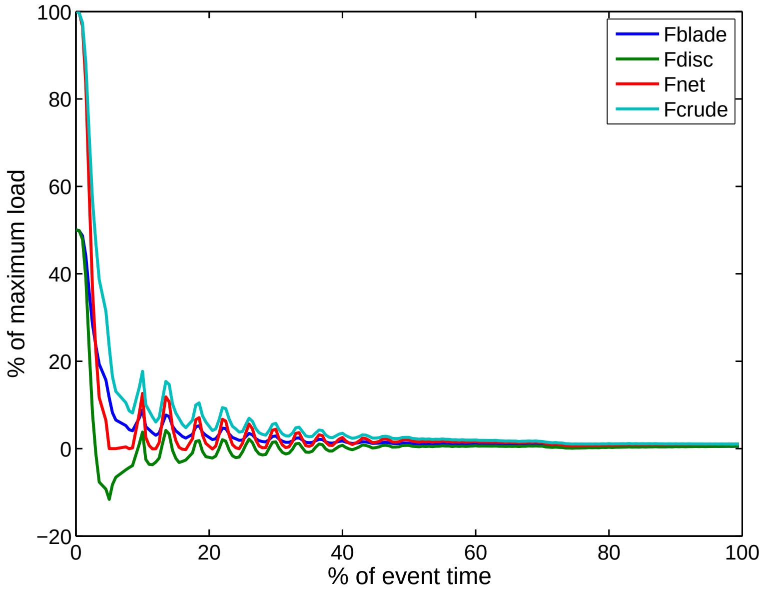

Figure 2.4: Axial loads applied on the IP turbine after the shaft failure(2)

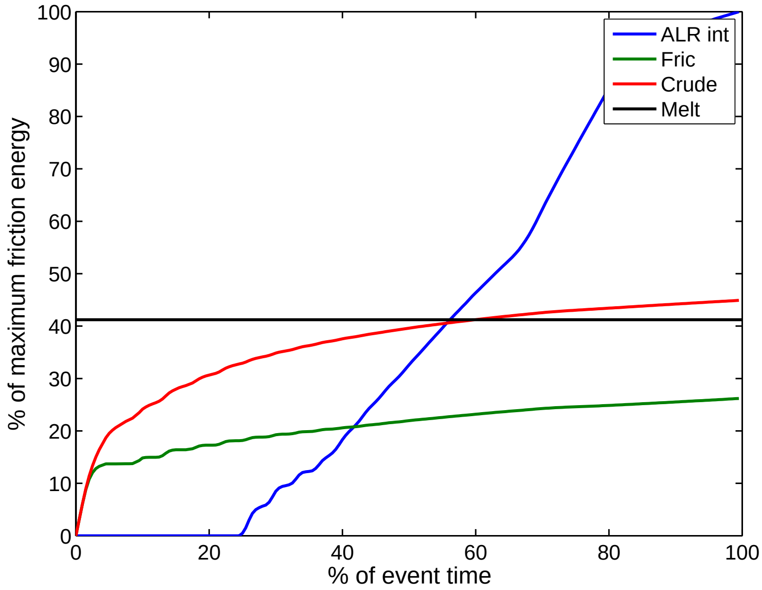

Figure 2.5: Comparison of frictional energy dissipated due to failure,Fric:LPT cavity sealed,Crude:crude friction sum, ALRint:friction energy as deduced from speed and gas torque, Melt: energy absorbed to melt static structure(2)

pattern of damage with engine A, although the tangling in the particular case was more violent.

In engine B, little residual vibration was detected from the engine components,as shown in Fig.2.6. The lack of residual vibration have facilitated the HP compressor to recover from surge and run stably for a period of time until the thermodynamic conditions in the engine result in the occurrence of a second surge.

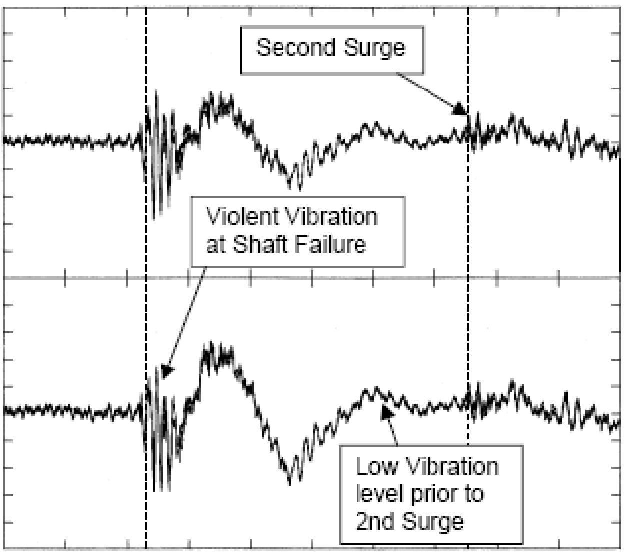

Figure 2.6: Engine B vibration history(2)

The tendency of gas turbine to recover from surge is related to the geometrical and aero-thermal features. The response of engine B is more 'typical' compared to engine A because the engine was running steadily before the shaft failure occurred.

The rearward movement of the IP turbine disc would seal the LPT cavity causing an increase in turbine capacity. This action leads to a pressure rise and further to a reduction in the axial load on the turbine disc. It is possible the pressure rise to provoke a reduction in the axial load to such an extent that it can nearly overcome the blade load. It is apparent that this event causes an elimination of the frictional wear rate of the rear static structure. Blade tangling has a positive effect on controlling terminal speed, therefore any action that could eliminate this phenomenon, needs to be prevented. Any tendency of the disc to move forward would result in opening the seal and equalizing the pressure with the pressure with the gas path.

The load acting on the free turbine is depicted in Fig.2.7 while Fig.2.8 presents the energy consumed as heat with time. The point of blade failure appears to be estimated with the friction energy when LPT cavity is sealed. The unsealed case overpredict the the amount of friction energy of about one third.

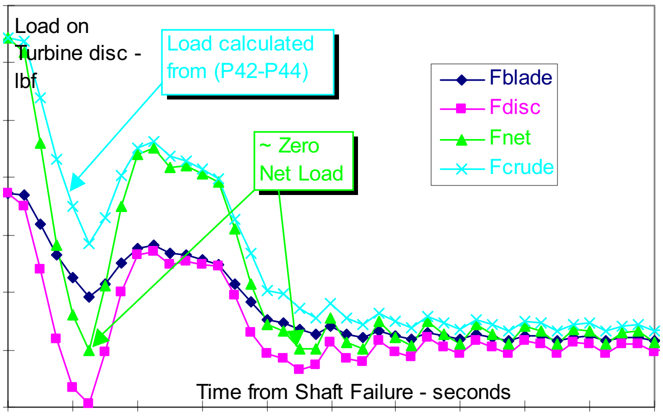

Figure 2.7: Axial loads applied on the IP turbine after the shaft failure

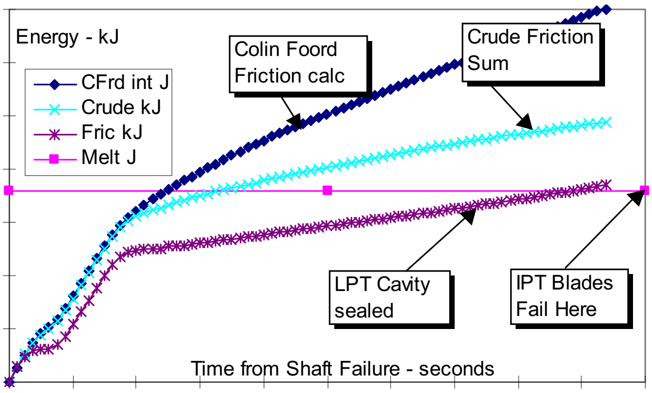

Figure 2.8: Comparison of frictional energy dissipated due to failure,Fric:LPT cavity sealed,Crude:crude friction sum, CFRint:friction energy as deduced from speed and gas torque, Melt: energy absorbed to melt static structure(2)

2.1.4.3 In-house industrial code for the prediction of shaft failure events-BD29

BD29 is a simple turbine only model developed at the time of the above engine failures. It is based on matching engine measurements of pressure and temperature. ad calculated turbine speed with HP compressor delivery pressure as the primary driving torque. Allowance is made fore the effect sf axial load , friction energy, axial movement of the turbine and hence efficiency losses.

2.2 Implementation of FEA on gas turbine components

In the past, FEA tools have been extensively employed to capture the dynamics of gas turbine component's failure. FEA tools have proven to be accurate in the prediction of complex dynamic phenomenon. FEA tools are implemented in industry to develop engine's structures able to withstand dynamic impact phenomena. In most cases there are common modeling techniques capable to provide a good estimation compared to the data provided by experimental arrangements.

2.2.1 Fan failure modelling

Fan failure modelling represents a characteristic example of the application of FEA on gas turbine components. Jet engines' manufacturers applied numerical tools in the field of fan containment systems trying to increase confidence and reliability in the design without the demand of costly testing.

In a scenario of a fan blade-out, the loss of a first stage blade in a high bypass turbine engine can be triggered by a bird strike, a foreign object damage or even fatigue. A fan blade-out event is considered as a difficult condition to simulate for the reason that it includes nonlinearities of structural dynamics as behavior of materials, large displacement and severe contact interaction between structural elements. However, modern computing technology provides the capability to simulate these complex events with the development of high fidelity simulation tools like LSDYNA, ANSYS, ABAQUS, NASTRAN. The continuously improvement in non linear finite solvers made them capable to capture the dynamics of the events and to deal with impacts and structures' failure.

Published works in the field of fan blade failure analysis can be distinguished into three different fields.

1. Causes leading to blade release including bird strike or general reported as foreign object damage
2. High impact of transient load generated inside the engine due to structure interaction between the blade fragments and the containment and the blade fragment and the adjacent blades
3. Rotating loads applied on fan rotor due to unbalance

The improvement in the foreign object damage tolerance of engines at the design stage required a methodology to assess the loss of fatigue strength. Prediction of the residual stresses attained from the impact on a compressor blade commanded the use of a damage material model(15). After the analysis on the causes of fan failure, the second step is to investigate the impact between engine fragments and containment aiming at proposing a design of the containment able to avoid hazardous debris.In the view of this, the advantages gained from a development of lighter engines brought in the foreground the use of lighter material in the construction of containment rings. However, the main requirement has always been to guarantee that the material of the containment is strong enough to withstand the possible high velocity fragment. Numerical tools contribute in the simulation of severe impacts and the development of empirical models giving information about the vulnerability of the structure and propose a strategic design for the avoidance of undesirable events.(12, 16, 17)

In terms of rotor-dynamic, the first one to analyse the effect of FBO unbalance in the time domain was Stallone et.al. (18) back in 1983. Cosme et.al. (19) employed an explicit code to analyse the rotor unbalance comparing with test measurements while Shmotin et.al.(20) studied the containment behaviour under unbalance emphasizing on the process of modelling of the interaction between the released blade with the adjacent blades . Carney et al.(21, 22) tried to identify the physics of the blade loss event in correspondence with time dependent trajectory of the lost blade and its impact on the containment structure , the unbalanced rotational dynamics of the remaining fan-rotor system and the rub of the remaining first stage fan on the containment ring due to the unbalance. Heidari et.al.(23) represented a multidisciplinary simulation method to streamline the FBO event based on the implicit fan blade calculations, which are used as initial condition for the initial transient explicit fan calculations on a fine-meshed finite element model. The derived forces are in a further step implemented as loads for a rotor dynamics simulation for much longer time using a coarser mesh. In this way, the mapping of the fan blade-out forces are computed applying a FE code.

2.2.2 Turbine failure modelling

Turbine rotor failure can be an outcome of overheating, birdstrike, blade detachment or even overspeeding. McCarthy(3) was the first who addressed the types of rotor failure analysing the reasons of turbine rotor and summarized the effects of rotor blade fragment, size, weight,energy and momentum on UK engines. According to(3), types of rotor failure leading to non-containment include low and high cycle fatigue, disc material and processing defects, disc overheating due to rubs or loss of cooling air and disc overspeeding due to shaft failure or engine overspeed. Considering rotor failure events happened in the past, large fragments are more prone to damage the aircraft than small ones and the damage tends to be more extensive. However,the release of small fragments is more frequent implying that probability of impact on a vulnerable item in aircraft is increased.

Figure 2.9 depicts a breakdown of non-containments in terms of number of incidents against the maximum dimensions of the largest fragment from the 1954 to 1976. It was reported that in case of turbines the release of small fragments is more often than large. The small pieces include single blades or part blades or small pieces of disc with blades attached. In Fig.2.9, the red areas represent the incidents that caused injuries or affected the airworthiness of the aircraft.

Generally speaking, FE tools have proven to be an accurate and time efficient way to analyze the structural dynamics of turbine blades and discs taking into account stress distribution, friction, impact forces and vibration. During

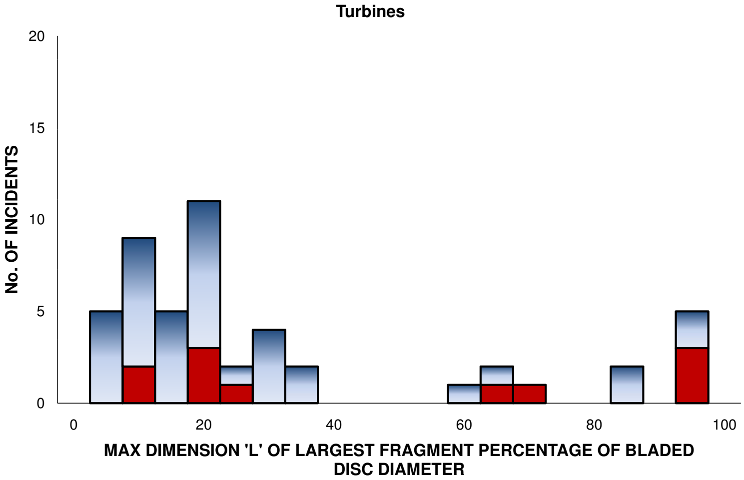

Figure 2.9: Maximum dimension of largest fragment as a percentage of bladed disc diameter(3)

the last decade, numerous researchers tried to develop methodologies to investigate different aspects of turbine failures using FEA solvers. A variety of represented research activities are summarised. Starting with Sarkar et.al. (24) who derived a comprehensive methodology of turbine failure and fragments' impact using a transient nonlinear finite element code. This research covers the effects of multiple collisions among the remaining blades and the rotor fragments on the containment process. The methodology derived provide fair agreement between numerical model and spin chamber experiments in determining the critical ring thickness and the residual kinetic energy levels of the fragment. In the same context, Kraus et.al.(25) highlighted that the fragmentation of the released blades is different when the analysis is performed with or without adjacent and showed the importance of choosing an appropriate material model with a failure criterion. Furthermore, except for the interaction of released blades with surrounding structures, analysis using FE has been conducted in the interest of investigating the damage mechanism of the turbine disc and indicating a few critical regions of turbine operating under excessive rotational speed and their effect on the size of the fragments(14). Last but not least, it is worth mentioning the implementation on numerical tools in developing engine fragment barriers with low added cost and weight(26).

The above mentioned research activities gave confidence about the capability of the computational analysis tools to simulate complex dynamic problems which include severe material interaction with fragments of high temperature. Therefore, the literature review is stated as a focal point in the decision of whether the use of finite element tools can accomplish accuracy of the wear propagation and the estimation of friction/heat dissipation.

2.3 FEA Solver

A large number of commercial codes exist and are implemented successfully to problems involving high damage levels. The computational codes available for dynamic analysis tend to be very complex requiring considerable experience with both the codes and the physical problems(27).

Transferring a physical problem to a discrete model and solving it using finite element code packages is a challenging task. Therefore, knowledge of the approximations of the software and its capabilities is a basic requirement. This implies that a literature survey needs to be accomplished in order to be aware of the software performance in solving the problem, while it will work as a technical foreground for the user.

It is common that compromises need to be decided by the user, however the keen understanding of the physical problem, the effects of discretization on the problem and the effects of numerical artifacts on the solution such as uneven resolution schemes, mixing of implicit and explicit integration schemes, choice of mesh or element type, effects of sliding surfaces of interfaces and the use of various viscosities to stabilize computations can assist in a sophisticated decision making.

The aforementioned selection of the applicability of FEA in impacts caused by fan or turbine failure represent characteristic examples of their use in aero engines. It is of the essence by means of providing ideas and techniques on the modelling approach of structures under high velocity impact with imposed transient loads.

Their contribution encompasses the solution to practical problems such as the structural meshing, the choice of constitutive model and contact algorithm.

The FEA solver used for the investigation is LSDYNA. It is one of the most advanced software for nonlinear structural analysis. It is capable of dealing with very complex phenomena, such as coupled thermo-mechanical simulations. It is very effective and largely used especially in impact and crash analysis, thanks to the advanced contact algorithms implemented and the explicit time integration capability. It has been used over the past 20 years in crashworthiness analysis, bird-strike and fan blade out simulation. The code works with input files, also called decks, that are logically organized.They are made up of several cards, each of them committed to define a particular feature of the model, such as material properties, contact algorithm and so on. Thanks to these features and to the capability of accurately reproducing experimental and test data, this code is proven to be very promising for the current investigation.

2.3.1 Contact and friction modelling

Contact modelling is considered to be one of the most difficult aspects to deal with in nonlinear finite element analysis. In LS-DYNA three different methods to deal with contact are implemented:

- penalty method
- kinematic constraint method
- distributed parameter method

The penalty method is the most frequently used, especially in explicit simulations and it is the one that was used in the analysis. It consists of placing interface springs between nodes penetrating a surface, and the surface itself. In this contact method, a 'master' and a 'slave' side have to be specified, in such a way that these two together encompass all the contacting elements (28). During the calculations, nodes of the slave side are controlled for penetration through a master segment. In LSDYNA, a segment denotes a face or a side of a solid element (4). When such a penetration is detected, a force proportional to this penetration is applied to the slave node. This force is made up of two different components. The first one is normal to the master segment F_N and the other one is parallel F_T as depicted in Fig.2.10.:

- the normal force, which has the effect of compressing deformable solids and corresponds to the sliding energy due to normal penetration of the slave nodes in the master segments,

  $$F_N = k \cdot x \tag{2.1}$$

  where x corresponds to the penetration of a slave node in a master segment and k determines the interface stiffness defined as :

  $$k = \frac{\alpha K \cdot A^2}{V} \tag{2.2}$$

  The above interface stiffness formula involves the scale factor α which controls the interface stiffness, the material bulk modulus K, which is characteristic of the material, the face area of the segment,A and the volume, V, of the element containing the penetrated segment. Both interface area and element volume are affected from the structural features.

- the tangential force, which is the source of sliding energy due to friction at the sliding interfaces and it is non-recoverable, thus it expresses the dissipated heat and is calculated, according to the Coulomb friction formulation,

  $$F_S = \mu \cdot F_N \tag{2.3}$$

  where μ is the friction coefficient defined according to Eq.2.4.

  $$\mu = \mu_{dyn} + \mu_{static} e^{DC|v|} \tag{2.4}$$

  where μ_{dyn} and μ_{static} are the dynamic and the static friction coefficient, DC is the decay coefficient determining how quickly the friction coefficient changes from the sliding to the static value depending on the relative velocity of the two contacting bodies.and v is the relative velocity between the penetrating node and the segment.

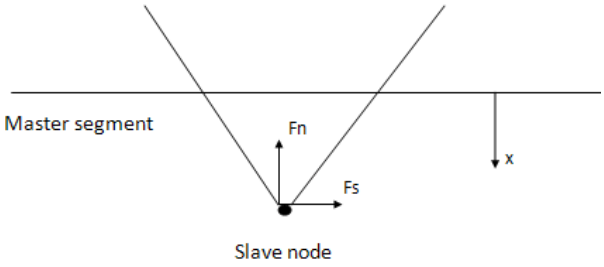

Figure 2.10: Forces due to contact (4)

When two surfaces contact each other, and in particular when relative sliding occurs, the sliding energy (SE) is calculated. The latter is based on the two components of the interface force, and is calculated according to:

$$SE = \int F_N \cdot dx + \int F_S \cdot u \cdot dt \tag{2.5}$$

as reported in (4). The component deriving from the normal force is recoverable since the normal contact is treated as a spring, but the component deriving from the shear force is dissipated. The actual formula used in the code to calculate this energy is (28), where the contact energy E_{SI} is incrementally updated from time n to time $n+1$ for each contact interface as:

$$E_{SI}^{n+1} = E_{SI}^{n} + \left[\sum_{i=1}^{nsn} \Delta F_i^{slave} \Delta dist_i^{slave} + \sum_{i=1}^{nsn} \Delta F_i^{master} \Delta dist_i^{master} \right]^{n+\frac{1}{2}} \tag{2.6}$$

In the above equation, nsn is the number of slave nodes, nmn is the number of master nodes, ΔF_i^{slave} is the interface force between the ith slave node and the contact segment, $\Delta dist_i^{master}$ is the interface force between the ith master node and the contact segment, while $\Delta dist_i^{slave}$ and $\Delta dist_i^{master}$. i are the incremental distances by which the slave node and the master segments respectfully have moved during the current time step. This is an important aspect of contact for the purpose of this analysis.

The last thing to mention about contact is the possibility to include contact damping. This is done with the viscous damping coefficient (VDC) that represents a percentage of the critical damping as shown in Eq.2.7- 2.9.

$$\xi = \frac{VDC}{100} f_{crit} \tag{2.7}$$

$$\xi_{crit} = 2m\omega \tag{2.8}$$

$$\omega = \sqrt{k\frac{m_{slave} + m_{master}}{m_{slave}m_{master}}} \tag{2.9}$$

The contact viscous damping, as reported in (28), can allow for an effective reduction in the high frequency oscillation of the contact force. The viscous damping is included in LS-DYNA mainly for metal forming applications.

2.3.2 Hourglassing

Hourglassing is a common name used in finite element analysis to address the problem of zero-energy mode of deformation. Zero-energy modes of deformations means that an element can be deformed without dissipating energy. One of the most common outcome of this phenomenon is that the structure has no or little stiffness. This problem, however, affects only the elements with a single point integration scheme and the reason for this is quite simple. As observed in Fig.2.11, the vertical and horizontal dotted lines are unchanged after deformation.(29)

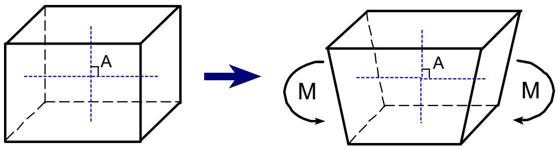

Figure 2.11: Change of shape for under integrated solid elements under bending moment(5)

Point A, which is the only integration point, will therefore not detect any normal or shear stress and no strain energy will be generated(5). A big issue of hourglassing is that it rapidly propagates inside the mesh, especially in the very coarse ones. In order to avoid non physical results, hourglass should be reduced as much as possible. There are three main methods to achieve this objective:

1. refine the mesh, since hourglass is particularly induced when a load is concentrated on few nodes
2. use fully integrated solid elements since, with an 8 points of integration scheme, will not suffer at all from hourglass
3. use on of the hourglass control algorithm available

Apparently, the second option seems to be the best one, since hourglassing will be totally avoided. Unfortunately, fully integrated solid elements may behave too stiffly due the shear locking effect. In fact, it is alway suggested to use single point integration solid elements, especially in impact analysis, and to apply one of the hourglass control algorithms available. There may be some situations where hourglassing is hard to reduce, even with the appropriate control algorithm. Therefore, an optimum combination of the three methods is the best solution(30).

In LS-DYNA there are various hourglass control types. They can be divided in viscous and stiffness forms. The latter adds a small stiffness to each element and the former a viscous damping, both of them with the purpose of stopping hourglass modes of deformation. These modes are orthogonal to the strain calculation and are not included in the energy balance(31). For this reason, the energy spent in reducing the hourglassing will result in a small loss of energy from the system, denoted as the hourglass energy. Consequently, this energy has to be low enough in order to have meaningful results. Usually, results are considered to be acceptable if the hourglass energy is less than the 10% of the peak internal energy.

2.3.3 Non local material

In order to model the contact between the seal segment and the lock plate it is required to use a damage model which will allow simulating the material behaviour and erosion that happens in the real case. References were found about problems encountered when using a damage model, it was reported that different simulations of the same model (6) using relatively coarse mesh provided different results as can be seen on Fig.2.12. It should be noted that in a non linear numerical simulation, which inherently has to use non-exact algebra, i.e. at some point numbers need to be rounded, a slightly different output should be expected from different simulations of the same model with the same software and hardware. For that reason, to reduce this effect, obviously the simulations are done with double precision.

Figure 2.12: Asymmetric results on impact problems(6)

Damage and failure models in finite elements tend to have a mesh size dependency which will require a constant size mesh. But it should be recalled that element size is an important aspect from a numerical modelling point of view as it will affect the computational time, increasing as the element size decreases. When the simulation is a static analysis the number of elements may not be a problem, but when working with non linear dynamic simulations the number of elements (and so the number of nodes) is a variable that must be controlled and variable density meshing is likely to be used. It was also found that the damage tends to be confined on the fictitious boundaries(6).

In order to reduce the effects of the damage localization an optional card is added. This option introduces a function that distributes the damage over a volume, which is defined by the user, so the failure criterion now depends on the state of the material, e.g. strain, within a volume that surrounds the integration point. This is done defining a function $\dot{f}_r$(28):

$$\dot{f}_r = \dot{f}_r(x_r) = \frac{1}{W_r}\int \dot{f}_{local}\,\omega\left(x_r - y\right)dy \approx \frac{1}{W_r}\sum_{i=1}^{N_r} \dot{f}^{i}_{local}\,\omega_{ri}V_i \tag{2.10}$$

$$W_r = W\left(x_r\right) = \int \omega\left(x_r - y\right)dy \approx \sum_{i=1}^{N_r} \omega_{ri}V_i \tag{2.11}$$

where Ω_r is the area of radius L surrounding an element e_r, $\dot{f}_r$ is the nonlocal rate of increase on damage and x_r is the center if the element e_r, $\dot{f}^{i}_{local}$ is the local rate of increase on damage, V_i is the volume and y_i is the center if the element e_i.

A weighting function is calculated in order to obtain the average damage over an area Ω_r. In that way damage will be increased on elements that have neighboring elements with more damage and vice versa damage will be decreased on elements that have neighboring elements with less damage.

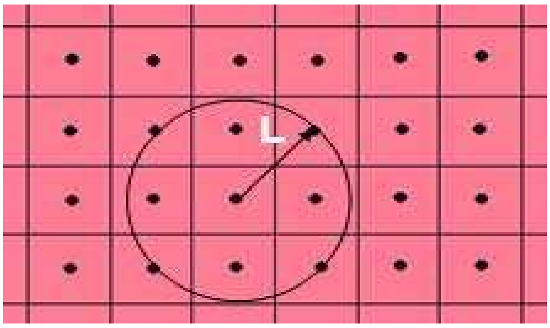

Figure 2.13: Definition of the area radius, L

2.4 Friction and wear Mechanism

Tribological problems are by nature complex, involving complicated mechanical and thermal interactions between the different components participating in the process and between the different components and the environment. Therefore, an efficient way to account for these interactions is to approach the problem from a system's point of view.

Figure 2.4 represents a brief of the energy absorbing processes on pairs of metallic materials. The energy transformation in both the base and the counter body and both the surface and a certain subsurface volume. The heat generation consists mainly of the thermal energy, the irreversible plastic deformation of the materials and the fracture energy associated with the energy required to generate new surfaces and thus to form wear particles.The energy derived from the secondary reactions are of minor significance and can be neglected, especially those connected to the exothermic processes, mechanical oscillations and structural transformation.

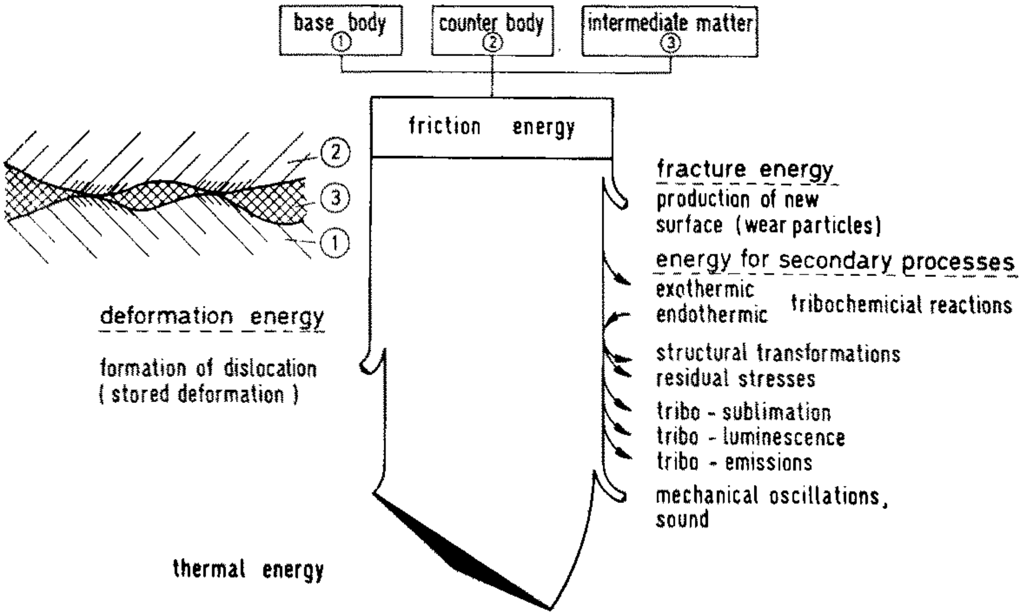

Figure 2.14: Energy flow and distribution among the participating physical and chemical processes(7)

The triboprocess diagram of Fig.2.15 constitutes a possible conceptualization of rubbing condition. According to the diagram, the system can be divided into five conceptual subsystems. Each subsystem interacts with the others transferring information.

The first subsystem is the thermal one in which the transient temperature distribution in the sliding parts is related to the mechanical work at the sliding interfaces. The mechanical subsystem represents the normal and the friction forces acting on the contacting bodies and the temperature distribution within the parts are converted into strain and stress distributions throughout the components. The contact surface area and the contact stress are also determined in this subsystem. The moving and the static parts are demonstrated by the subsystems, material I and material II, respectively. The properties of both materials interact with mechanical and thermal subsystem.Lastly, the wear debris is illustrated by the material plane III.

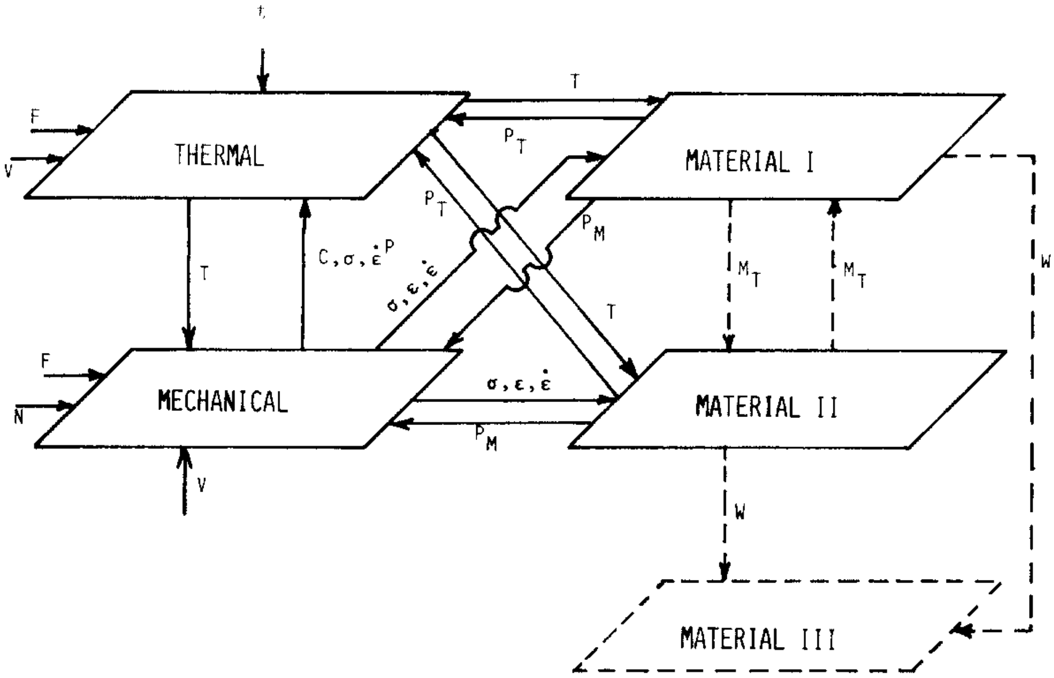

Figure 2.15: Triboprocess diagram for rub energetics problems: T, temperature distribution; C, contact conditions; σ, stress distribution; ϵ, strain distribution; $\dot{\epsilon}$, strain rate distribution; P_M, mechanical properties; P, thermal properties; W, wear; M_T, material transfer; N, normal load; F, friction force; V, sliding velocity; t, time.(8)

Fig. 2.15 represents not only the interaction between the subsystems but also the system's inputs. The inputs of such a system are the normal and friction load, the sliding velocity and the time.The aforementioned techniques shows a general appoach of the frictional process without accounting the thermochemical reactions, oxidation or environmental factors. Notwithstanding, this procedure can be implemented to handle frictional problems and establish a methodology in developing numerical models for sliding systems.

A portion of the friction energy dissipated in a system is related to the development of the wear. Wear is defined as the loss or transfer of material when contacting surfaces slide. Wear is not a property of a material, it is a system dependent property. A system consists on the mechanical properties of the materials in contact, its composition, micro structure, chemical properties, surface roughness and treatments, contact geometry, type of motion and relative speed, pressure or load, vibration, environmental conditions such as temperature, pressure, composition of the surrounding gas, lubrication and lubricant chemistry etc.(32)

Wear mechanism can be classified into six wear modes : 'abrasive', 'adhesive', 'fatigue', 'corrosive', 'melt' and 'diffusive' wear. The first three types of wear are more descriptive of the mechanical wear. In the situation of corrosive wear, a tribochemical reaction between contact surface materials and the surrounding lubricants. Melt wear model occurs when the sliding interaction between the bodies and the derived frictional energy are high enough to increase the temperature above the melting temperature of the material. A first attempt to construct wear mechanism maps of exploring a broader pattern have been proposed by Lim and Ashby(9).

Lim and Ashby (9) attempted to construct wear-mechanism maps which summarize models and data for wear indicating the dominant mechanism, for any given set of conditions to be identified. Two converging routes have been followed:

- Empirical: Data from wear experiments are plotted on suitable axes of load and sliding speed,identifying the mechanism by observation.
- Physical modelling: Model based equations describing the wear rate caused by the each mechanism are combined to indicate the total wear and the field of dominance each.

Based on simplified wear equations and calibrating them using data from a large number of pin-on-disc experiments, Lim and Ashby(9) created the wear map shown in Fig. 2.16, which provides the contours of wear regimes and the dimensionless wear rate as a function of dimensionless normalised pressure and dimensionless normalised velocity, defined as:

$$W_n = \frac{W}{A} \tag{2.12}$$

$$F_n = \frac{F}{A \cdot H_o} \tag{2.13}$$

$$v_n = \frac{v \cdot r_o}{a} \tag{2.14}$$

where W is the volume lost per unit sliding distance, A is the nominal contact area and r_o is its radius, F is the nominal pressure divided by the nominal contact area, v is the relative sliding velocity and a is the material's thermal diffusivity.

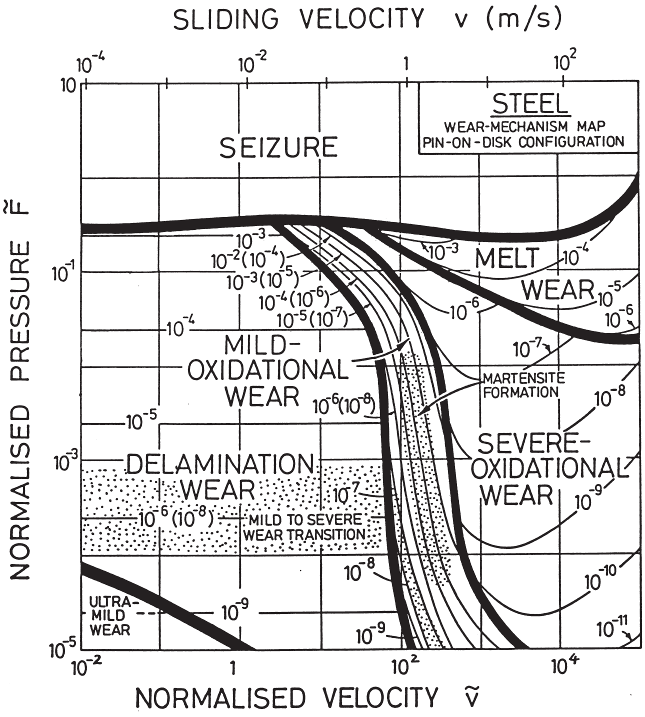

Figure 2.16: A wear-mechanism map for low carbon steel based on physical modelling calibrated to experiments.(9)

Figure 2.16 illustrates a wear map for the case of low carbon steel. The regimes of the wear mechanism have been derived from the physical modelling and calibrated to experimental data available in literature. Based on the empirical and the physical modelling , the regions of dominated wear mechanism are mapped using the sliding conditions as axes, since they are controllable and they determine many aspects of wear behaviour as surface heating(33).

The most confident knowledge about a friction pair tribological behavior can be achieved by carrying out wear experiments which can be used in the development of empirical models with respect to the material and the wear type. The dominating parameters contributing to the sliding wear of a given system are the loading and the relative sliding of the contact. Depending on the sliding conditions,a different wear mechanism might be the dominant which defines the leading one to the fastest rate of wear,at a given loading and relative sliding of the contact. The mechanisms encountered in wear studies of metals include wear by melting, by chemical change induced by frictional heating, by low-temperature plasticity and by brittle fracture.

The attention is particular devoted to the zone of melting wear. As it has been aforementioned, the interaction between the turbine components occurs under high relative speed and high loads. This implies that the dominated mechanism is the melt wear. The temperature analysis of the map has been based on the assumption of a simple 1-dimensional heat flow.

Montgomery(34) investigated the friction and the wear at high sliding speeds, indicating that the predominant mechanism of wear at high sliding speeds is surface melting followed by subsequent removal of a portion of the melted surface layer. Provided experimental data of this work has been focused on the friction and wear of projectile steel on gun steel.It is crucial that at high rate of heat generation, friction coefficient values have been detected to be substantial low demonstrating a completely melted surface layer. As a consequence, the surfaces are probably not actually in contact but are separated by a lubricated film of melted material.In case of steel, wear rate at high sliding speed can be well-fitted by a function of the rate of heat generation according to the following Eq.2.15:

$$\dot{q} = const.\,(\mu \cdot F \cdot v) \tag{2.15}$$

An application of the above wear estimation model on materials having different melting point indicated that the constant c can be expressed as a function of the melting point:

$$const = A \cdot exp\,(B/T_m) \tag{2.16}$$

It is evident that materials with high melting point such as steel or nickel has the potential to show low wear rates.Experimental observations are in consistency with physical modelling of wear maps, since the zone of melt wear is defined by the melting temperature of the individual material.

2.5 Summary

To sum up, finite element analyses are proven to be an appropriate mode to understand the FBO event turbine failure, fragments interaction, in terms of failure and fracture initiation, stress and temperature distribution. The drawback of extensive computational time is still to be overcome. However, the continuous improvement in computational resources gives evidence that this kind of analysis is valid. The recommendation of a methodology should necessitate an efficient modelization to attain reliable as well as cost-efficient solutions.

A significant advantage of the FE is the ability to estimate wear propagation taking into account the analytical geometry of the structure and conducting a thermo-mechanical analysis.Wear prediction is of the essence in the particular scenario of shaft failure where sliding friction between turbine components is inevitable and the accurate prediction of the occurrence of blade tangling is a requirement for the determination of rotational speed.

3

Modelling Approach and Methodology

This chapter gives an overview of the modelling strategy and the methodology derived in order to capture the dynamic phenomena of turbines in contact. The main aim is to show the steps followed to simulate the impact between the free rotor and the following static arrangement.

3.1 Simulation strategy

Turbines in contact is a complex problem to analyze. An insight into the prevailing phenomena of the impact can be achieved through the FE analysis. Non linear finite element analysis solver, LSDYNA, has the potential to capture the impact between the structures and facilitates the estimation of the heat dissipated as friction between the structures, the increase of temperature on the contact interface and the material failure.

The complexity of the impact necessitates to adopt a modelling strategy in order to define properly the problem and to achieve the objectives avoiding possible numerical errors and offsetting the computational time penalty. The scheme of the Fig.3.1 illustrates the strategy followed for the investigation of turbines in contact.

The diagram of the modelling strategy shows the fundamental steps of the analysis. As depicted, the first priority is to identify the areas of investigation.

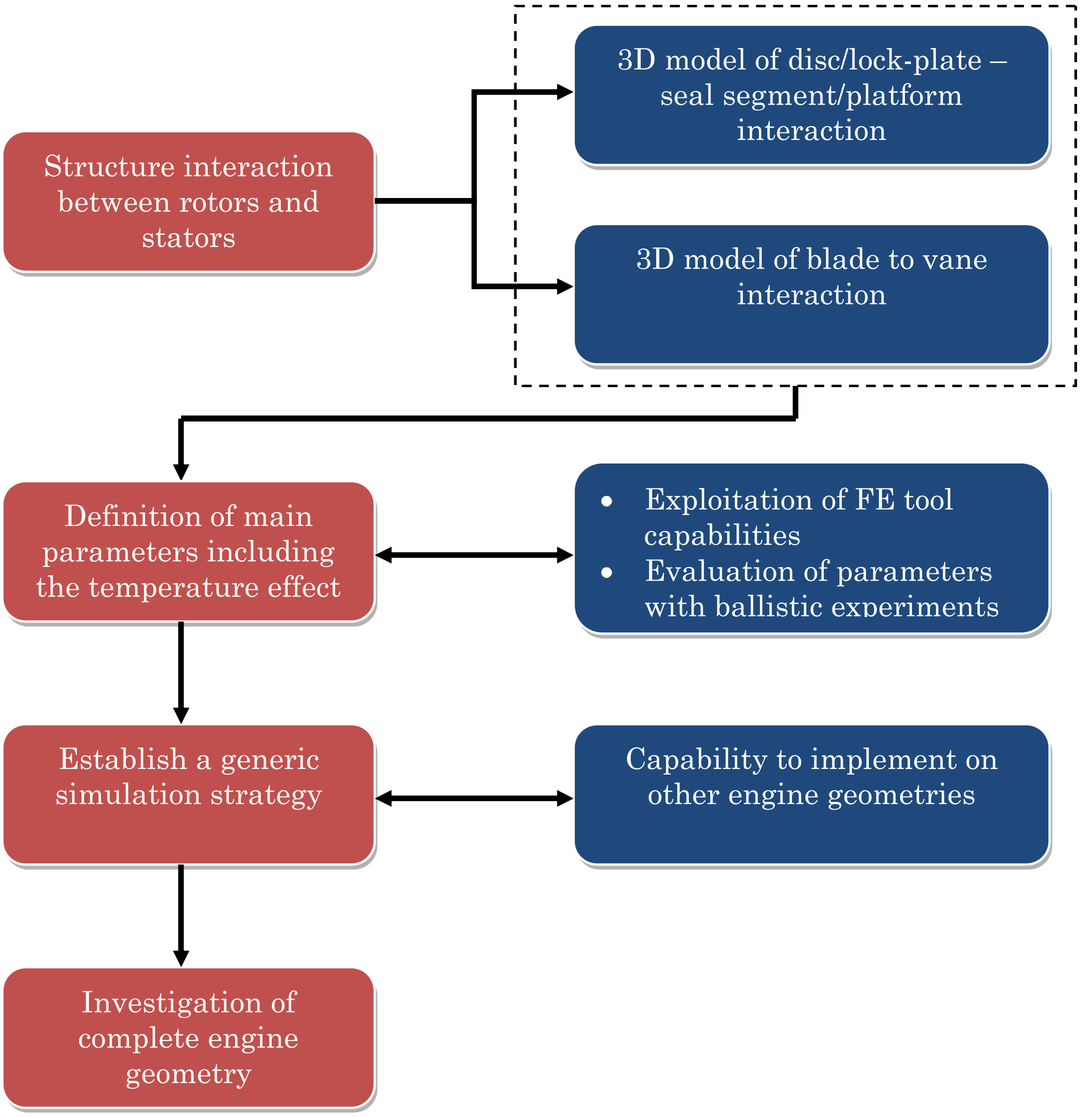

Figure 3.1: Diagram of the modelling strategy

As aforementioned, the first contact interaction takes place between the lower parts of the turbines meaning the region of the lock-plate of the disc and the seal segment and platform of the static structure. In effect, it is the structure of the seal segment which prevents the blade tangling occurrence and, thus, a substantial section of the seal segment structure has to fail in order to have further displacement of the IP turbine. Having this in mind it is possible to divide the structure interaction into two key areas of interest:

- Interaction between the disc/lock-plate and the seal segment/platform of the NGVs.
- Interaction between the turbine blades and the downstream turbine stators.

The models of the above areas of interaction should capture various aspects of the dynamic impact phenomena. Sample of analytical 3D geometric structures are illustrated in Fig.3.2 and Fig.3.3. These 3D structures reflect, respectively, the real geometry of the lower and the upper parts of the rotors and stators of a modern three spool HBR turbofan engine. In more details, all the models developed in the context of this project are presented later on in the same Chapter.

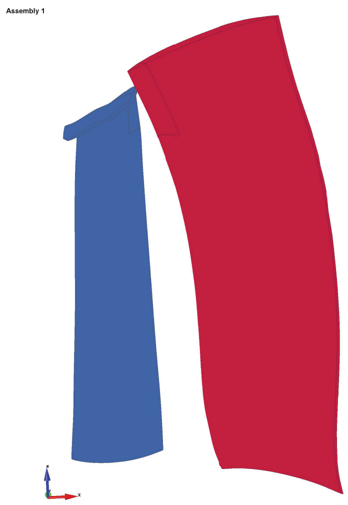

Figure 3.2: Geometric structure of blades and vanes

After the development of the geometric models, the investigation needs to encompass the determination of the boundary conditions and the specification

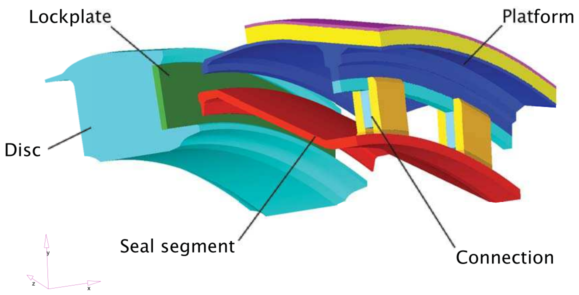

Figure 3.3: Geometric structure of disc/lock-plate and seal segment/platform

of the modelling features. The modelling features referring to the fidelity of the meshing, the definition of the contact algorithm and the choice of the constitutive model are determined through parametric studies. In the light of insufficient publications on the topic of turbine interaction, the process of parametric studies required considerable effort, therefore they have been successfully carried out in the context of MSc theses.

Generally speaking, parametric analyses assisted in adopting modelling techniques, overcoming modelling challenges, preventing numerical errors while they provided a better insight into the understanding of the crash phenomena. However, apart from the parametric studies, further actions have been taken in order to assess the simulation results.

When this kind of investigation is performed, the absence of experimental data can be a drawback in the evaluation of the methodology. The answer emerged from the literature review in the field of ballistic and pin-on-disc scenarios. Ballistic scenarios are used as a starting point in the analysis of the failure and the contact algorithm definition while pin-on-disc scenarios are implemented to evaluate the prediction of the wear and the friction energy on the contact interface. The ballistic and the pin-on-disc scenarios are described in detail in Chapter 5, in which the LSDYNA simulation results are compared with experimental data, available on public domain.

Lastly, the methodology of the turbines' interaction is concluded with the generic modelling analysis described in Chapter 4. The initial target of the analysis performed is to establish a generic approach able to be implemented on other engines' geometries and easily integrated with other codes developed in the context of shaft failure modelling.

3.2 Evolution of FEA models and parametric analysis

This section gives a representation of the FEA models developed during the dissertation. As aforementioned, it is the first reported attempt to provide an insight into the interaction of turbines using FEA solvers. Having this mind, FEA models have been initially developed and then evolved as dictated from the parametric analyses studies and from the attained knowledge. The evolution of the models provides information about the modelling approach while it gives feedback about the parameters that are essential for this sort of impact.

In the description of the simulation strategy, the splitting of the structure interaction between rotors and stators into two key areas is reported as well as the assets of the recommended approach. The investigation and the parametric studies are performed independently. Therefore, there are two parts, the first one is devoted to the interaction between the lower part of the turbine and the static arrangement and the second to the effect of blade tangling.

3.2.1 Mechanical analysis of lock-plate/seal segment impact

The initial analytical model developed for the investigation of the structural interaction between turbines after contact is illustrated in Fig.3.4. In Fig.3.3, on the left side, there is the IPT disc while on the right the LP1 NGV seal segment and platform are illustrated. The geometry of the disc is not complete mainly for two reasons. Firstly, the complete geometry would involve more elements increasing the computational time without contributing to the accuracy of the model. Secondly, the disc is not involved in any contact interaction with the surrounding structure whereas the clamped lock-plate interacts directly with the opposite structure of the seal segment and platform of the NGVs. The lock-plate is defined as a different part which is fixed to the rotating disc using shared nodes. In this way it is possible to simulate the contact only between the lock-plate and the NGVs. The lock-plate is simply a ring of constant thickness. The mass and the inertia of the whole structure are taken into account to scale down the applied axial load and torque, respectively.

On the other hand, the NGV is mainly made up of the seal segment, the platform, and the connection between those two. As illustrated in Fig.3.3, to fix the platform another element has to be added to the geometry denoted as fixing in the Fig.3.3. It is simply an external ring-like structure that is connected to the platform and that is fixed, in turn, on its top surface. It could be argued that it was simpler to fix directly the top of the platform by constraining the nodes on the top surface. This choice, however, would result in a stiffer structure. The actual piece of material taken into account is connected to the NGV stator vanes, that are fixed at the engine casing through the shrouds. Therefore the NGV vanes will provide the platform plus seal segment structure with some elasticity that would be largely reduced if the latter was fixed at the top of the platform. This fixing is much shorter than the NGV stator vanes, in order to limit the number of elements.

3.2.1.1 Boundary conditions and modelling features

The modelling features involve:

- Element type and formulation
- Material models: Plastic kinematic model and rigid
- Contact definition

The boundary conditions have been defined based on the engine data in view of demonstrating the impact between turbines in contact. The boundary conditions include the definition of:

- Initial velocity
- Loads: axial load and applied torque
- Damping

Element formulation Different element types can be implemented in different areas of the structures according to the demands of the impact and the geometric features. In this model, hexahedral elements are implemented in the most of the structure, as presented in Fig.3.4. However, in the case of the sharp end of the seal segment, pentahedra are used to avoid mesh distortion(29). In terms of mesh quality, the created elements limit the aspect ratio, the skewness, the Jacobian and the warpage between acceptable values(31). More flexible limits are applied on the areas that have been considered as rigid bodies (rigid material is analytically described in page 47) and are far enough from the contact interface such as the disc. In this way, a further reduction in computational time is achieved with negligible effect on the accuracy of the simulation results. Regarding the choice of the element formulation, the elements in the lock-plate are assigned to the selective reduced fully integrated solid element assuming constant pressure through the element(29) avoiding element distortion due to sever impact, while the constant stress solid element formulation is applied on the rest of the parts including also blades and vanes.

Plastic kinematic material model It is considered to be the most usual material model used in crash simulations. At low stress level, the stress is dependent on the state of strain. When a stress limit, yield stress, is achieved, a non-recoverable plastic deformation occurs.

The elastic-plastic material type, despite being fairly simple is an effective one, as it has a bilinear stress strain curve. To specify this material, the Youngs modulus and the hardening modulus are required. The first one (E) is the slope of the elastic part of the curve and the second one (Et) is the slope of the plastic part. The stress strain curve used by this material card is depicted in Fig.3.5. Additional parameters assisting in the definition of the material model are the

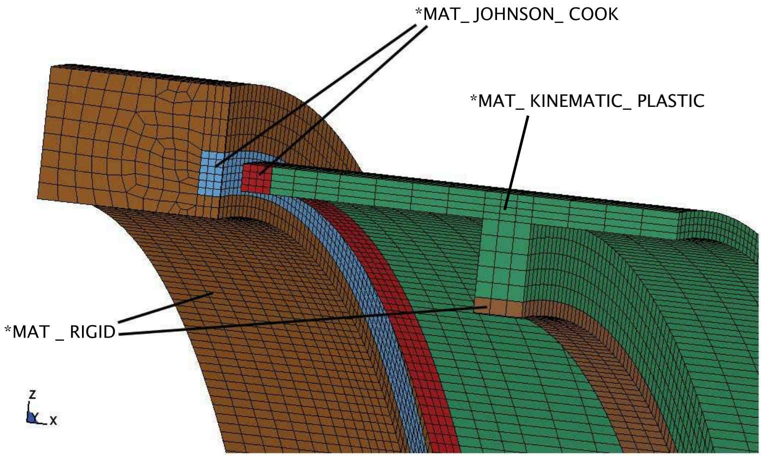

Figure 3.4: Structural mesh of disc/lock-plate and seal segment/platform

formulation for the rate effects and the choice between kinematic and isotropic hardening.

The viscoplastic formulation allows for a great improvement in the results both in terms of noise reduction and stress accurately determined as a function of strain rate. Regarding, kinematic or isotropic hardening choice, Witek et.al. (14) stated that isotropic hardening can be more suitable for turbine rotor materials. The difference between the kinematic and isotropic hardening are depicted in Fig.3.5.

Additionally, it is possible to account for strain rate effects using the Cowper and Symonds model. It is a well known model that multiplies the stress strain curve for a scale factor that depends on the strain rate (28). Therefore, it allows to take into account the effect of the strain rate by scaling the yield strength with the following factor:

$$1 + \left(\frac{\dot{\epsilon}}{C}\right)^{1/p} \tag{3.1}$$

The value of the two parameters C,p can be determined by low and high velocity impact experiments with Inconel 718 available in public domain. Figure 3.6 presents the effect of the Cowper Symonds on the stress distribution of the seal segment structure to emphasize how important is proven in be in the simulation of severe impacts. The absence of strain rate effect scan lead to misleading results in

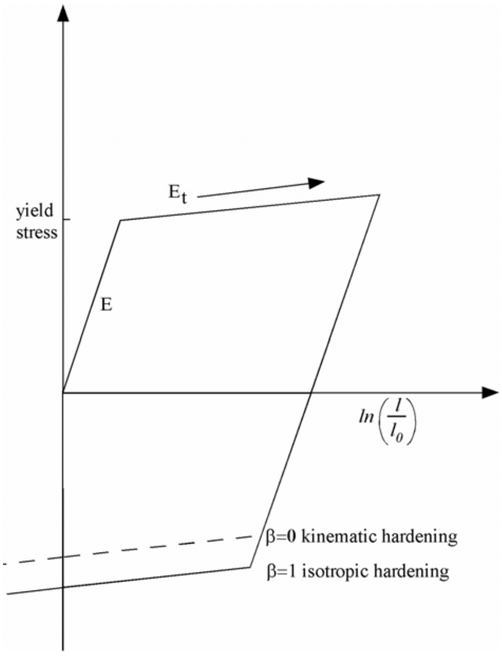

Figure 3.5: Stress-strain curve

terms of stress and strain distribution. This is important when a failure criterion based on the stress and the strain rate, for instance, is applied on the structures.

Rigid material model Some parts of the models are not involved in contact but also they are far enough from the contact interface making it feasible to be accounted for non deformable parts without any consequence in the results. To use rigid structures in these regions is an efficient method to reduce the computational time without any compromise in the results' precision. The rigid material is defined only by the density, the Youngs modulus and the Poissons ratio.

Contact card This is one of the most important aspects, since everything that happens at the interface between the lock-plate and the NGVs depends on the definition of contact, and in particular on the parameters used. An automatic contact is defined, which is repeatedly suggested, particularly in crash simulations where it is not straightforward to know how and where contact will take place.

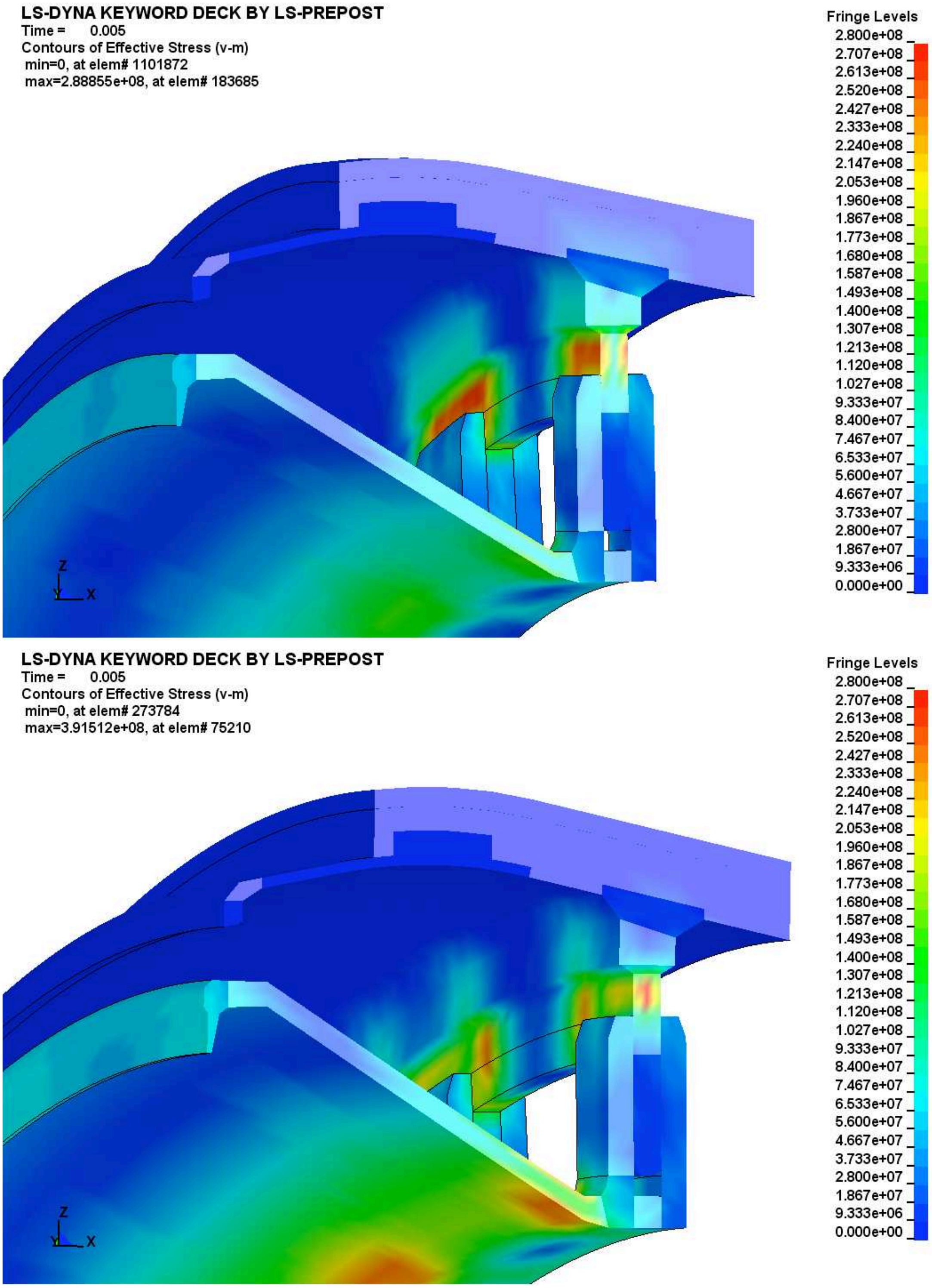

Figure 3.6: Cowper and Symonds model effect. Cowper and Symonds model used (top), no account for strain rate (bottom)

In cases of high deformation of the structures, it may become impossible to determine the orientation of the contacting surfaces. Automatic contact types automatically check for the orientation in order to avoid undetected contact.

In addition to the automatic scheme, the surface to surface choice is defined denoting that a two-way treatment of contact. This means that all the procedure used internally in LSDYNA to determine if a slave node is penetrating in a master surface is called twice, in order to check if a master node is penetrating in a slave segment.(31)(28) In Appendix A, the definition of the parameters of the contact card is included while, in §2.3.1, the contact modelling is described in detail in order to have a better picture of the definition of the parameters.

Initial velocity All the simulations start at the moment of shaft failure, therefore an initial rotational speed is applied to the disc and the lock-plate. In addition to this, it is necessary to define a preload condition on the structure at the beginning of the simulation though the implementation of dynamic relaxation in order to allow for the stress initialization on the deformable lock-plate.

Loads There is a torque and an axial load applied to the disc. The torque is used to simulate the effect of the gas flow through the blade row of the IPT. The axial load, instead, is used to simulate the load of the main gas path and ideally the effect of secondary air system acting on the IPT rotor and resulting in the axial displacement. These two loads have been taken from engine data, and in particular from the results of the in-house industrial code called BD29 (§2.1.4.3) and are depicted in Fig.3.7 with respect to time. In order to take into account the fact that only a part of the disc without the blades is modelled, both loads are scaled down according to the mass and inertia of the whole turbine rotor.

The disc is always modelled as a rigid body due to the fact that the torque and the axial load need to be applied. In this manner, there is not any demand for applying dynamic relaxation on the rigid disc, while intense deformation due to excessive centrifugal loads is prevented. In the contrary, dynamic relaxation needs to be imposed on the lock-plate to initialize stress due to the rotational speed.

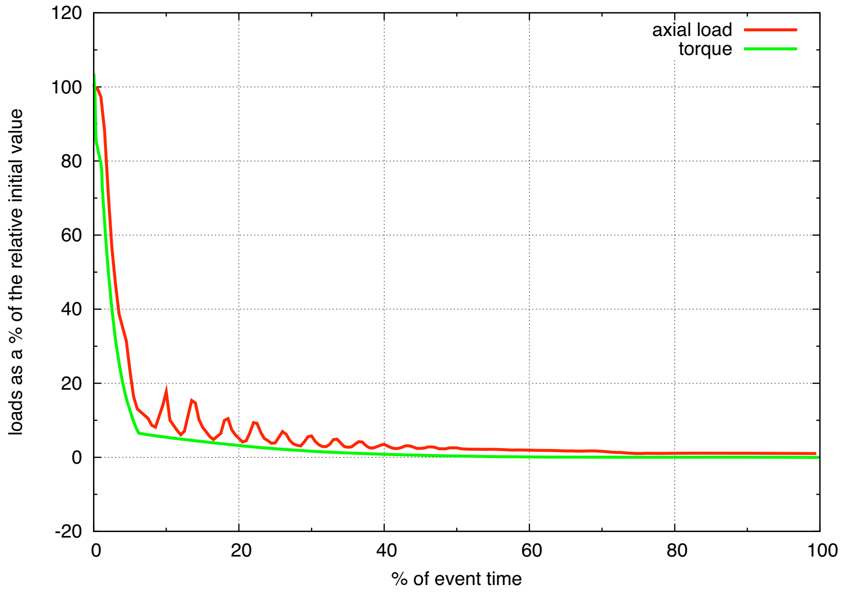

Figure 3.7: Axial load and torque applied to the disc

Damping In real structure, the NGVs are clamped at the tip of the vanes. The lack of the vanes in the structure and the location of the fixing close to the platform of the NGVs provoke a stiff response of the structure after the impact. This causes axial vibration on the IPT rotor. To overcome the issue of stiff response and damp the oscillations, a damping coefficient can be applied on the structure in order to avoid bouncing of the IPT rotor.

As aforementioned, the platform is fixed thorough the ring-like structure (denoted as fixing). If the platform and seal segment structure is considered as a cantilever beam, the bending stiffness of the cantilever is calculated according to Eq.3.2.

$$bending\ stiffness \propto \frac{EJ}{L^3} \tag{3.2}$$

It is evident in Fig.3.8, that the length of the fixing (Lfixing) is less than the length of the stator vanes(Lstator vanes). For this reason, the same applied load provokes more oscillations and vibrations of the structure in the FE model. Although the NGV stator vanes cannot be simplified with a cantilever beam, the concept is still valid.

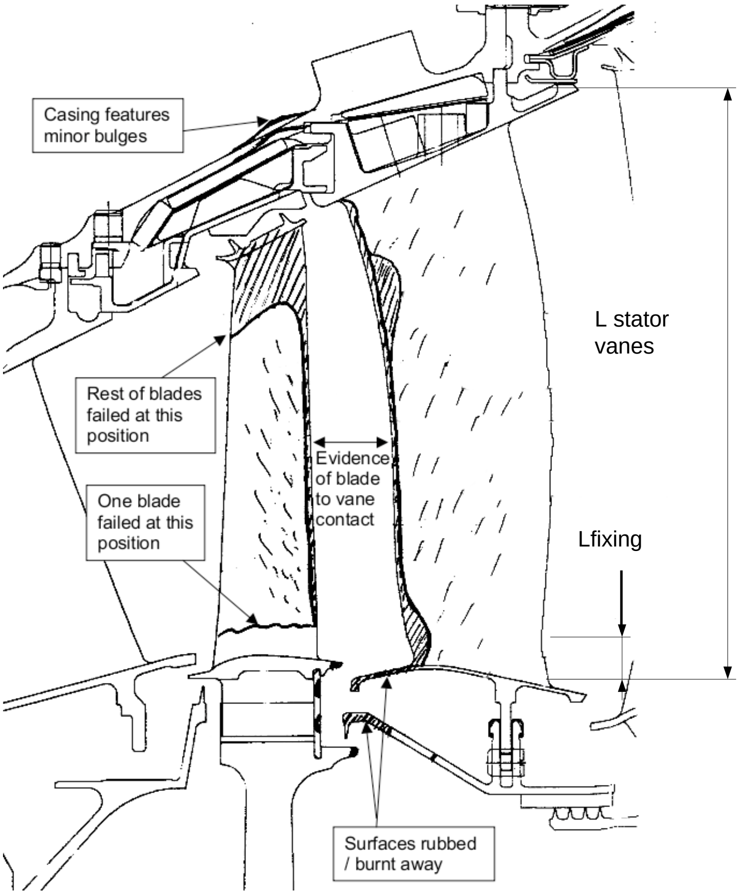

Figure 3.8: Length of the fixing used in the model and length existing in the real engine

In case of the totally undamped system as depicted in Fig.3.9, a node of the seal segment and platform oscillates a lot in the x direction. An imposed damping coefficient can demonstrate the real behaviour of the structure which does not cause any high frequency oscillations based on analytical simulations of the interaction between a section of the NGVs and a lock-plate. These simulations involve one section of the real structure of the NGVs with clamped vane at the tip and have shown that the structure avoid structural bouncing after the impact.

To properly apply a damping coefficient to a system, its natural frequencies

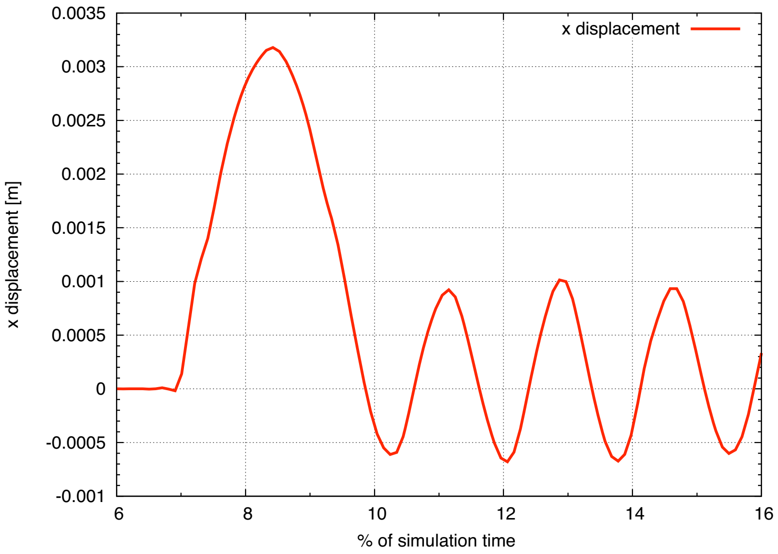

Figure 3.9: Displacement along the x axis of a seal segment node

should be calculated and in most cases it is suggested to apply a damping coefficient proportional to the first order frequency. The mode of oscillation targeted for being damped is the oscillation along the x axis. Based on the axial displacement of the node in case of the undamped case shown in Fig.3.8, the period of oscillation is approximated to be equal to T=0.0009 seconds. The critical damping of an oscillatory motion that has a period T is:

$$critical\ damping \propto \frac{4\pi}{T} \tag{3.3}$$

The damping calculated with this formula is applied to all parts of the NGV structure. It should be said that this is only approximately the critical damping, since the period T is calculated quite roughly, and only the oscillation along the x axis is being damped. Therefore it can be considered as an approximate critical damping only For the x motion and not for the whole system. However, it can be applied to prevent axial oscillations and give a better representation of the impact however parametric studies have been performed in order to show the effect of damping on the structure.

3.2.1.2 Parametric studies

The parametric analyses have assisted in acquiring a deeper insight in the modelling of the IPT and NGV contact. Many aspects of nonlinear finite element simulations have been utilized. The parametric studies have been held in the following areas of interest:

- Contact and Friction Modelling
- Hourglass control
- Damping
- Mesh size

In the next paragraphs, the most important outcomes of the parametric studies are highlighted.

Contact and friction modelling The contact parameters have been investigated in detail. The friction coefficient is calculated using an analytical model which takes into account the static friction coefficient, the dynamic as well as the transition from static to sliding condition(Chapter 2).

The investigation of every parameter of the definition of the friction coefficient of Eq.2.4 have shown that the greatest effect is devoted to the dynamic friction coefficient due to the fact that the impact between turbines takes place under high rotational speed of the rotor and therefore the parameter of higher effect is the dynamic friction coefficient. The effect of the dynamic friction coefficient is well presented in Fig.3.10. As shown in Fig.3.10, there is a linear dependency of the friction energy on the friction coefficient. The increased friction energy affects the rotational speed of the rotor. The effect of different friction coefficients on the rotational speed is shown is Fig.3.11 in which it can be seen that rotational speed decreases. The decrease is affected by the value of the friction energy however it can be pointed out that friction coefficient plays a significant role in the evolution of the event and the determination of the terminal speed o the free rotor. In the lack of available experiment data in the field of nickel alloys rubbing, it is sufficient to specify friction coefficient in a simplified manner by on constant value neglecting the effect of the transition from static to dynamic friction.

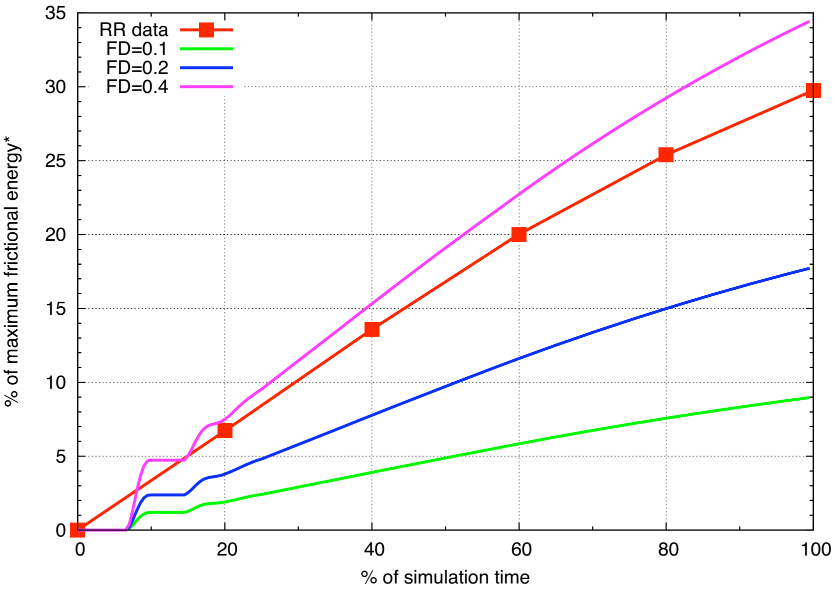

Figure 3.10: % of maximum friction energy attained in engine A scenario with time for difference dynamic friction coefficients (FD)

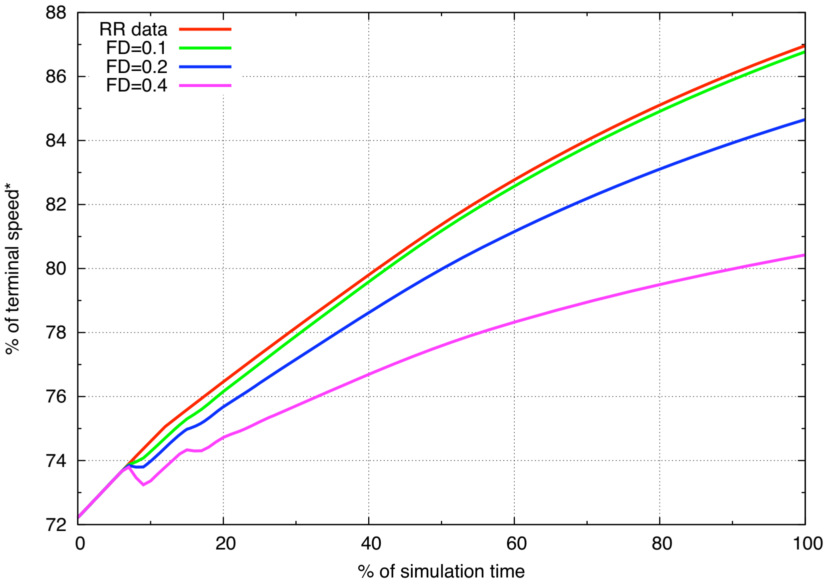

Figure 3.11: % of maximum rotational speed attained in engine A scenario with time for difference dynamic friction coefficients (FD)

Hourglass control Hourglassing addresses the problem of zero-energy mode of deformation(hourglass definition is analytically presented in §2.3.2). Zero-energy modes of deformations means that an element can be deformed without any dissipating energy. One of the most common outcomes of this phenomenon is that the structure has no or little stiffness.

LSDYNA solver gives the capability to the user to select the most appropriate hourglass energy for the investigated impact case. A variety of hourglass algorithms are available. For the investigated scenario, stiffness based algorithms have demonstrated a better performance. However, they add some stiffness to the structure therefore this type of control is better to be imposed on as few as possible parts involved in crash analysis.

The hourglass energy is an important part of the analysis which has been analytically examined by in order to finalize the modelling strategy. Special attention has been focused on hourglass energy mainly because hourglass energy is considered to be a bad feature in a simulation and it is easy to give misleading results.

Damping The structure considered in this model is stiffer than the one existing in the real engine, because the tips of the vanes are not included in the structure. The length of the fixing used in the analysis is smaller than the length of the stator vanes. For this reason, the same applied load provokes more oscillations and vibrations of the structure in the FE model. This is the main reason why a damping coefficient has been applied on the static arrangement.

In this way, the material damping of the LP1 NGV is taken into account preventing any stiff response of the structure due to the fixing around the platform. This stiff response of the structure is mainly connected to the simplification of the structure assuming the fixing around the platform instead of fixed vanes at the shroud as it happens in the real geometry.

Figure 3.12 illustrates the effect of damping coefficient on the gap between the IPT rotor and the LP1 NGV. The gap closure can cause an increase of the pressure inside the cavity. Conversely, if the gap opens, the pressure of the cavity can equalize the one existing in the annulus. Considering the above, damping

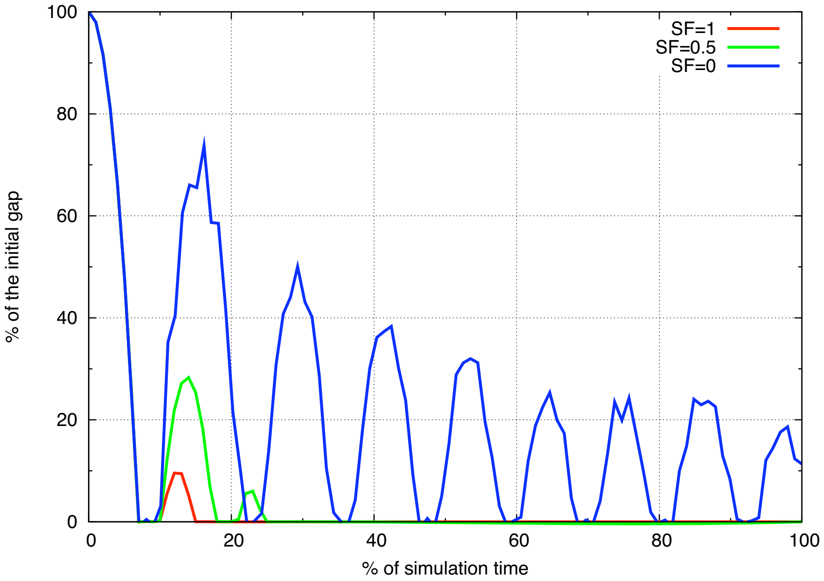

Figure 3.12: % of the initial gap with time for different damping coefficient

can have an effect on the axial load acting on the rotor, thus on the frictional torque and on the terminal speed.

Mesh size A mesh analysis have been carried out in view of understanding the effect of element size on hourglass energy and stress distribution and their effect on the rotational speed and friction energy. The different meshes used in the analysis and the number of elements are shown in Table 3.1.

The simulations gave the same results in terms of friction energy and rotational speed however different handle of hourglass algorithm is recommended when the coarse mesh is used. It is worth pointing out that the coarse mesh used in the mechanical analysis and the parametric studies works satisfactory and it is approved for the current analysis, however a refined mesh can provide better results avoiding the existence of hourglass energy while predicting more accurate the stress distribution with the drawback of high computational demand.(35)

The investigation of the mesh size is more crucial in cases of material failure. On account of a constitutive model with failure criterion, the element size affects

Mesh	global number of elements	elements of NGV
Coarse mesh	608362	223210
Refined mesh	2048024	986612
Fine mesh	2487848	1217744

Table 3.1: Number of elements used in each mesh

the time of failure. Therefore, in these cases, finer mesh is required as it is shown later on in the event of the thermo-mechanical analysis. Furthermore, it is recommended to have always the same element size on the contacting surfaces. Hence, the mesh size on the lock-plate and on the parts of seal segment and platform involved in the contact should be similar. Parametric studies have approved an element size of approximately $5e-6Kg$ for the mechanical analysis to offset the model accuracy with the computational penalty.

3.2.2 Thermo-mechanical analysis of lock-plate/seal segment impact

A combination of thermal and mechanical analysis is considered to be significant for the investigation of turbines in contact. Contact parameters are dependent on the temperature and, thus, the temperature distribution within the contact area needs to be calculated. The modelling of the thermal effect requires a consistent analysis of the temperature distribution throughout both contacting bodies concentrating attention on the contact surface and the near-surface regions.

Regarding the thermal analysis, the determination of the temperature distributions dictates the solution of Fourier's law for heat conduction which for isotropic material is expressed through the governing heat equation described in Eq.3.4 (36):

$$\rho c \frac{\partial T}{\partial t} = k \left(\frac{\partial^2 T}{\partial x^2} + \frac{\partial^2 T}{\partial y^2} + \frac{\partial^2 T}{\partial z^2} \right) + \dot{Q} \tag{3.4}$$

The thermal conductivity κ, the density, ρ and the specific heat, c are representative of the isotropic material type. The heat generation rate, $\dot{Q}$, consists of the heating rate by the friction between the components, $\dot{q_f}$, and the heating rate from irreversible plastic deformation, $\dot{q_p}$.

$$\dot{Q} = \dot{q_f} + \dot{q_p} \tag{3.5}$$

According to Coulomb's law, the frictional force is directly proportional to normal force, F by the coefficient of friction, μ :

$$F_f = \mu \cdot F \tag{3.6}$$

and thus the frictional heat generation rate is equal to the frictional force multiplied by the the relative speed between the components :

$$\dot{q_f} = \mu \cdot F \cdot v \tag{3.7}$$

The heat generation rate due to irreversible plastically deformed material is determined by Eq.3.8 :

$$\dot{q_p} = \eta \cdot \sigma \cdot \dot{\epsilon^{pl}} \tag{3.8}$$

where η is a constant in a range of 0.85-1.00 and represents the work rate to heat rate conversion factor, while σ and $\dot{\epsilon^{pl}}$ are the stress and the plastic strain respectively.

The energy derived from the plastic deformation of the structures in contact is small compared to the frictional heat generation rate. Solution of the Eq.3.4 of Fourier's law can be accomplished following several techniques. However, the most prominent of the techniques are the heat source methods, Fourier transform methods and numerical methods. The benefits of the finite element solution incorporate the capability to accommodate non uniform friction heat generation, finite geometries of complex shape, variations in materials and to control automatically the partitioning of the frictional heat at the contact interfaces. In addition, finite element analysis has the potential to simulate cases of wear using a constitutive model including failure mode. In that sense, a transient heat conduction analysis accounts for the change of contact due to wear propagation.

Thermal analysis has a significant effect in conditions of increasing temperature distribution, but considering only this type of analysis leads to misleading results. It is typical that a constitutive model conducts failure analysis based on both the temperature distribution and the stress distribution. By this means, a mechanical analysis is also required to transform the normal and friction forces at the contact surface, as well as the temperature distribution into a stress distribution.

In mechanical analysis, the geometry of the contacting bodies and the boundary are defined , while the temperature distribution and the temperature dependent material properties are determined through the thermal analysis. For the analysis of the temperature distribution, the geometry of the bodies involved in contact, their relative speed and the temperature-dependent thermal properties of the materials need to be known. The interaction between the mechanical and the thermal analysis is depicted in Fig.3.13

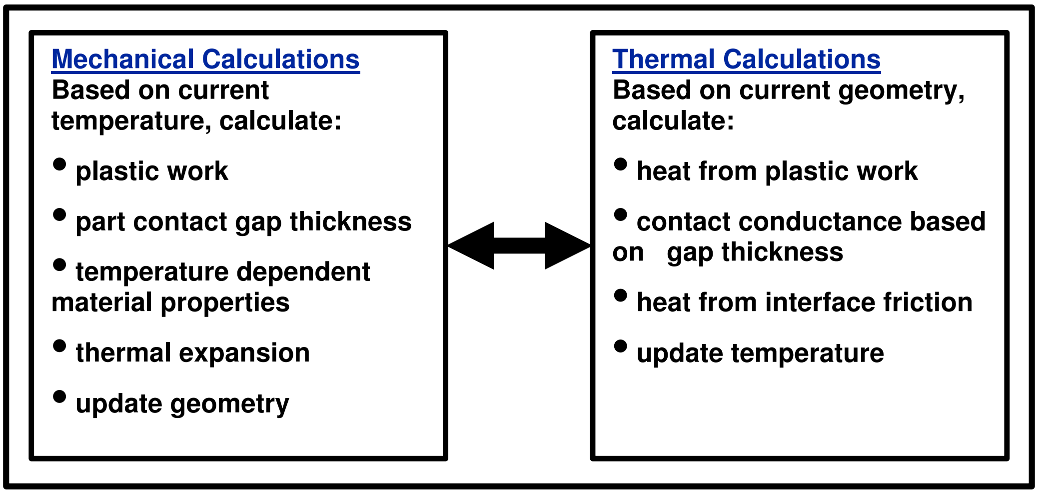

Figure 3.13: Coupled thermal mechanical solver schemes

The main methodology that LSDYNA solver uses is based on explicit time integration, but an implicit solver has to be used with combining heat transfer and structural analysis. As an implicit calculation is run, the optimum solver is the iterative one which requires the definition of convergence tolerances. Moreover, two time steps have to be specified: thermal time step and structural time step, which are completely independent from each other. It is worth mentioning that using the coupled thermal-mechanical solver requires much longer computational times than a structural analysis, a CPU penalty of around 40% is detected.

To conclude, the thermo-mechanical analysis enables the calculation of heat flux at the contact interface considering heat conduction within the zone of intimate contact while mechanical analysis determines the distribution of the shear tractions within the zone of contact and plastic stress, and the strain distributions in the near surface area based on the heat input to the contacted component. The modelling approach of the system of turbines in contact needs to account both thermal and mechanical analysis. This implies that the finite element model is to conduct a coupled thermal-mechanical analysis. This type of analysis has the potential to provide information of the stress distribution as well as the temperature distribution and simulate the failure or wear of the interacted parts based on the failure model of the constitutive model.

3.2.2.1 Boundary conditions and modelling features

The parametric studies of the mechanical model presented in §3.2.1 provided the knowledge of selecting the most appropriate values for the investigation of the severe impact between turbines and revealed the demand of including the thermal effects in the analysis. This led to evolve the models in order to capture the temperature effects and the wear propagation. A aforementioned, FEA solver needs to encompass thermal and mechanical analyses increasing the computational effort to approach prohibitive values. In the view of offsetting the computational penalty, structures of the lower part of the turbines are modified. The modified structures are depicted in Fig.3.14.

The structure presented in Fig3.14 has been used in (37) to simulate the disc to seal segment interaction, provide feedback about the capabilities of the FEA solver to estimate wear propagation and temperature effects and to carry out parametric studies. Although the structure is simplified in many ways, the model yields comparable to reality results. In addition, this structure forms the basis for the generic analysis which is going to be discussed extensively in §4.

In this subsection, the modelling features and the boundary conditions are discussed in the following subsequence:

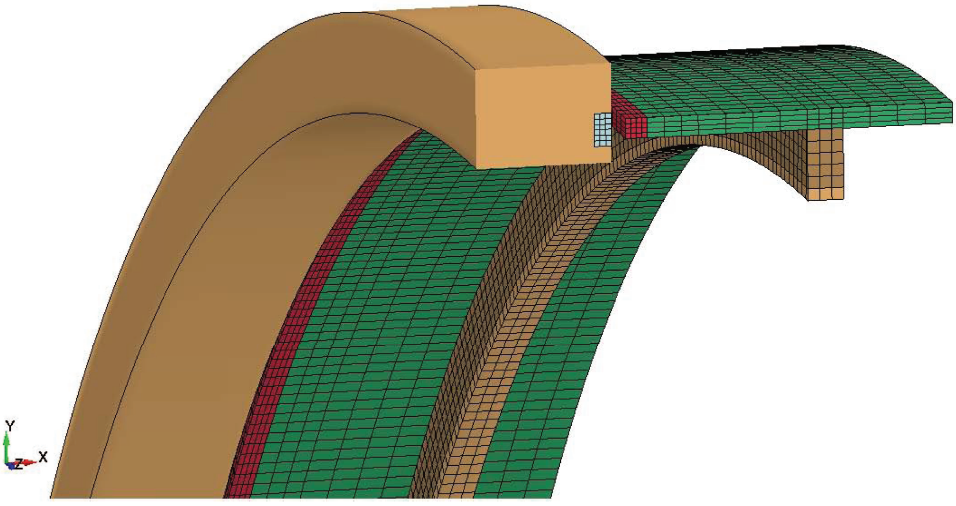

Figure 3.14: Structural mesh of simplified disk/lock-plate and seal segment/platform

- Geometric features
- Element type and formulation
- Constitutive models
- Equation of state
- Contact definition, initial velocity and load

Geometric features As depicted in Fig.3.14, the structure is divided into a number of parts including disc, lock-plate, seal segment and fixing. The part of the rotor disc is modelled as a constant thickness ring and defined as rigid. The mass and the inertia of the free rotor has been accounted for the scaling of the load and the torque. The lock-plate modelled as a constant thickness ring which is connected to the disc through shared nodes. The seal segments is considered as a beam which is fixed to avoid any rotational or translation movement due to interaction.

The division into a number of parts occurred in order to have the flexibility to specify different material models according to the requirements of the simulation. In the paragraph devoted to the material models, the development of every part is explained.

Element formulation All parts are meshed with solid hexahedral elements. The same procedure with the mechanical structure is followed. The quality of mesh is fine however an initial mesh is developed and then based in the mesh sensitivity studies is further enhanced. Special attention is focused on the areas that come directly into contact. Based on the experience with the mechanical model, the same element formulation is chosen and an hourglass control algorithm has been imposed to avoid zero energy modes. In more detail, the hourglass control algorithm and the element formulation are presented in Appendix A in which the LSDYNA input file of thermo-mechanical model is included.

Constitutive models A variety constitutive models have been implemented on the structures. Fig.3.15 depicts the structure accompanied with legends of the constitutive models that are employed for each part. It is possible to see that only the elements that are closer to the contact zone are modelled with the Johnson Cook material card. This allows to save some computational time, since this material model is much more expensive that the kinematic plastic one. The rest of the disc is modelled with a rigid material, as for the original model. A rigid material is used also to fix the ring.

- *Johnson-Cook material model*

  The high impact between the turbine structures is subjected to dynamic loading conditions, implying the existence of a wide range of strains,strain rates, temperatures and pressures, particularly at the region of the sliding interface. A cumulative-damage fracture model is used in order to capture the dynamics of the turbine impact.

  Johnson-Cook material model is commonly used in impact simulations where the metals are subjected to large strains, high strain rates and high temperatures. This model needs to be defined by a number of constants

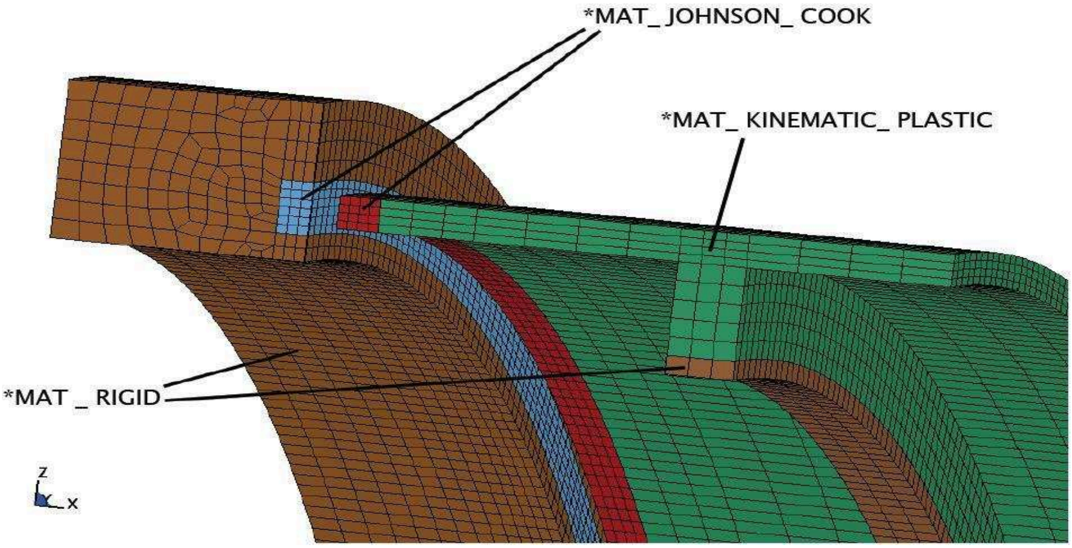

Figure 3.15: Structural mesh of thermo-mechanical analysis

determined from physical tests. In 1985, Johnson and Cook(10) have developed the particular cumulative-damage fracture model and evaluated with an independent series of tests and computations on a variety of metals.

The model for the von Mises tensile stress is expressed according to the following equation:

$$\sigma = [A + B \cdot \epsilon^n] [1 + C \cdot ln\dot{\epsilon}^*] [1 - T^*] \tag{3.9}$$

where

$$T^* = \frac{T - T_{room}}{T_{melt} - T_{room}} \tag{3.10}$$

The first set of bracket represents the stress as a function of strain while the second and the third set of brackets give the effect of strain rate and temperature, respectively. The temperature for the adiabatic condition is due to the plastic work of deformation. In all cases, the adiabatic stresses reach a maximum and then decrease with increasing strain, as depicted in Fig.3.16. The point of maximum stress is important since it represents the point where local instabilities may occur. As it is mentioned, this material model accounts also for fracture as the deformation proceeds. The damage to an element is defined:

$$D = \sum \frac{\Delta\epsilon}{\epsilon^f} \tag{3.11}$$

Fracture is allowed to occur when the the ratio D is equal to 1. This implies that the increment of equivalent plastic strain which occurs during an integration cycle is equal to the equivalent strain to fracture, under the conditions of strain rate , temperature,pressure and equivalent stress.

The fracture at strain is calculated according to Eq.3.12

$$\epsilon^f = [D_1 + D_2 \cdot expD_3\sigma^*]\,[1 + D_4 \cdot ln\dot{\epsilon}^*]\,[1 + D_5 \cdot T^*] \tag{3.12}$$

The dimensionless pressure-stress ratio is defined as the ratio of the average of the three normal stresses to the von Mises equivalent stress:

$$\sigma^* = \frac{\sigma_m}{\sigma} \tag{3.13}$$

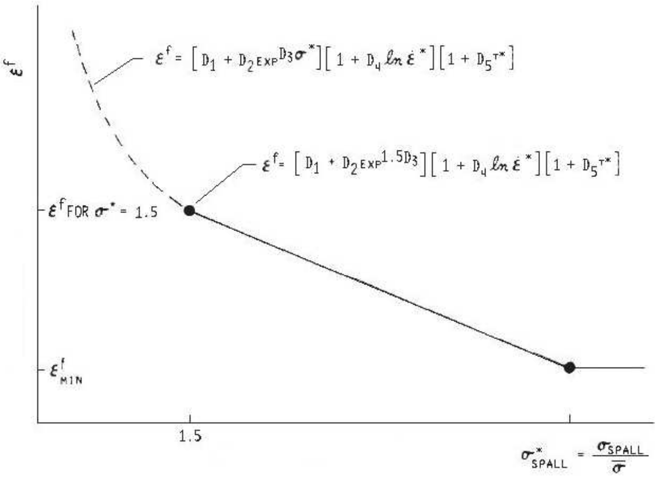

Figure 3.16: Stress-strain at fracture (10)

Mechanical Properties	**Values**
Density $[Kg/m^3]$	8220
Young's Modulus $[Pa]$	1.68e+11
Poisson's Ratio $[-]$	0.28
Yield strength $[Pa]$	9.8e+08
Hardening Modulus $[Pa]$	8.77e+09

Table 3.2: Mechanical properties

Strength Constants	**Values**
A $[Pa]$	1.15e+09
B $[Pa]$	1.305e+09
n $[-]$	0.6
C$[-]$	0.0075
M$[-]$	1.3

Table 3.3: Strength constants(13)(14)

When Johnson-Cook material model is implemented in 3D elements, it is necessary to define an equation of state of the material. The equation of state is the mathematical relation between the different variables that define the state of the material. It describes the state of matter as a functional relation among temperature, pressure, volume, density, internal energy and possibly other state functions related to the matter.

Tables 5.1, 3.3 and 3.4 represent the parameters defining the Johnson-Cook material model for the material of INCONEL 718 and 650^oC.

Fracture Constants	**Values**
D_1	-0.0134
D_2	-0.0255
D_3	0.3
D_4	0.07
D_5	2.5

Table 3.4: Fracture constants(13)

Polynomial EOS Constants	Values
C_0	0
C_1	1.68e+11

Table 3.5: Polynomial equation constants(13)

Temperature[K]	Thermal Conductivity[W/mK]	Heat Capacity[J/kgK]
373	15.4	471
573	19.1	525
773	21	578
973	24.8	631
1173	28.5	684
1373	32	738
1503	33.78	773
2500	38.8	840

Table 3.6: Temperature dependent heat capacity and thermal conductivity

- *Thermal material model*

  This material model is used to specify the thermal properties such as the specific heat capacity, the thermal conductivity, the phase change temperature and the latent heat. It is possible to define temperature dependent heat capacity and thermal conductivity as in Table 3.6. These values are actually used in the modelling of the thermal material of INCONEL 718.

- *Elastic-plastic material model and rigid model*

  Elastic-plastic material model and rigid model. Elastic plastic material model has been implemented in the seal segment that are away from the contact interface, while the rigid material model is employed for the disc and the fixing of the seal segment.

Equation of state The equation of state is the mathematical relation between the different variables that define the state of the material. It describes the state of matter as a functional relation among temperature, pressure, volume, density, internal energy and possibly other state functions related to the matter.

These equations are useful to define the behaviour of fluids and gases, and the volume or crystalline transition of solids. At present, a single equation of state able to predict the behaviour of all substance at all conditions is not known. Each equation is appropriate for a determined range of conditions and substances, so the mathematical model of the EOS has to be chosen carefully depending on the working conditions of the analyzed model.

For the case of high velocity impact, the most suitable choice is the Grunneisen equation of state. No information has been found about the accurate definition of this form of EOS, so a more simplified equation was chosen for all the simulations, as shown in Eq.3.14:

$$p = C_0 + C_1 \cdot \mu \tag{3.14}$$

Equation 3.14 is a simplified form of the polynomial equation of state where C_1 coefficient was specified as the bulk modulus of the Inconel 718 and $\mu = \frac{1}{V} - 1$ and V is the relative volume of element.

Loads, initial velocity and contact In terms of the boundary conditions, they are identical to those implemented on the mechanical model in §3.2.1. Regarding contact definition, the contact card of automatic surface to surface algorithm is chosen (§2.3.1 and §3.2.1) activating the thermal choice which includes the effect of temperature and pressure in the friction coefficient and thermal conductance (28)(37)(35).

3.2.2.2 Parametric studies

Parametric studies are carried out in the thermo-mechanical analysis aiming to introduce to the aspects that affect the evolution of the impact and the wear propagation. The critical parameters involve:

- Damping
- Initial temperature

- Mesh size

Damping The effect of damping coefficient is examined by means of wear evolution. The implementation of damping has as a result to avoid bouncing of the structure. Comparing the results of a damped scenario with a complete undamped, it is worth pointing out that the mass decrease is lower in the first case, as illustrated in Fig.3.17. This has to do with the large amplitude and frequency vibration of the free rotor in the axial direction. The high stresses and as a consequence the high friction energy, as depicted in Fig.3.18 are responsible for the material failure in conjunction with the temperature increase due to the sliding conditions.

Furthermore, in a completely undamped case, the continuous bouncing of the structure results in higher stresses due to the kinetic energy which is deformed into dynamic energy of the seal segment structure increasing the pressure at the interface resulting in higher stresses and strains. Therefore, the failure criterion is achieved earlier and greater mass is eroded from the structure of the seal segment than the cases with imposed damping coefficient within the same time margins.

Based on the analysis performed on the NGV section fixed at the tip of the vane, no rebound of the IPT rotor has been noticed. Therefore, in order to avoid any overestimate of the wear propagation, a damping coefficient needs to be defined which avoids the bouncing of the rotor after the first impact.

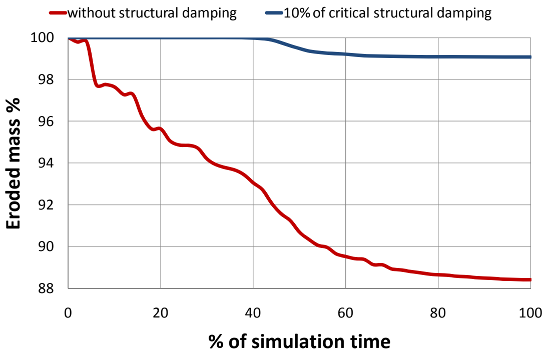

Figure 3.17: Mass change against time with and without damping coefficient

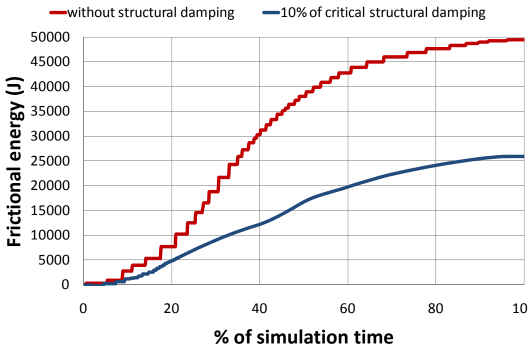

Figure 3.18: Friction energy against time with and without damping coefficient

Initial temperature A model with higher initial temperature has been simulated. The amount of heat transferred during the impact remains similar however the contact interface temperature increases quicker. As a result of the higher temperatures near the contact region, there is much more element erosion. Regarding the results of rotational speed and friction energy , there is not any obvious difference.(37)

Mesh size Basic requirement of the thermo-mechanical analysis is the use of fine mesh. The mesh size can be improved until a compromise between accuracy in the results and affordable computational time and cost is reached. Thermo-mechanical analysis account for thermal effects through the temperature calculation which is calculated as the average temperature of the nodes formulating an element. The heat supply per unit volume is subject to thermal conductivity of the material. In the case of the rubbing between nickel alloys, the thermal conductivity has high value preventing heat diffusion within the structures. Therefore, the size of an element and mainly its thickness affect the temperature distribution on the contact interface. More specific, a coarse mesh with thick elements results in underestimation of the temperature due to high temperature gradient. As a result, the element deletion based on failure criterion is delayed and greater amount of friction energy needs to be dissipated as heat to achieve mass loss.

Figure 3.19 represents how the mean temperature at the contact interface changes with element thickness. Finer mesh at the interface contact provides more accurate prediction of the temperature. This is common also for all the metal structures where the depth of the heat diffusion is insufficient to cause a noticeable temperature increase in long distance from contact interface commanding a short thickness of elements in x-axis. Figure 3.20 presents the refined mesh that has been recommended after the parametric studies.

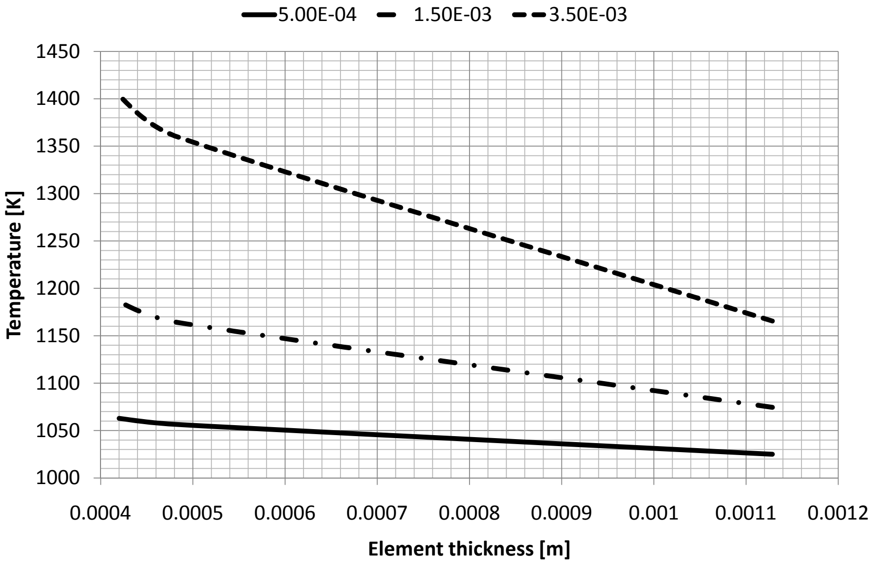

Figure 3.19: Change of mean temperature at the contact interface with element thickness (x-axis) at different times

3.3 Interaction between the turbine blades and the downstream turbine stators

The knowledge gained from the mechanical analysis model of the lock-plate and the seal segment/platform has been used as a basis for the analysis of blade tangling. The FEA model of blade and vane is shown in Fig.3.21. The section provides the modelling approach and the effect of axial displacement on the sliding energy and the rotational speed.

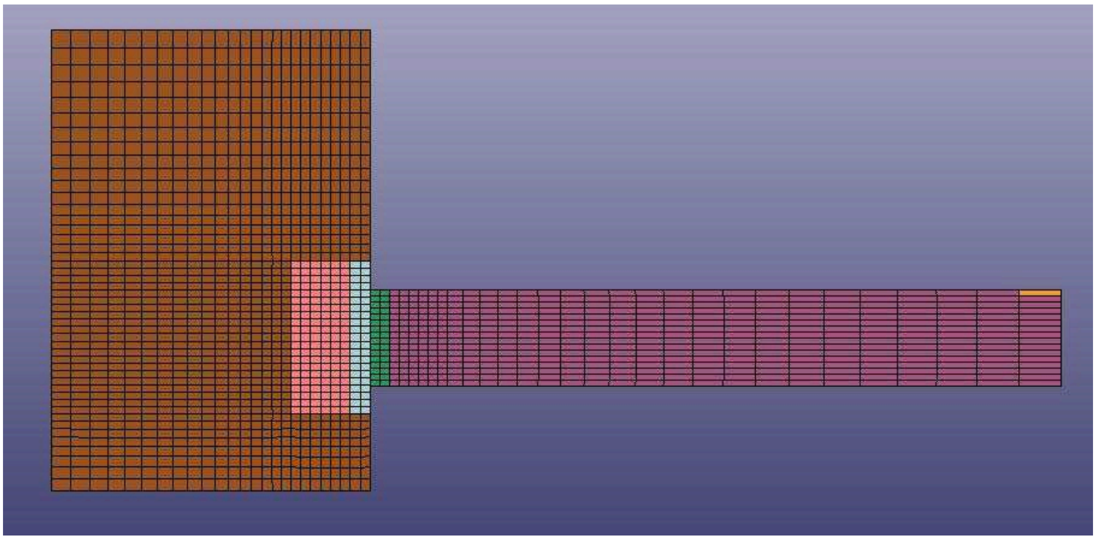

Figure 3.20: Refined 2D mesh representation

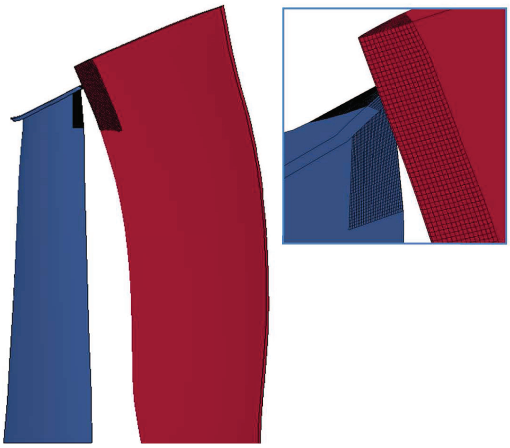

Figure 3.21: Structural mesh of blades and vanes

3.3.1 Boundary conditions and modelling features

Material model and contact algorithm The accurate assessment of the plastic deformation of the materials involved during contact requires including a failure criterion for the material. The piecewise linear plasticity damage model is based on utilizing plastic strain as a damage mechanism of failure of the material. The implementation of the damage model demands a contact card able to remove failed elements. This demand leads to the choice of the eroding option in contact definition instead of the automatic one.

Boundary conditions Before the blade to vane contact takes place, the blades, as a part of the whole turbine, rotate at a high angular speed. Due to the centrifugal effects, the blades are deflected into a quasi-static shape. This preloaded state of the structure is calculated by LSDYNA during an implicit static analysis which is the first part of the entire simulation. The blades are free to rotate about their axial direction, while the center of rotation of the body is fixed and the rotational load is applied as a body force.

In order to study the material interaction between the blades and the vane, a number of assumptions are made considering the boundary conditions applied on the structure. In the described model, the applied load on the free turbine rotor due to pressure difference is defined as a dynamic axial displacement of the center of rotation. In shaft failure events, the dynamic displacement depends also on the dynamic impact phenomenon of the plastic deformation of the seal segment and NGV platform after the interaction with the lock-plate of the disc. In order to evaluate how the growth of the seal segment/platform plastic deformation influences the blade to vane interaction, an analysis of different dynamic displacement scenarios was carried out. This is discussed in detail in the next section.

The actual relative rotational speed between blade and vane is a key parameter in determining the total amount of frictional energy dissipated during blade tangling. A high relative rotational speed implies that significant plastic deformation is likely to occur in both structures following the impact.

The structural model response is also subjected to the torque which forces the rotor blades on a circular path around the mass center. Using as boundary conditions the initial angular speed and the torque versus time, the variation of the rotational speed is then calculated considering the moment of inertia of the structure and the energy dissipated due to impact.

3.3.2 Axial displacement variation

In this study, instead of defining a load that is applied to the IPT structure, an axial translation is employed to demonstrate how the IPT blades will be displaced axially with time. The axial displacement is representative of the forces acting on the structure and affects the growth rate of material plastic deformation. The effects of the axial dislocation of the turbine rotor are illustrated in Fig.3.22 for three different cases of displacement versus time.

Figure 3.22 illustrates the three notional curves of structure displacement versus time that have been examined in this study. The curves represent a possible moderate axial displacement of the rotor blades. The erosion rate of the elements of the seal segment and the platform define when the first contact interaction between the blade and vane tips is going to occur. The axial translation is connected to the wear propagation of the seal segment and platform.

All simulations were initiated at a typical free running turbine angular speed of 1022 rad/sec before blade to vane contact. The applied torque forces the rotor blades to rotate around the mass center with increasing angular speed leading to one rotor revolution in approximately 6 msec. During the high speed impact against the turbine stator, the blade loses its initial velocity and becomes highly deformed as it can be observed in Fig.3.23 and 3.24.

The rotational speed starts decreasing as soon as the high velocity impact occurs due to the frictional forces arising on both structures. In a case of a moderate crash impact, where the rotational speed remains almost unaffected, frictional forces have minimum effect due to smaller contact surface area. A more intense impact, leading to a higher axial displacement in the same time, results in a larger decrease in the rotational speed due to a larger frictional energy dissipation.

In Fig.3.22, each step increase illustrates the contact between one blade and the vane at each time. Due to the existence of only two blades in the model, after a step increase in sliding energy, a period of no material interaction follows until the axi-symmetric blade contacts the vane structure again. It is evident how the axial movement of the free turbine affects the results in terms of sliding energy and rotational speed. Considering the results it can be concluded that a more intense axial displacement commanded by the axial load leads to higher energy dissipation as a result of the increase in the contact area of the interacted bodies. Additionally, the sliding energy and the displacement affect the rotational speed. The rotational speed is decreasing with time in all cases apart from the one with moderate displacement. in which the sliding every is not high enough to produce a braking torque that can withstand the continuously increasing of turbine acceleration. In the case of the rapid blade tangling, the quick transition to the maximum displacement decreases the rate of sliding energy after a certain time allowing the increase in rotational speed.

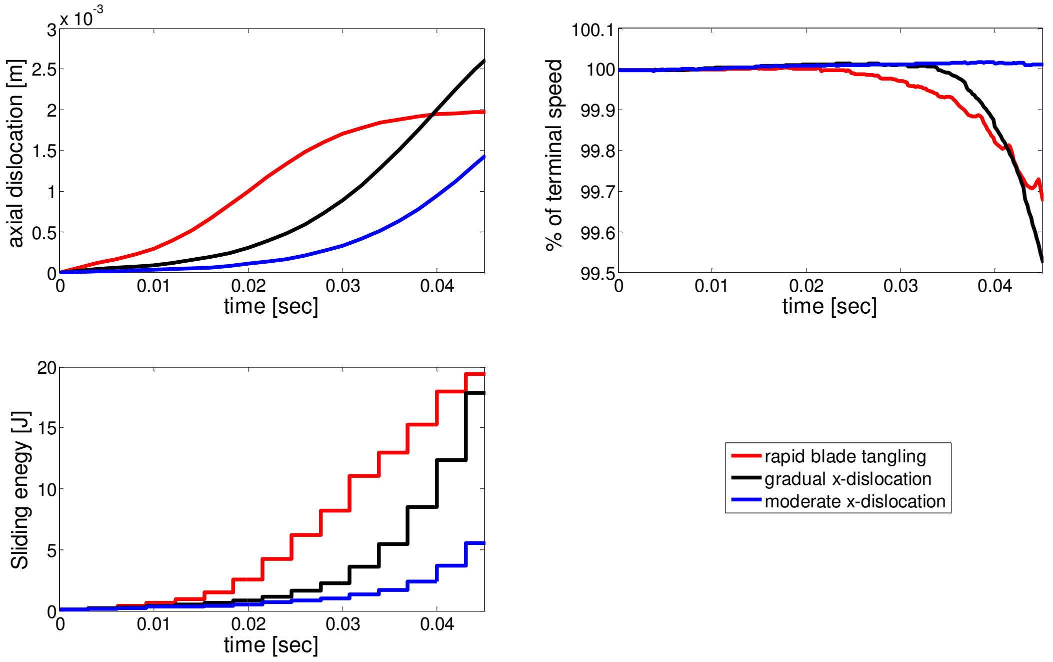

Figure 3.22: Axial displacement, sliding energy and rotational speed with respect to time

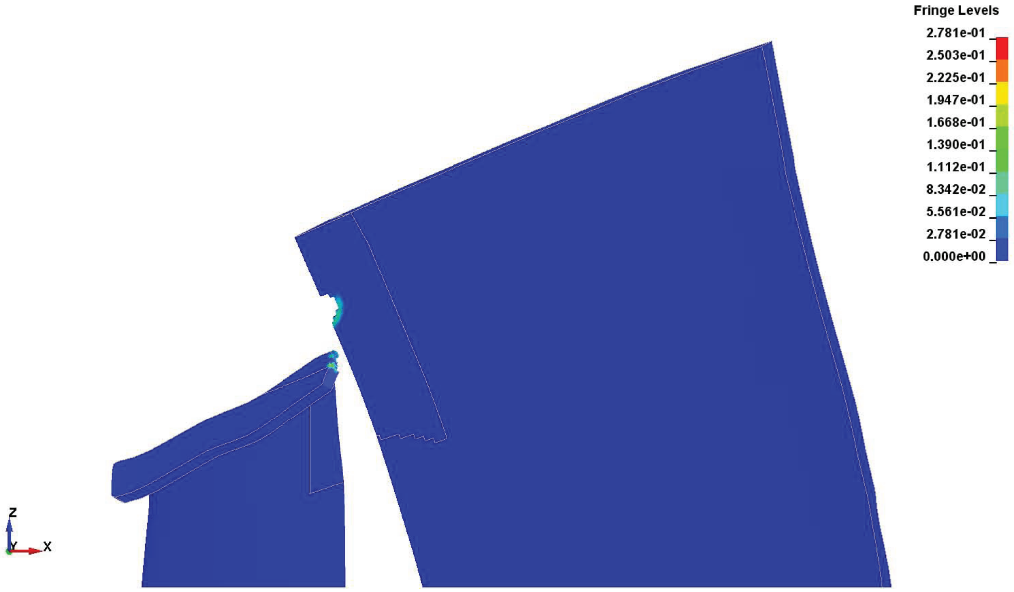

Figure 3.23: Structural mesh of blades and vanes

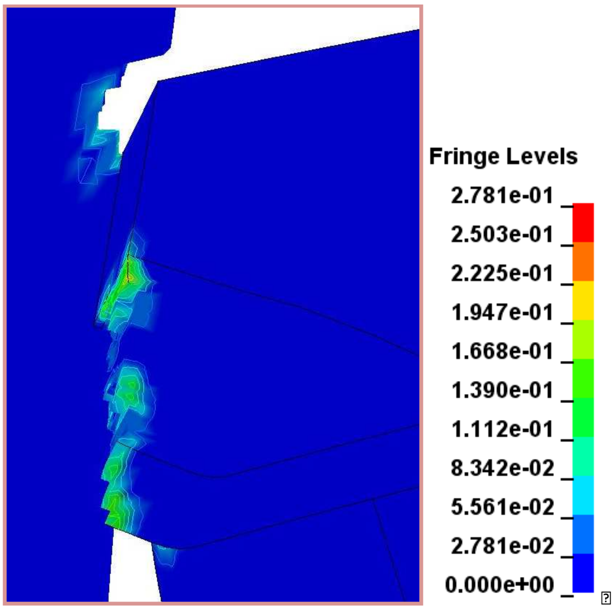

Figure 3.24: Material failure due to high strain

3.4 Summary

This chapter has demonstrated the approach that has been adopted for the modelling of turbines in contact using LSDYNA package. The simulation strategy includes the decoupling of disk to platform interaction and blade to vane interaction. As a result, the initialisation of blade tangling depends on total wear on the disk lock plate and seal segment. The definition of the modelling approach includes the description of all material parameters, boundary conditions, initial conditions and geometries that have been implemented in both mechanical and thermo-mechanical test cases, such as element formulation, material models, initial velocity, load, damping, equation of state, thermal properties, mesh size. In a further step the effect of temperature in the thermo-mechanical approach has been analysed, and its dependency on element thickness has been shown. The chapter concludes with an analysis of the interaction of blades with downstream stators, where the effect of blade tangling on rotor terminal speed has been illustrated.

4

Generic modelling

This chapter is devoted to the description of the idea of generic modelling. The modelling approach highlights the path that needs to be followed to achieve the objectives of the structural interaction after shaft failure. Although, FE solver is proven to be the most promising way of analyzing severe impacts, a few challenges arose considering its implementation. To overcome these challenges, a generic methodology is developed which manages to combine LSDYNA results with structural analysis calculations. The main features of the generic methodology comprise:

- Capability to capture the impact event and the wear propagation
- Applicability in different engine geometries and loading conditions
- Convenience in use
- Quick enough for preliminary design
- Easily integrated with other tools

In the scope of the generic methodology, the critical parameters of load, rotational speed, frictional power and wear rate are expressed in a non-dimensional form. In this manner, dimensionless analysis provide the capability to indicate these parameters independent from time, contact surface area and material characteristics. As a result, it is feasible to define the evolution of a transient event like the interaction between turbines by assuming quasi-steady condition in every step.

This section begins with an introduction into the non dimensional parameters followed by the generation of the non-dimensional maps derived from the simulation results of LSDYNA models and ends with the presentation of numerical tool based on structural dynamics analysis.

4.1 Non-dimensional parameters

A tool for the analysis of turbines in contact in a preliminary stage needs to be applicable to a variety of geometric characteristics. In this direction the wear mechanism needs to be expressed in a non-dimensional form. In further detail,the normalized versions of wear rate, frictional power, load and rotational speed are introduced.

The normalized wear rate is calculated using Eq.4.1

$$W_n = \frac{W}{A} \tag{4.1}$$

where the wear rate W of a sliding surface is defined as the volume lost from the surface per unit distance slid, as shown in Eq.6.1 and A is the contact area.

$$W_= \frac{V}{u \cdot t} \tag{4.2}$$

It is implied through Eq.4.1 that the wear rate is independent from the duration of the event, since the dependency of the wear rate W on the sliding distance is linear.

The main parameters that affect the propagation of wear is the load and the rotational speed. Both parameters influence the heat dissipated at the region of contact and as a consequence the wear. In case of the load applied on the body during the sliding motion, the normalized value of load is defined as :

$$F_n = \frac{F}{A \cdot H_o} \tag{4.3}$$

where A is the contact area and H_o is the material hardness representative for a particular temperature.

The normalized rotational speed is calculated according to Eq.4.4

$$u_n = \frac{u \cdot r_o}{a} \tag{4.4}$$

where r_o is the radius of the nominal contact area and is derived from Eq.4.5.

$$r_o = (A/\pi)^{1/2} \tag{4.5}$$

Furthermore, α is the thermal diffusivity defined as the thermal conductivity divided by the volumetric heat capacity.

Implementing Eq.4.3, 4.4, 4.5 on Eq.3.7, the normalized form of the friction power is defined as

$$\dot{Q}_n = \mu \cdot F_n \cdot v_n = \mu \cdot \frac{F}{A \cdot H_o} \cdot \frac{v \cdot r_o}{a} \tag{4.6}$$

To sum up, the non-dimensional friction power is independent of the contact area and the radius of nominal contact. This means that for a given set of normalized load and normalized speed, there is unique value of non-dimensional friction power which can be applied on contact areas of different shapes and sizes to estimate energy consumed due to slide.

4.2 Non-dimensional maps

In view of generic methodology, LSDYNA simulations were run in order to map the effect of the basic quantitative aspects of wear, load and rotational speed in the evolution of material failure. Figure 4.1 and 4.2 represents the scheme adopted to derive the non-dimensional maps. Alternatively, these results could have been derived from experimental testings which are, however, time and cost consuming.

In light of this, FEA simulations are performed under steady-input conditions. A set of constant values of rotational speed and load are applied on the rotor structure. The geometry of the LSDYNA model is depicted in Fig.4.2. Instead of using the Hi-Fi model of Fig.3.2 and 3.3, which is a realistic representation of the real engine architecture, a simplified structure is recommended for the generation of the non-dimensional maps.

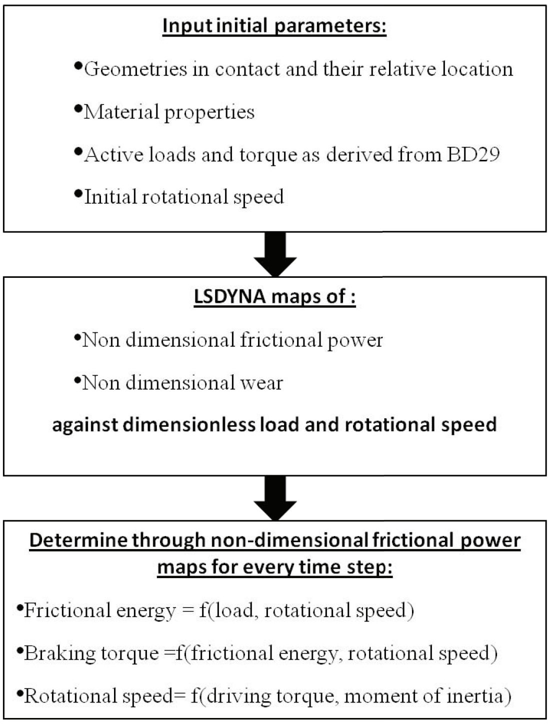

Figure 4.1: Steps of deriving non-dimensional maps

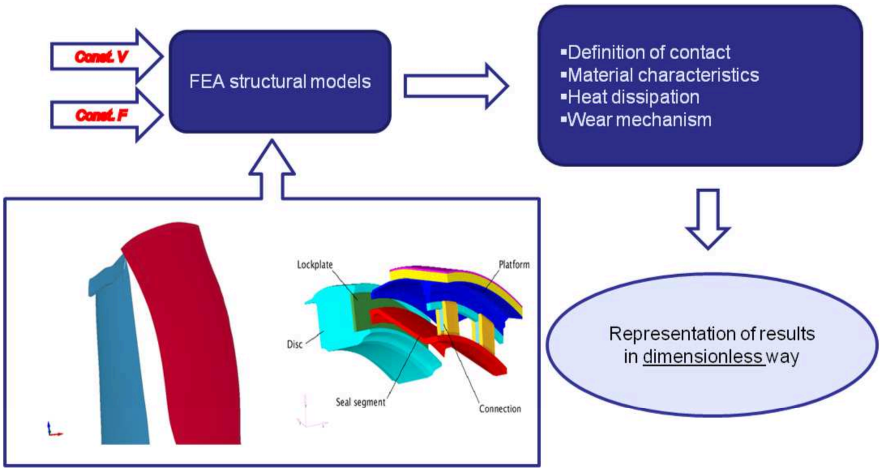

Figure 4.2: Use of FE models to built non-dimensional maps

The choice of the simplified structure appears to be the most ideal since the non-dimensional parameters are independent from the sliding area. Therefore, a structure constant contact area enables the estimation of the normalized wear and frictional power which are applicable, also, on different shapes and sizes of contact area.

In case of the first contact interaction between the lock-plate of the disc and the seal segment, the FEA model consists of the structure of the disc/lock-plate, while the structure of the seal segment is represented by a beam of constant thickness which is fixed on one side to prevent movement on axial direction. The primary dimensions of the simplified structure are based on a real engine geometry. These geometric characteristics include the radius of the disc , the mean radius and the length of the seal segment(the length corresponds to the distance from the contact to the connection to the NGV structure).

In case of rubbing structures, it can be assumed that the predominant mechanism of surface heat is not the plastic deformation but heat generation. Therefore, a way to present the surface heat flux independently from the thickness of the element can be calculated by the following Eq.4.7.

$$q_s = KP\mu u = \frac{KF\mu u}{A} \tag{4.7}$$

where $K = 1/element\ thickness$ in the event of negligible effect of plastic deformation on the contact interface. Equation4.7 can be used to define the surface heat flux when the melting of the material occurs by means of element deletion. The wear of the surface starts when adequate amount of surface heat flux is diffused and follows a linear pattern with respect to time. Consequently, the wear rate can be estimated through the following equation:

$$W_n = \frac{\dot{V_m}}{A\upsilon} \tag{4.8}$$

where A: is the contact surface area, υ: the relative sliding velocity, $\dot{V_m}$: the rate of the volume of the material melted away and is defined as

$$\dot{V_m} = \frac{V_{in} - V_{fin}}{t_m - t_{fin}} \tag{4.9}$$

where V_{in}: initial volume of the structure, V_{fin}: final volume of the structure after the removal of the melted material at time t_{fin}, t_m: time when the melting of the material started, t_{fin}: final time determined by the end of the simulation

More specific, to connect the above mentioned with the interaction between the rotor disc/lock-plate and the seal segment, the quick revolution of the turbine disc, the thermal conductivity of the material in addition to the duration of the contact implies that the heat product remains on the contacted surfaces allowing almost negligible part of the energy to be diffused in the structures. The contact interface of the structure needs to consume a particular amount of heat in order to elevate the interface mean temperature up to the melting limit.

For the blade to vane interaction, the model of the steady input conditions consist of shell elements. Although, an initial attempt to derive non-dimensional maps of blade interaction is succeeded (38), further investigation need to carried out in order to include in the numerical model the blade tangling effect.

The contact definition and the material properties for the FEA model used in generic methodology follows the same pattern with the FEA models analytically presented in the §3.2. The basic modification deals with the boundary conditions, since constant values of axial load and rotational speed are applied on the disc to determine constant friction power and wear rate and derive the non-dimensional maps which connect the normalized power and the normalized wear with the normalized load and relative rotational speed. These 3D curves are analytically presented in Chapter 6.

4.3 Wear Estimation Numerical Structural Analysis of Turbines in Contact

In the scope of the numerical model based on structural dynamics analysis, a FORTRAN code is developed which attempts to combine the LSDYNA normalized results of friction power and wear with structural dynamics equation. The main inputs of this tool include:

1. the geometry of a real turbine engine

2. the load acting on the free turbine structure
3. the torque
4. the initial rotational speed

The input values are converted into a non-dimensional form. In addition, a database of non-dimensional maps of normalized frictional power and wear rate with respect to normalized load and rotational speed is created and imported in the tool.

Figure 4.3 represents an overview of the numerical model. At the beginning, a number of LSDYNA simulation of steady input conditions are carried out to derive the generic maps. Considering the inputs based on an engine shaft failure scenario, the geometry and the gas load determine the axial load, the applied torque and the initial rotational speed. Linear interpolation is carried out in the grid points of the generic maps to define the frictional power and the wear rate.

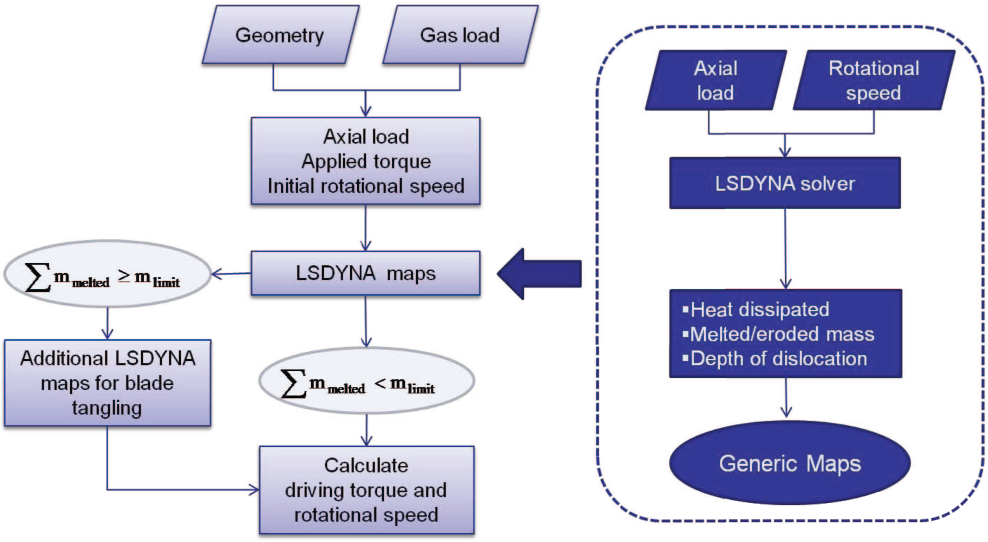

Figure 4.3: Overview of analytical model for the prediction of rotational speed of the free running turbine

In every time step, the frictional energy, the driving torque, the rotational speed and the cumulative melted mass are calculated. Before the occurrence of the blade tangling , only the 3D maps of the lower part of the turbine are accounted in the calculations. When the melting mass approaches a value that allows a further axial displacement with a consequent blade tangling occurrence, additional 3D maps for blade tangling effect are incorporated into the calculation to consider the effect of additional frictional power and wear.

4.3.1 Boundary conditions

The input values of axial load an driving torque are derived from the gas pressure difference. For the purpose of shaft overspeed analysis, a RR code, called BD29 (2), calculates the pressure difference along the free turbine, the rotational speed and the driving torque. The BD29 results in terms of pressure difference and driving torque are implemented as as input on the modelling of turbines in contact to simulate the impact phenomena.

In the FEA analysis, the pressure difference is defined as a mean load acting on the structure of the turbine. The mean axial load is calculated as the product of the pressure difference and the total area of the turbine, including the structure of the disc and the blades.

$$F_{crude} = (P_{entry,IPT} - P_{exit,IPT}) \cdot (A_{disc} + A_{blades}) \tag{4.10}$$

The surface of the disc and the blades are derived for the particular engine configuration (2). In terms of torque estimation, the applied torque is derived from the BD29 code and is equal to the sum of the driving torque and the braking torque. The initial rotational speed of the turbine is defined as the one of the IP turbine at the time of shaft failure.

4.3.2 Geometric features of turbines

In addition to the load and the torque, the geometric characteristics of the engine need to be included in the input parameters. At first, the severe interaction takes place between the seal segment and the lock-plate as the event progresses, a part of the seal melts away allowing interaction also between the lock-plate and the platform. Every engine has different geometry characteristics. In order to understand what controls the friction wear, it is important to include the detailed geometric features of the sliding structures. Discretization of the contact area and the volume of the structures enables to interpret the progress of the wear. For the particular, engine failure the cumulative volume and the area of contact with respect the axial displacement of free turbine from the initial position are depicted in Fig.7.2.

The displacement is specified according to the volume that melts away. At every displacement, the contact areas changes as a part of the structure is ejected from the contact interface. For the purpose of this analysis, the axial displacement of the turbine is taken into account. The structure of the seal segment and platform, as observed, has varied thickness, causing difficulties in the estimation of contact area and displacement. In case of constant area of contact, the resultant wear depth displacement could be calculated from the ratio of melted volume to the contact area:

$$\Delta x = \frac{V_m}{A} \tag{4.11}$$

For the purpose of the analysis the structures of the seal segment and the platform are discretized into small material volumes of the order of $5.317e-10$. In this way, resultant wear depth of the seal segment and platform are calculated continuously to account for the change of the contact surface. Figure 4.4 depicts the geometry based on real engine while Fig.7.2 illustrates the change in contact area and the cumulation wear with respect to the wear depth. Then, the resultant wear depth is given by the summation of volume to surface ratio for every strip:

$$\Delta x_j = \sum \frac{V_{m,j}}{A_j} \tag{4.12}$$

4.4 WENSAT Calculations

The sequence of the equations used in the numerical tool is shown below:

1. Before the shaft failure occurs, the IP turbine is located at a distance from the NGVs, as illustrated in the following distance. The gas pressure results in an axial load on the surface of the turbine resulting in moving it rearwards. In order to achieve the first material interaction, the gap between

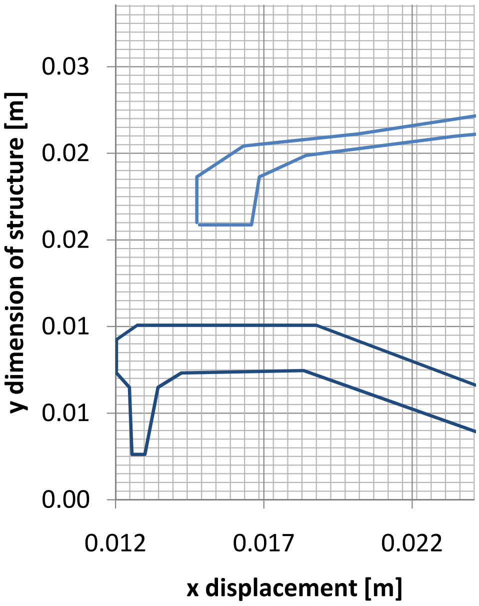

Figure 4.4: y-dimension of the structure versus x-dimension

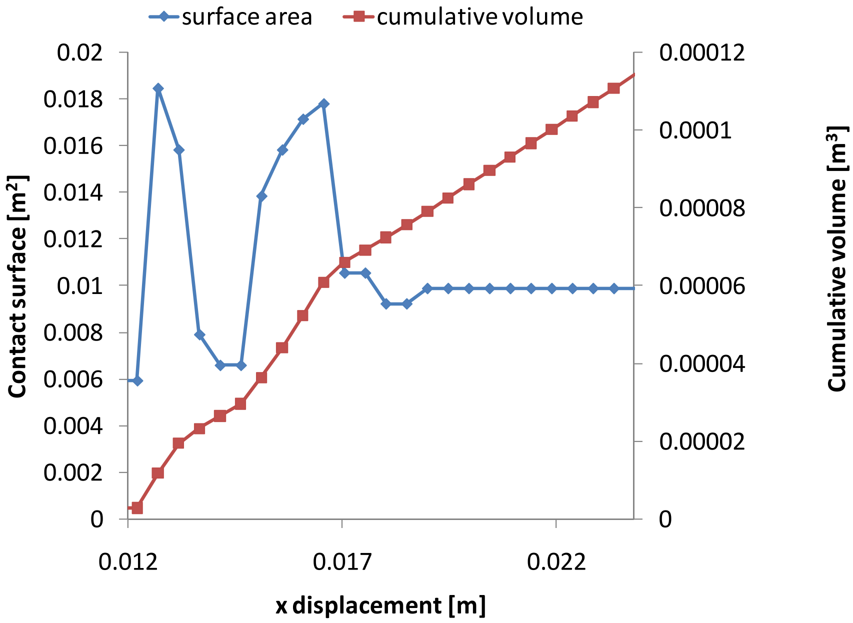

Figure 4.5: Contact surface and cumulative volume at contact against time

the IP turbine and the static arrangement needs to close. The time required to close the gap is few milliseconds due to the very axial load.

In the numerical model, in every time step, the displacement of the turbine before the occurrence of the first contact is simulated as a uniform acceleration in which the velocity of an object changes by an equal amount in every equal time period. In one dimensional analysis, the axial displacement according to the uniform acceleration motion is calculated as:

$$\Delta x_{j+1} = \Delta x_j + \frac{1}{2} \cdot \frac{F_j}{m} \cdot \Delta t^2 \tag{4.13}$$

The mass of the turbine rotor, m, is calculated from the volume of one blade with the corresponding disc section as it is measured from Altair Hypermesh 10.0 multiplied by the density of the nickel alloy (INCONEL 718) and the number of blades. Before the closure of the gap, since there is no material interaction the friction power and as a consequence the friction energy are equal zero.

2. When the first contact interaction occurs, the frictional power is calculated interpolating linearly into the grid of the friction power map using the set of rotational speed and axial load. Based on the friction power estimation, the incremental friction energy is calculated,

$$Q_j = Q_{j-1} + \Delta\dot{Q}_j \cdot \Delta t \tag{4.14}$$

where $\Delta\dot{Q}_j$ is the instant frictional power,

$$\Delta\dot{Q}_j = \frac{\dot{Q}n_j \cdot A_{j-1} \cdot H_o \cdot \alpha}{\sqrt{\frac{A_{j-1}}{\pi}}} \tag{4.15}$$

3. The friction torque is derived through the instant frictional energy and then the driving torque is calculated in order to derive the rotational speed used for the next iteration.

$$T_{fric,j} = \frac{\Delta\dot{Q}_j}{u_j} \tag{4.16}$$

where u_j is the rotational speed

$$u_j = \frac{u_{j-1} \cdot \alpha}{r \cdot \sqrt{\frac{A(j)}{\pi}}} \tag{4.17}$$

Using Eq.4.16, the driving torque and the rotational speed are estimated through Eq.7.5 and Eq.7.6.

$$T_{driv,j} = T_{applied,j} - T_{fric,j} \tag{4.18}$$

$$u_{j+1} = u_j + \frac{T_{driv,j}}{I} \cdot \Delta t \tag{4.19}$$

4. The normalized wear rate is calculated for a given set of normalized load and rotational speed through a linear interpolation among the points of the generic map.

5. After the prediction of the wear rate, the wear prediction is carried out. The melting wear begins when the energy dissipated as heat reaches a certain value that enables the failure criterion of the material to be achieved. As the event progresses, the friction energy that is dissipated as heat between the structures increase the temperature and the stress, strain at the interaction resulting in melting wear. The limit of the failure can be expressed through the frictional power. Therefore, a critical limit for the beginning of the melting wear is established, as derived from the LSDYNA calculations. This value is representative of the mesh size and is stated as a starting point of the melting wear.

   An additional loop is implemented in the code to account for the increase of sliding energy of the structure at every displacement step. The code initiates the boundary condition of the failure when an axial displacement of the IP turbine is achieved. At every displacement, new material of the seal segment comes into contact with the lock-plate. The thermal conductivity of the nickel alloy does not allow the heat diffusion into the material to take place within short periods of time. In addition, the gradient of temperature on axial distance is negligible allowing the calculation of the temperature to be carried out from the initial temperature of the material defined as 1000K. This implies that the friction energy needs to approach and exceed the boundary limit at every displacement so that wear starts. This is an iterative process which is carried out to estimate appropriately the melting wear and the displacement.

When the erosion starts, the calculation of the wear is estimated in accordance to the Eq.4.20

$$W_{j+1} = W_j + W_{n,j} \cdot \frac{u_j}{r \cdot \sqrt{\frac{A_j}{\pi}}} \cdot \alpha \cdot A_j \cdot \rho \cdot r \cdot \Delta t \tag{4.20}$$

6. Displacement of the structure is calculated from the volume that melts away. According to the discretization of the seal segment and platform, when the melting mass approaches and exceeds the volume limit (as defined form the discretization of the structure) further axial displacement occurs. The geometry is imported in terms of cumulative volume and contact area with respect to the displacement. After the impact the cumulative volume loss and thus the axial displacement is estimated in accordance with Eq.4.21 and Eq.4.22, 4.23.

$$V_{j+1} = \frac{W_{j+1}}{\rho} \tag{4.21}$$

$$V_{j+1} \geq V_{cum,xi} \tag{4.22}$$

$$x_{j+1} = x_{i+1} \tag{4.23}$$

4.5 Summary

The idea of a generic modelling methodology able to capture the impact event and wear propagation has been introduced in this chapter. The novelty of such approach is that it combines LSDYNA results with structural analysis calculations in a convenient, time efficient tool that can be easily integrated in other performance tools. The parameters of the generic maps, wear rate, frictional power, load and rotational speed are expressed in a normalised form.

The method adopts a quasi-steady condition in order to calculate the evolution of such transient event. For every time step, values of normalised load and speed, result in a value of wear rate through the use of non-dimensional maps. This wear is, then, translated to axial displacement through an appropriately chosen correlation between volume and axial displacement. Such method allows the prediction of any wear propagation phenomenon, in order to be coupled with a general shaft failure performance code.

5

Methodology verification

Since there is not previously published attempt to investigate the occurrence of turbine clashing, there is little or no knowledge available in the public domain about the modelling of turbines in contact using FEA. As discussed in Chapter 2, FEA have been extensively used in cases of failure on gas turbine components. Nevertheless, most failure scenarios studied like fan blade out or turbine blade fragments occur due to the existence of high stresses and strains, whereas the effect of temperature was considered to be of negligible or less importance for the analyses.

In the investigation of turbines in contact, temperature distribution is considered to be crucial for the structural interaction and wear propagation. Hence, a thermo-mechanical analysis is employed to capture the dynamics of the transient impact phenomenon. The lack of previous knowledge of modelling techniques in such severe impact of turbines in conjunction with the absence of experimental data on the interaction between turbines provoke a troublesome issue in FEA results' evaluation.The answer to the assessment of the modelling emerged from an extensive literature survey in terms of available experimental data of ballistic impact scenarios and pin-on-disc interactions under high sliding velocities.

The main issue is to prove that the modelling approach estimates contact interaction, energy dissipation, movement evolution of the slipping part and wear propagation accurate enough to be trusted. This chapter presents the capability of FEA to estimate accurately the motion of a projectile in the event of the ballistic impact and the propagation of material failure when a pin slides on a disc under high relative velocity. The computational results are compared to experimental data while the modelling techniques are handled as a groundwork and a guide for the avoidance of any modelling errors.

5.1 Pin-on-disc numerical analysis

5.1.1 Background

Pin on disc structural interaction under high speed and loading conditions using a FEA solver is carried out in order to:

- assess the applicability of the dimensionless analysis
- evaluate the capability of the FE tool and the adopted modelling techniques to simulate the friction event and to estimate the wear propagation
- compare the FE results with semi-empirical models and real experiments (available data in public domain) with the aid of dimensionless analysis

Summarizing, the main target of this chapter is to support the applicability of dimensionless analysis. Necessary requirement is to develop a FEA model of pin-on-disc interaction and simulate their friction contact under certain pressure and rotational speed conditions which enable melting wear to be the predominant wear mechanism. Lastly, the FEA results are compared to semi-empirical models and experimental data using the dimensionless form of the basic parameters which are load, rotational speed and wear.

5.1.2 Wear modelling

In the 2nd Chapter, a consistent review of the wear analysis has been included reporting the types of wear. Attention has been drawn on the first wear mechanism maps that has been constructed by (9) in order to indicate the dominant wear mechanism for a given set of conditions. Wear maps correlate a large amount of wear data from the literature(39)(40)(41)(42). Because these wear data come from experiments with different geometries, Lim and Ashby (9) proposed the use of non-dimensional wear, load and sliding speed. In that way it is possible to avoid or at least reduce the influence of the size and geometry of the specimens used in test facilities.

A necessary requirement of having melting wear as a predominant mechanism is the existence of high relative speed and load at the contact interface(43). Experimental investigation of a pin-on-disc interaction in the zone of the melting wear has been performed by Montgomery (34).

The results of the experiments have been used to calibrate the equation of bulk heating of the pin. In more detail, the bulk heating equation has been derived from the heat generation at the interface due to rubbing and the heat flux inside the structures as a result of heat conduction(44). The heat generated per unit area due to friction is calculated from:

$$\dot{Q} = \frac{\mu \cdot F \cdot v}{A_n} \tag{5.1}$$

where μ is the friction coefficient which decreases exponentially with increasing rotational speed. A part of this heat diffuses into the pin while the rest penetrates into the structure of the rotating disc. A fraction of the heat entering the pin, diffuses into its contact surface while the remaining is conducted into the body of the pin. It can be assumed that after an initial transient condition, the temperature in the pin settles down at the steady state distribution which can be calculated from the first law of heat flow. In a way of simplicity, it is not far from reality to linearize the problem, so that the heat flux can be easily calculated through the following equation :

$$\dot{Q_{hf}} \approx k \cdot \left(\frac{T_b - T_o}{l_b} \right) \tag{5.2}$$

Equation 5.2 represents a linear dependency of heat flux from the temperature increase on the pin. The thermal conductivity, k, and the equivalent linear diffusion distance, l_b. The parameter l_b is indicative of the distance from the contact interface where the heat has been diffused. Using this equation, it is easy to calculate the limits of melting zone by substitute $T_b = T_{melt}$ (33). The melting zone area calculated for pure iron can be seen is Fig.5.1.

Considering Eq.5.1 and 5.2, the bulk temperature of the pin can be provided by equation:

$$T_b = T_o + \left(\frac{\alpha \cdot \mu \cdot F \cdot v \cdot l_b}{A_n \cdot k} \right) \tag{5.3}$$

The parameter α represents the fraction of heat flowing into the pin and is calculated by :

$$\alpha = \frac{1}{2 + l_b \cdot \left(\frac{\pi \cdot v}{8 \cdot a \cdot r_o} \right)^{1/2}} \tag{5.4}$$

The elevated temperature of the contact surface of the pin leads to localized melting. A film of liquid metal is formed at the sliding interface providing some sort of 'melt lubrication'. The friction coefficient of the material drops to low values. In an experimental arrangement, the liquid layer supports the normal load through the hydrodynamic mechanism, however the heat produced because of viscous work and the layer, continues to melt more solid gaining high values of wear rate at even low friction coefficient. Therefore, in case of melting wear the equation of heat flux on the pin can be expressed as equal to the heat conducted into the part of the pin and the heat absorbed as latent heat in melting a volume per second at the sliding interface. The heat flow equation can be modified to:

$$\alpha \dot{Q} = -k \cdot \nabla T + L \cdot \frac{V_m}{A_n} \tag{5.5}$$

where $\alpha \dot{Q}$: the rate of frictional heat input into the pin, $-k \cdot \nabla T$: the rate of heat conduction into the pin, $L \cdot \frac{V_m}{A_n}$: the rate of heat absorption by the melting material.

Based on energy balance presented by Eq.5.5, it is possible to gain the quantity of the melted material.

Fig.5.1 shows the data that Lim and Ashby (9) gathered for the dry wear of steels and later used to calibrate the mathematical above presented mathematical models.

5.1.3 Finite element model

The geometric characteristics and the boundaries of finite element reflect a common experimental apparatus of a high speed pin-on-disc test device as illustrated

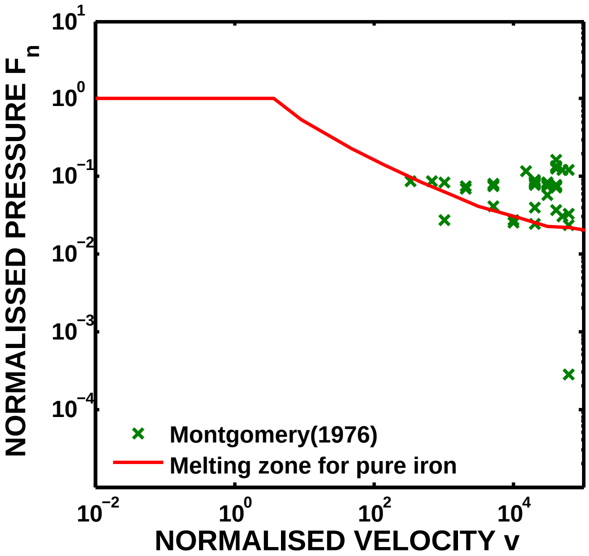

Figure 5.1: Melting zone with respect to normalized pressure and velocity

in Fig.5.2(a) and 5.2(b). The radius of the pin is 1mm while the radius of the disc is equal to 20mm. The disc rotates under a constant speed while the loads on the pin were applied by means of pressure at the surface.(The input file is provided in Appendix A)

Based upon the geometric characteristics of the pin-on-disc, the finite element model of Fig.5.3 is developed. Figure 5.3 illustrates the geometry and the meshing of the pin-on-disc model as developed in a high-performance finite element preprocessor tool, Altair HyperMesh 10.0. The dimension of the structure demands the development of very fine mesh. The volume of each element approximates the value of 8.567e-013 m^3.

During the structural interaction, part of the friction heat is dissipated into the pin, increasing its stresses and temperature, while the rest diffuses into the disc. The surface of the pin is highly deformed and overheated due to contact interaction leading to material loss. Hence, the model of the pin is modelled as a deformable body that accounts for pressure distribution, stresses and strains. In more detail,as observed in Fig.5.3, the pin model is divided into two component models, which are connected at their interface through shared nodes. The part

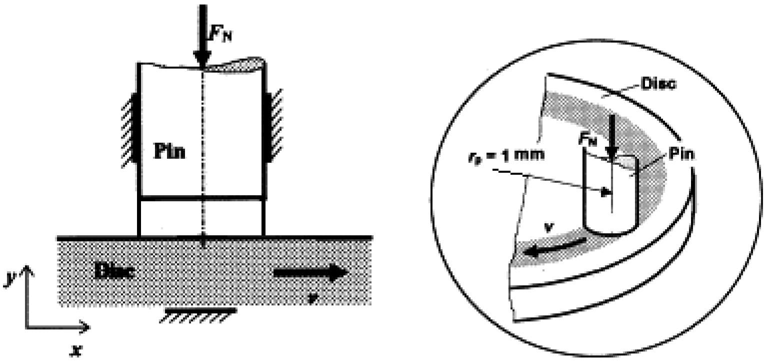

(a) Pin on disc schematic - 2D (b) Pin on disc schematic - 3D

Figure 5.2: Pin-on-disc schematics based on experimental apparatus

Property	**Unit**	**Value**
thermal conductivity	$W/(mK)$	41
thermal diffusivity	m^2/sec	9.1 E-06
volume thermal capacity	$J/(m^3K)$	4.5 e+06
melting point	K	1800
latent heat of melting	J/m^3	2.1 E+09
hardness	GPa	1 E+09
density	kg/m^3	7.8 E+03

Table 5.1: Material properties

of the pin whose surface interacts with the disc is accompanied by the Johnson-Cook constitutive model to capture the wear propagation based on its failure criterion. The second component of the pin is defined as a non-deformable structure and corresponds to the upper part of the pin which is clamped in case of an experimental arrangement to prevent any translation or rotation.

Figure 5.3: Pin-on-disc geometric model

Additionally, the disc rotates at a high rotational speed diffusing the friction heat in larger contact area. Therefore, the surface of the disc remains almost unaffected in terms of stress and strain. For this reason, the disc can be modelled as a rigid body.

Lastly, a thermal material model is defined in the FE model of pin-on-disc to specify thermal properties of the structures (Table 5.1) so that the temperature distribution and its effect on wear propagation can be quantified through the analysis.

The sliding contact at the disc-to-pin interface is modelled by a set of master elements of the disc and a set of slave elements of the pin (§2.3.1). The approach of the modelling of contact in LSDYNA solver is the one presented in Chapter 3 (§3.2.1). Considering the boundary conditions applied on the structures, a constant prescribed rotational speed is applied on the rigid disc and a constant distributed pressure load acts on the set of elements of the upper surface of the pin as observed in Fig.5.2(a).

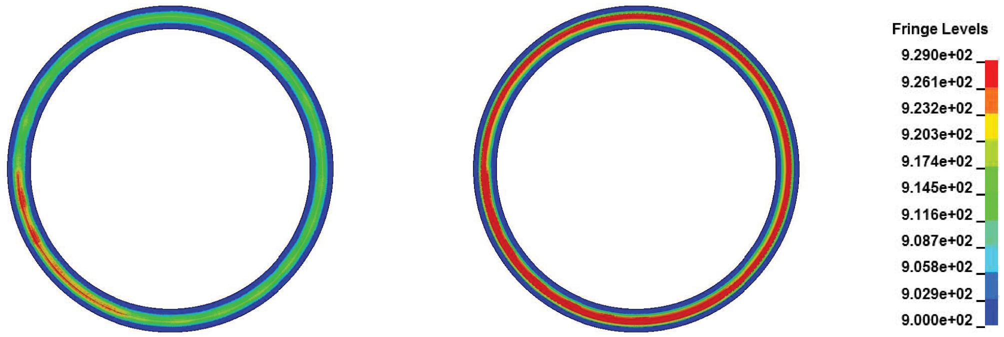

(a) Nodes' temperature on disc at time 3e-04 (b) Nodes' temperature on disc at time 10e-04

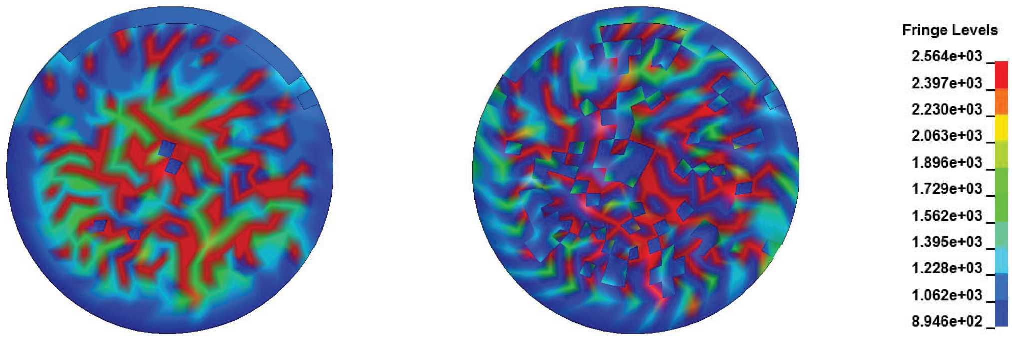

(c) Nodes' temperature on pin at time 3e-04 (d) Nodes' temperature on pin at time 10e-04

Figure 5.4: FEA results of pin-on-disc

5.1.4 FE solver calculation

FE simulations are performed for a few sets of normalized loads and rotational speeds which correspond to the melting zone as depicted in Fig.5.1. Simulation results are described when the normalized pressure is equal to $1.00e - 01$ while the normalized rotational speed is $8.05e + 04$.

To investigate the evolution of heat dissipated between the structure as a results of friction, two snap-shots showing the temperature distribution on the surfaces of the bodies are depicted in Fig.5.4(a),5.4(b),5.4(c),5.4(d). The snap-shots correspond to a time of $3\ e - 04$ sec and $1\ e - 03$ after the beginning of the friction event, relatively. It is evident through the temperature field distribution circumferential of the disc that the time is enough for the disc to complete a number of revolutions. It is evident that there is a negligible increase in the nodes'temperature of the disc. On the other hand, the rubbing on the surface of the pin results in a considerable increase in temperature so that the pin achieves the material failure criterion (Johnson-Cook material presented in §3.2.2). This outcome is expected since a point on the surface on the disc has heat injected into it only for the interaction time (: the time required for a point to slide across the diameter of the pin) whereas the pin receives heat all the time increasing continuously its temperature.

As the event moves on , the temperature field on the disc changes. The number of revolutions indicates a continuous rise on the temperature distribution due to the increase of injected heat into it. In terms of the pin, the elements that achieve the failure criterion of the material which is a function of stress, strain, strain rate and temperature, are deleted from the calculation. This means that the deleted elements are not accounted in the FEA calculation letting the remaining elements to receive the heat.

After 3e-04sec, a few elements have been deleted and removed from calculations, hence the temperature has a uniform distribution particular at the center of the pin. As the events progresses, elements of the contact surface of the pin exceed the threshold of the failure criterion and are deleted from the contact surface of the pin making visible the row of the elements behind them. The second row of elements is not involve in the contact and, thus, energy is transfered to them only through conduction, hence, the element temperature is much lower compared to the elements on the surface. Therefore, the excessive temperature is concentrated at the remaining element while the low temperature fields is indicative of failure occurrence.

The change of temperature within the material as a result of the heat flux of the pin is illustrated in Fig.5.5. At the contact interface the heat dissipated due to friction elevates quickly the mean surface temperature of the pin only within a few milliseconds. Comparing the temperature between two different periods, 0.03 and 1 msec, a diversity is noticeable mainly at the interface contact while the effect of energy dissipated as heat has less effect as the distance from contact area increases.

Figure 5.6 represents the change in volume during the rubbing process. It

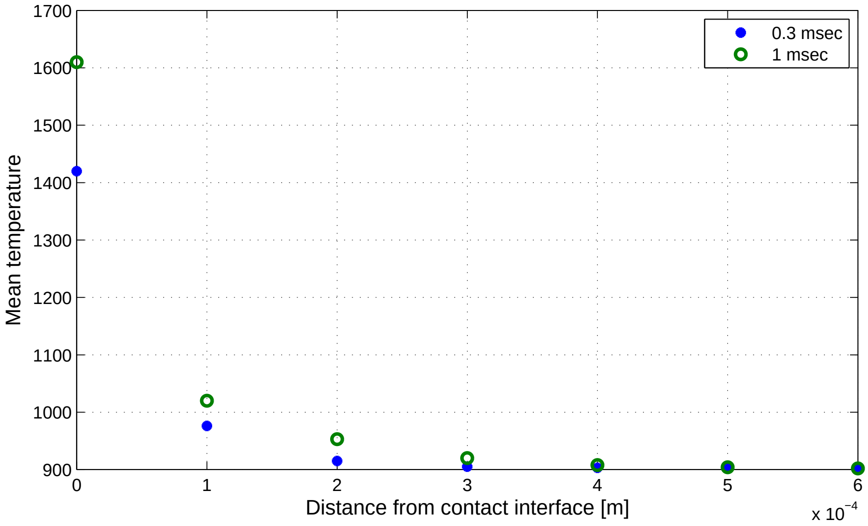

Figure 5.5: Mean temperature on different distances form the contact area

can be observed that the volume decreases linearly with time, so that the non-dimensional wear (Eq.2.13) is easily estimated from the simulations.

The use of normalised parameters have the potential to compare results of LSDYNA model of varying geometric features. High rotational speed and high loading conditions have been imposed on the pin-on-disc model in order to capture the failure of the material due to the existence of high temperature apart for the effect of high stresses and strains. The speed criterion is a parameter of high effect on the simulations. Since the existence the high relative velocity between the structures indicates that there is insufficient time for an equilibrium condition to be established.

5.1.5 Non-Dimensional maps

A number of simulations, like the one presented above, are carried out using constant pressure acting on the pin and a constant rotational speed on the disc.

The area of wear zone which is links to the shaft failure event and the interaction between turbines is the melting zone. High temperature distribution force the material to melt away and to develop a lubrication surfaces on the sliding interface affecting the friction coefficient value.

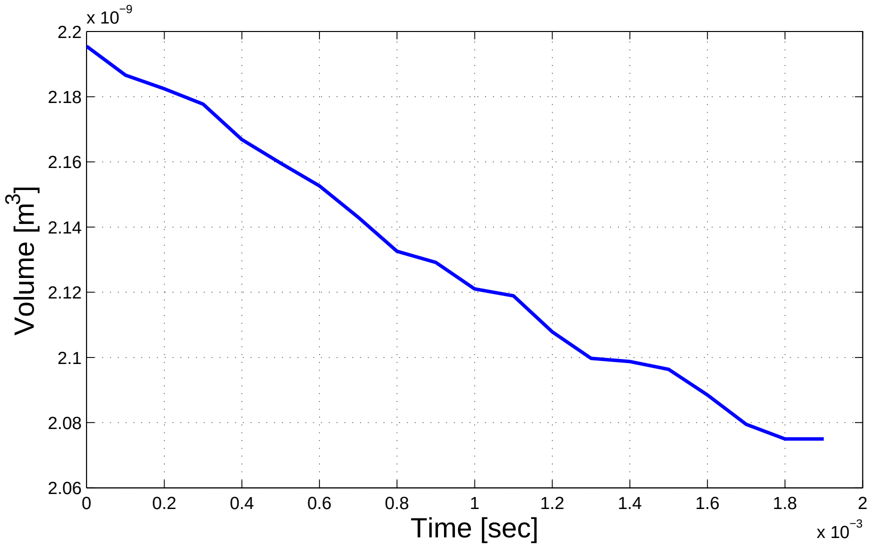

Figure 5.6: Volume change against time

The set of steady input conditions of load and relative velocity are imposed on the pin-on-disc model. To capture the wear propagation due to melting, these numerical experiments have been carried out under load and relative speed. Random set of condition are selected and presented in Fig.5.7. Based on these, coupled thermo-mechanical simulations are run and the non-dimensional map of the normalized wear rate against normalised load and rotational speed are shown is Fig.5.8. The normalized values have been derived using the Eq.2.13-2.15. The results of the wear rate calculated through the LSDYNA simulations are in good agreement with the 1D model calibrate with experimental data (9)(34)(40)as it can be observed in Fig.5.8. The testing of the pin-on-disc geometry has indicated that a very similar simulation methodology can be applied to other geometries as well, relevant to the objectives of this work.

5.2 Ballistic scenarios

5.2.1 Background

In the past, scientists tried to simulate the effect of uncontained engine debris impacts on aircraft fuselage-like skin panels studying the penetration of aluminium

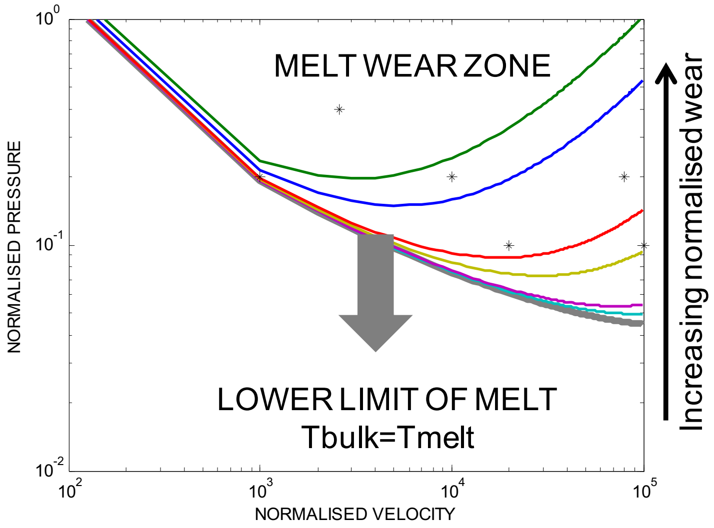

Figure 5.7: Cases simulated using LSDYNA belonging to melting wear zone

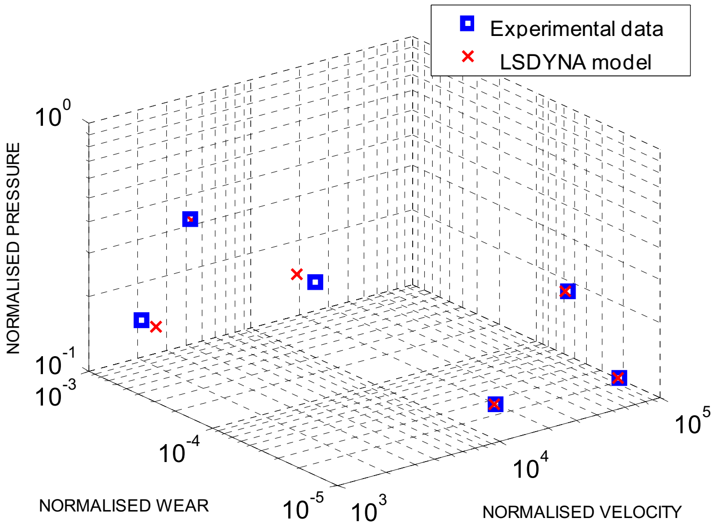

Figure 5.8: Comparison between numerical model calibrated with experimental data provided by Ashby(9) and LSDYNA simulation for pin on disc

plate impacted by titanium impactors. A failed rotating component in a gas turbine engine can release high energy fragments which can be illustrated as a projectile impacting on a target. The target plays the role of the engine containment and the aim was mainly to investigate the possibility of penetration. The penetration capability of the material released depended on a number of parameters as projectile's kinetic energy, material of the structures, shape, and orientation of impact. Experimental results of target-projectile interaction are provided by a number of papers reported in the public domain.(12)(45)(26)(13)(17)

In the case of stators' and rotors' interaction, the components of the rotors can be illustrated as a high energy projectile impacting on the target which plays the role of the stators. Different approaches of the material interaction are followed and compared to the provided experimental data. The main target is to eliminate any possibility of inaccuracy in the FE analysis results by investigating possible modelling techniques.

5.2.2 FE model description

Finite element modelling of the spatial domain(12) needs to be sufficient enough to represent the geometry of the structure and to capture the structural response after the high velocity impact of the fragment on target-fuselage. The demand for the appropriate selection of the simulation parameters becomes a major issue in order to ensure accuracy and robustness of the solution.

Figure 5.9 depicts the meshing of the target and the impactor. The mesh size is considerable small a t the area of the impact to avoid any numerical errors caused by mesh density.

The finite element modelling strategy is essential to examine contact and material modelling for the impact and penetration. In all cases, the simulation model involves three components: impactor, text fixture frame and target plate. The finite element models use the standard 8-node integration with single point integration and default settings for hourglass control(Appendix A).

1. Impactor:The impactor is modelled using 8-node solid element with an elastic-plastic strain hardening material model. The initial position of the impactor is positioned 0.0625in away from the target and it has a predefined

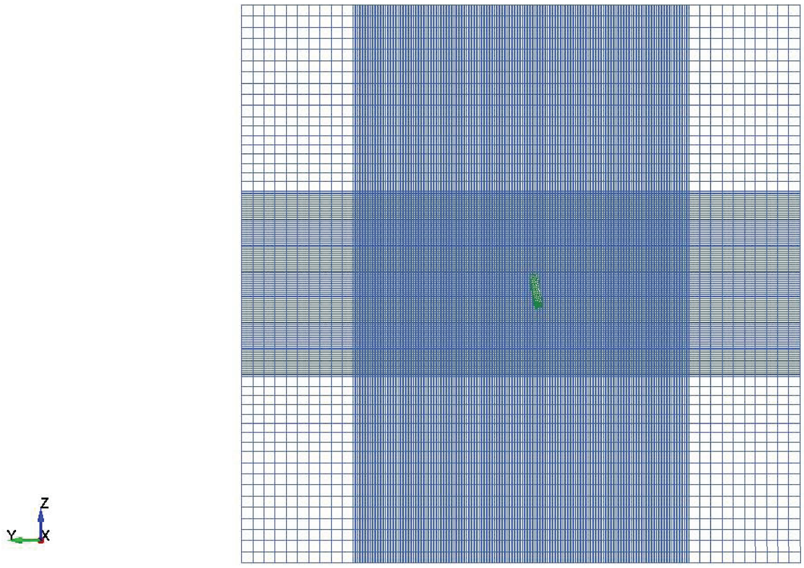

Figure 5.9: Meshing of the target

orientation. Impactor is made of titanium and the material properties are reported in the Table5.2.

2. Frame:The frame is also modelled with 8-node solid elements with an elastic strain hardening material. The frame has a lower and an upper part which are assembled to clamp down on the target plate. It is made of titanium. The outer border of the frame is 6.0in on each side with a clamping border 0.375in wide. Boundary conditions are applied on the nodes in the test frame to prevent any motion.
3. Target Plate:The target plate is modelled using also 8-node solid element with an elastic-plastic strain hardening material model.

5.2.3 Model validation

Figure 5.10 represents LSDYNA results simulating ballistic impact and compares them with available in literature experimental data. In some cases, it is not apparent from the beginning that the modelling approach includes considerable errors. Although the displacement differences of the impactor simulated by the

Material	**Titanium**	**Aluminium**	**Steel**
Young's modulus	$16.0Msi$	$10.0Msi$	$30.0Msi$
Poisson's ratio	0.30	0.30	0.30
Yield strength	$0.12Msi$	$0.05Msi$	$0.35Msi$
Hardening modulus	$0.30Msi$	$0.10Msi$	$0.15Msi$
Hardening parameter	0.20	0.20	0.23
Weight density	$0.16lb/in^3$	$0.10b/in^3$	$0.28lb/in^3$
Ultimate strain to failure	–	$0.2in/in$	–

Table 5.2: Material characteristics of impactor,target plate and frame(11)

three cases are not substantial, the indication of possible fault in calculations comes up with the representation of velocity and kinetic energy. In these plots, the declination between simulation results and experimental data is illustrated in Fig.5.10. Therefore, special attention is required to distinguish any faults that may assign uncertainty in the results of the simulation.

Two example of 'bad' simulation approach are presented. In the first scenario the parameters' selection of the contact algorithm allows the penetration of the impactor without any failure occurrence on the structure of the target as depicted in Fig.5.11. This is called 'soft' penetration and the axial velocity of the impactor after the impact is overestimated due to the decreased resistance of the target with a consequence increase in axial displacement and kinetic energy while the internal energy of the target is decreased. This 'soft' response of the target is connected to a low value of contact stiffness parameter, k.(as it is defined in §2.3.1)

The second scenario includes the case of element inter penetration. Failure is achieved in the structure of the target due to excessive strain however there is element inter penetration as depicted in Fig.5.12 which decelerates the impactor and leads to underestimation of the axial velocity at the end of the simulation time. This response is linked to the definition of the contact algorithm showing the importance of choosing the most appropriate conditions for the contact interaction.

The results of the final case are depicted in Fig.5.13 and 5.14. The strain distribution and the fracture of the target are shown. The final case achieves good agreement with the experimental data from public domain.

In this manner, experimental data of ballistic tests are used to assess the turbines' interaction after a shaft failure. In the case of stators' and rotors' interaction, the components of the rotors can be illustrated as a high energy projectile impacting on the target which plays the role of the stators. Different approaches of the material interaction are followed and compared to the provided experimental data. The main target is to eliminate any possibility of inaccuracy in the FE analysis results by investigating the effect of imposed boundary conditions.

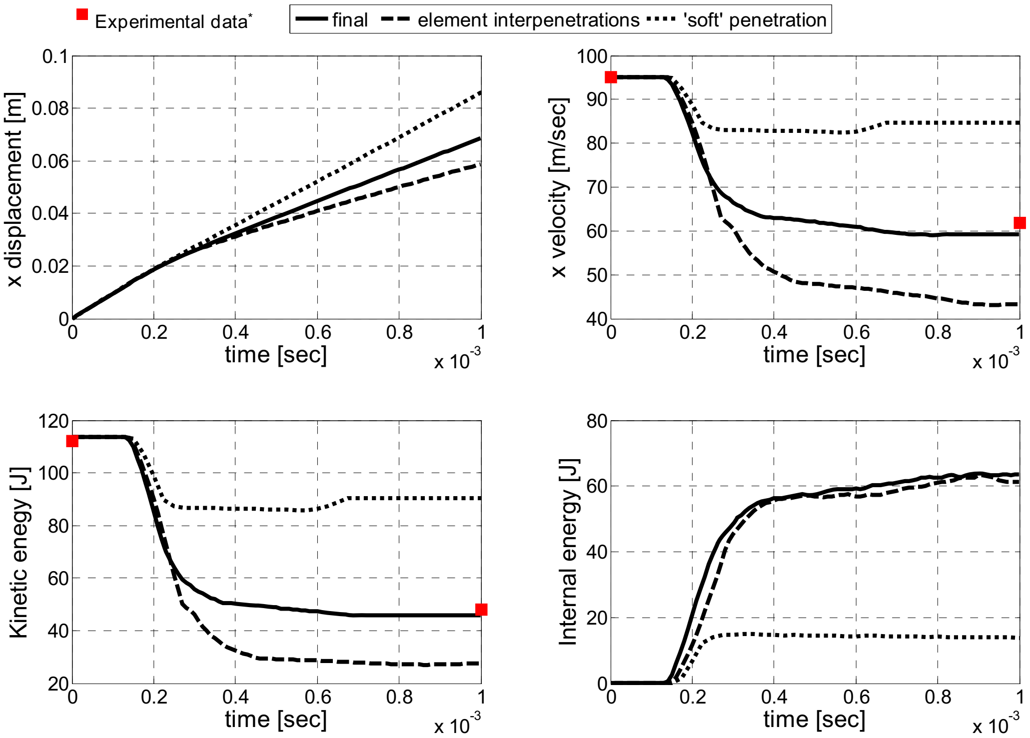

Figure 5.10: Results of ballistic impact; displacement, axial velocity, kinetic energy, internal energy with respect to time; experimental data are given from (11, 12)

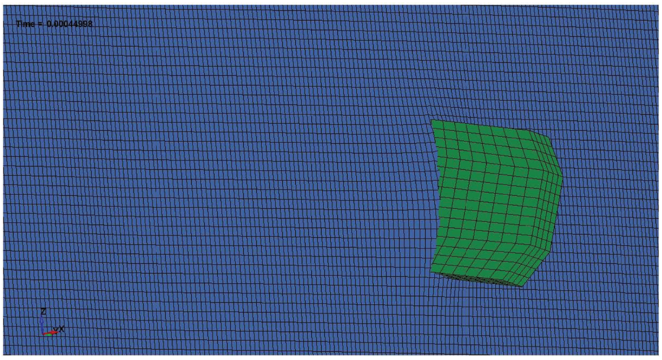

Figure 5.11: Scenario of soft penetration

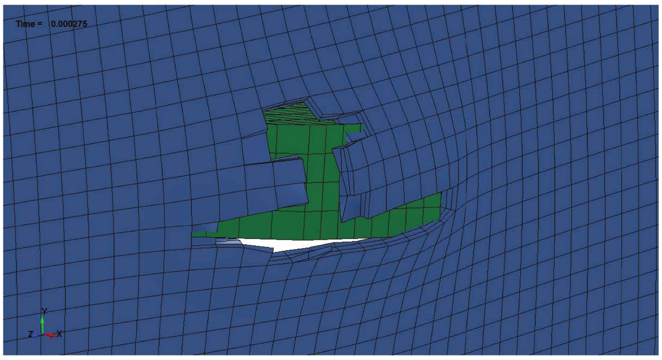

Figure 5.12: Scenario of element interpenetration

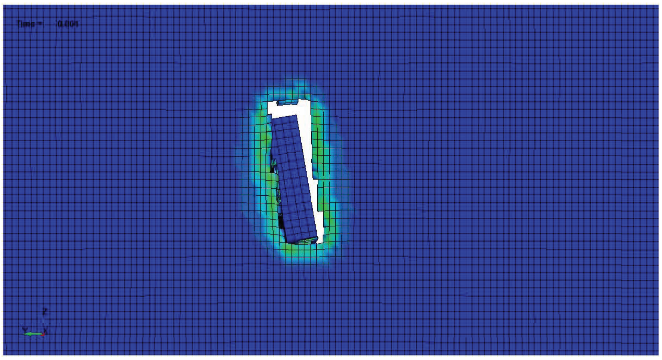

Figure 5.13: Final scenario-Contours of strain

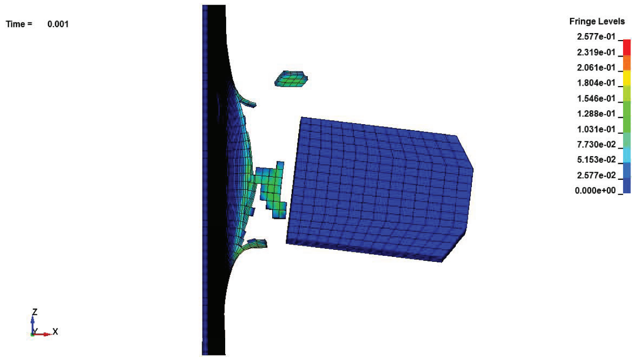

Figure 5.14: Final scenario-Contours of strain

5.3 Summary

This chapter exhibits the capability of LSDYNA to predict failure phenomena that include structural wear due to friction and impact. Two structural models have been developed LSDYNA and tested against experimental studies. In the first case, LSDYNA has been used to confirm Lim and Ashby's model and the results showed a good agreement between theoretical and numerical approaches. In a similar fashion, LSDYNA captured the effects of impact when compared against experimental data of a ballistic scenario, including target penetration. Evidently, LSDYNA exhibited its applicability to the shaft failure scenarios of the present thesis.

6

Wear propagation

The most challenging part in the investigation of turbines in contact is the estimation of wear propagation, particularly, in the region of lock-plate to seal segment interaction since it determines the occurrence of blade tangling. The prediction of wear propagation through experimental arrangement is almost prohibitive due to its expense. On the other hand, the breakthrough of the FE analysis tools and the continuous increase in computational resources encourage the use of FEA for the estimation of wear rate.

In this section, the estimation of wear rate and frictional power through FEA are presented as well as the effect of some critical parameters. The derived maps are used as a database in the generic model introduced in Chapter 4.

6.1 Design of the wear maps

Wear is analyzed as a dynamic process and, in the current analysis, plays the role of the dependent variable. The wear rate changes with respect to a set of independent variables defined by the FEA user. Generally, it is representative of the load acting on the contact surfaces, the relative speed between the structures, the initial temperature of the material and the material properties as it shown in Eq.6.1.

$$Wearrate = f\left(Load, Velocity, Initial\ Temperature, Material\ Characteristics\right) \tag{6.1}$$

In sliding contacts of turbines in contact, the primary parameters affecting wear propagation consist of the load and the relative speed while the factors of initial temperature and material type are considered to be of a secondary effect and are held constant in order to create the wear maps. Although, parametric studies showed that there is a connection between the initial temperature of the material and the wear propagation (increasing value of initial material temperature accelerates the progress of wear), in the performed analysis the value of 1000K is considered for the nickel alloy according to (46). Regarding the material type, nickel alloy is employed for the current experiments, however wear and friction maps can also be derived for other material such as steel.

In this manner, LSDYNA simulation of a set of independent variables are carried out to construct the wear and the friction power maps which are used as as database in WENSAT for the investigation of the complete transient event of turbines in contact.

6.2 FEA results of wear rate and friction power

6.2.1 Definition of wear coefficient using FEA

A number of LSDYNA simulations are carried out with identical values of the initial temperature and material characteristics. For every set of constant load and relative speed, a unique value of wear rate is determined. This wear rate is calculated through the results of mass loss due to the sliding contact between a rotating and a stationary structure.

According to the wear definition of Eq.6.1, it is evident that there is a bond between the wear rate and the rate of heat generation defined as the product of friction coefficient with load and velocity. Therefore, the result of the wear rate for the numerical experiments can be illustrated in a plot. The use of a non-dimensional form of load and speed is applied in order to express the values independently of geometric and material characteristics. The non-dimensional form of load and speed are called otherwise normalised values.Figure 6.1 represents the points of normalised wear rate with respect to the normalized friction power.

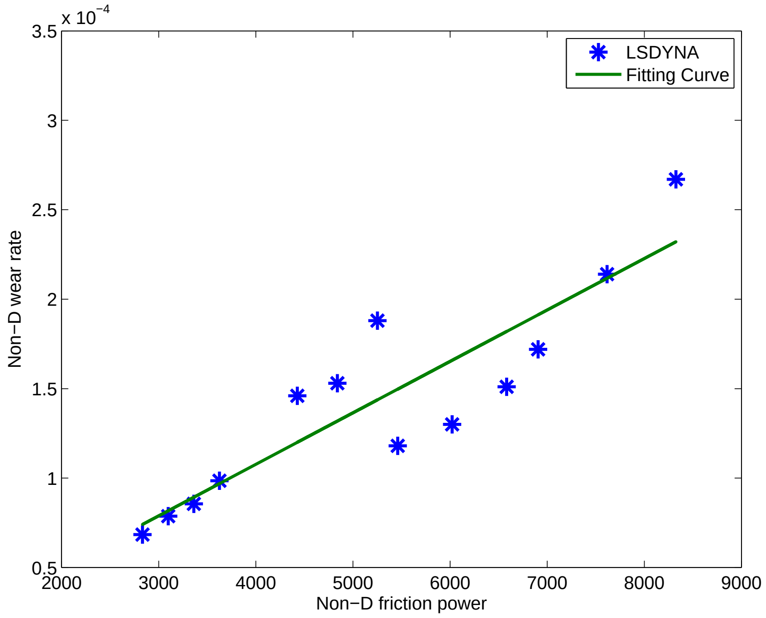

Figure 6.1: Normalized wear rate with respect to the normalized friction

It is noticed that a rise in heat generation causes an increase in the wear rate. Considering Archard's wear law(39), the wear rate at any point on the contact surface is proportional to the local contact pressure and the relative sliding velocity. Consequently, following the same pattern the non-dimensional wear rate can be defined as a linear function of non-dimensional heat generation.

In more detail, regression analysis is employed to define how the typical value of the normalized wear rate changes when the normalized friction power is varied. The numerical results of normalized wear rate can be well fitted by a linear curve according to Eq.6.2.

$$W_n = C\dot{Q}_n \tag{6.2}$$

The constant C can be called wear coefficient and it is indicative of the material properties, friction coefficient and initial temperature of the material.

The wear coefficient is derived from a range of FEA simulation of high sliding speed and loads presented by asterisks in Fig.6.1. The dominant wear mechanism under these conditions is the surface melting by the reason of an excessive increase in the heat surface flux and a subsequence rise in surface temperature. Based on the constitutive model, represented in §3.2.2, the temperature in conjunction with the stresses and the strain rate of the material are responsible for the wear propagation on the structure.

The temperature seems to have a predominant effect on the interaction under high loads and speed conditions as derived from Fig.6.2. The increase of the mean temperature at the contact interface is depicted for three different loads while the rotational speed is held constant. Only a few milliseconds are enough to increase the temperature at the surface to approach the melting point of the material. When Johnson Cook failure criterion is achieved accounting for surface temperature, mass removal through element deletion takes place. The remaining elements on the interface contact continue receiving energy from the rubbing increasing their stress and their temperature as the rubbing process evolves.

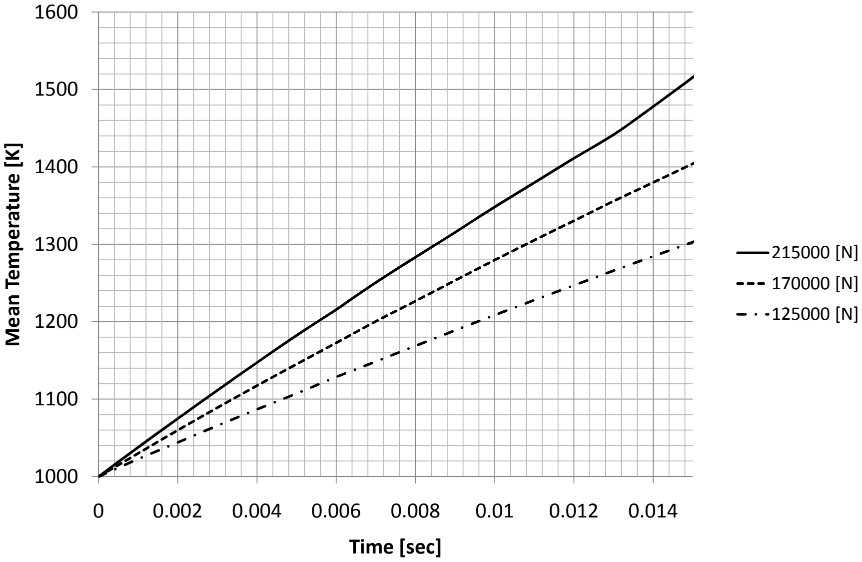

Figure 6.2: Mean temperature on the surface of the seal segment for different load at constant rotational speed of 805 rad/sec

6.2.2 Effect of friction coefficient

Friction coefficient has a critical role in wear propagation and friction power. When two structures rub on each other, the friction coefficient is representative of the material type, as well as the relative speed and the temperature on the contact interface. In case of melting, the friction coefficient at the rubbing interface decreases due to the material layer on the surfaces which act as a lubricant. The estimation of the friction coefficient requires experimental investigation of the behaviour of the rubbing material under certain conditions of rotational speed. Experimental results on the friction coefficient for nickel alloys are reported in (46). The friction coefficient of the nickel alloy is equal to 0.067 when the rubbing occurs at high temperatures and, thus, relative speed.

Apart from the maps of friction coefficient 0.067, additional maps of friction coefficient of 0.1 are developed based on numerous LSDYNA simulations. The developing these maps targets at studying the effect of the friction coefficient on the wear rate and evaluating the possibility of developing any correlations of wear rate maps for different friction coefficients in order to update the database of the generic model. Furthermore, in case of the frictional power maps, there is a linear dependency of heating/dissipated power on the friction coefficient value. In order to show the effect of the friction coefficient comparable plots of wear rate and friction power maps are presented.

The methodology showed in §6.2.1 is followed to derive the wear coefficient from FEA simulations. A wide range of LSDYNA simulations of steady input conditions are carried out. Every point in Fig.6.3 represents the wear rate of a single FE simulation. The linear curve approximates the results of the FE analysis. The inclination of the wear rate against friction power for the friction coefficient of 0.1 is higher than 0.067 showed in Fig.6.1, implying that the wear propagation is quicker.

The increase in frictional power as derived from FEA with respect to normalized load and rotational speed is illustrated in Fig.6.4 and Fig.6.5 correspondingly for friction coefficient equal to 0.1 and 0.0067. Due to thee linear dependency of power on the friction coefficient, the derived surface of the $\mu = 0.1$ is shifted over

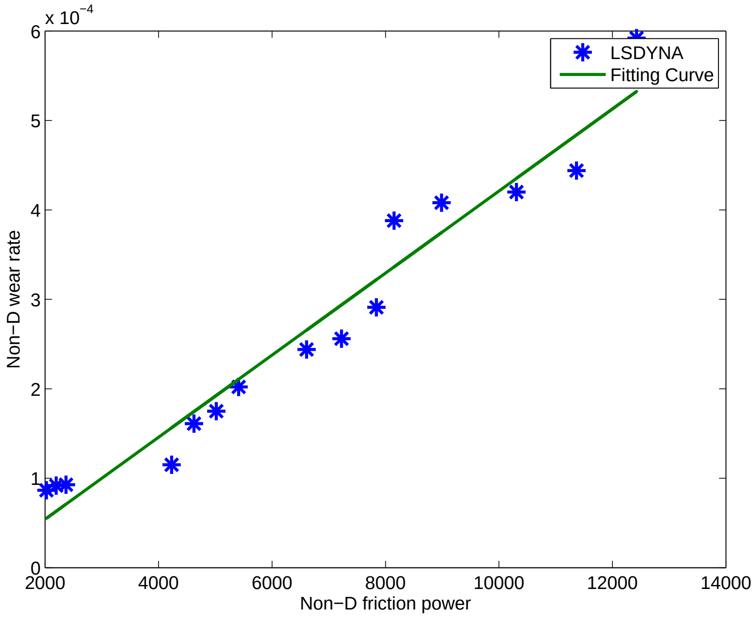

Figure 6.3: Normalized wear rate with respect to the normalized friction

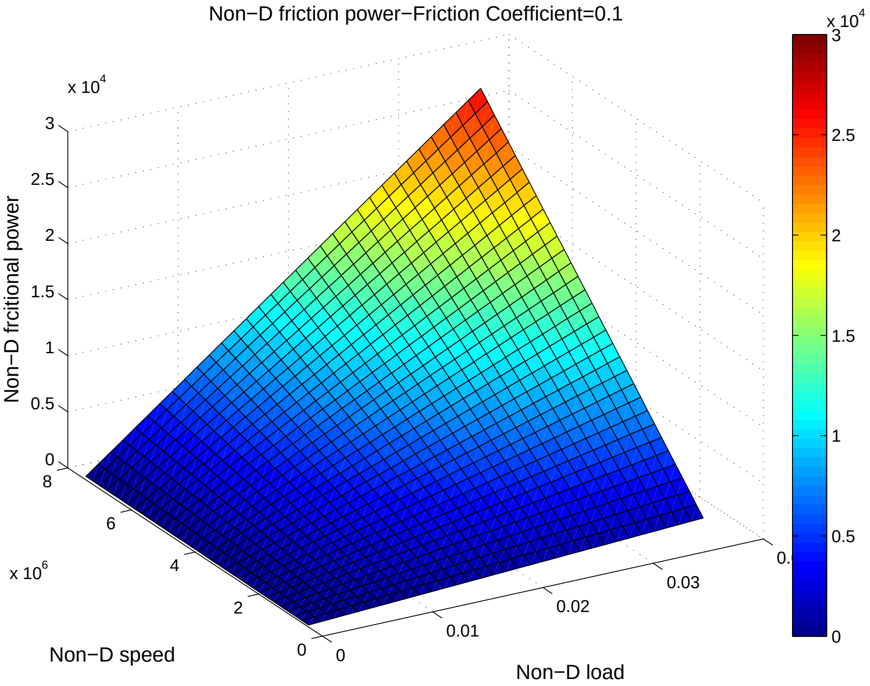

Figure 6.4: Non-dimensional friction power for friction coefficient 0.1

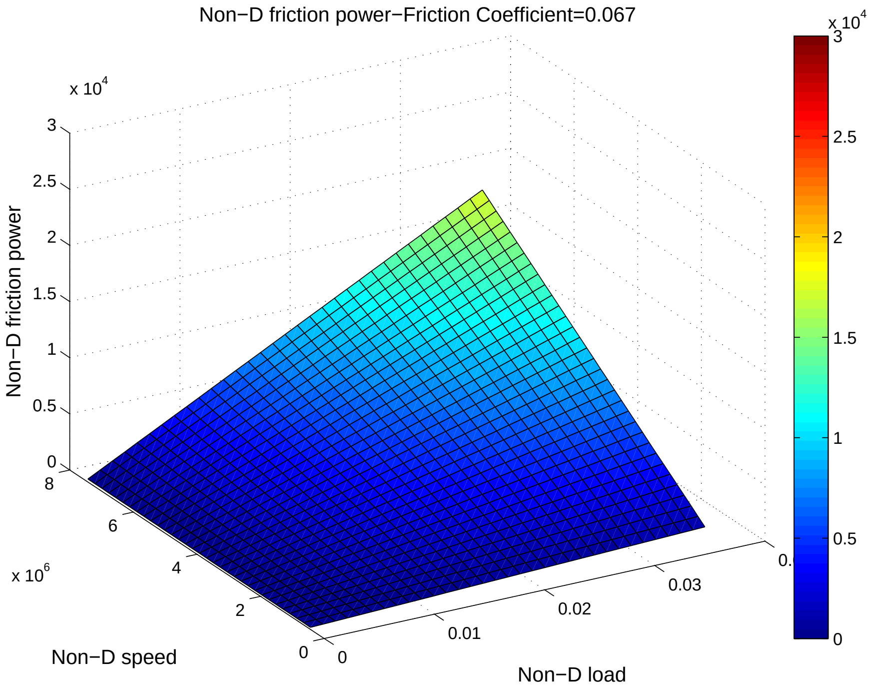

Figure 6.5: Non-dimensional friction power for friction coefficient 0.067

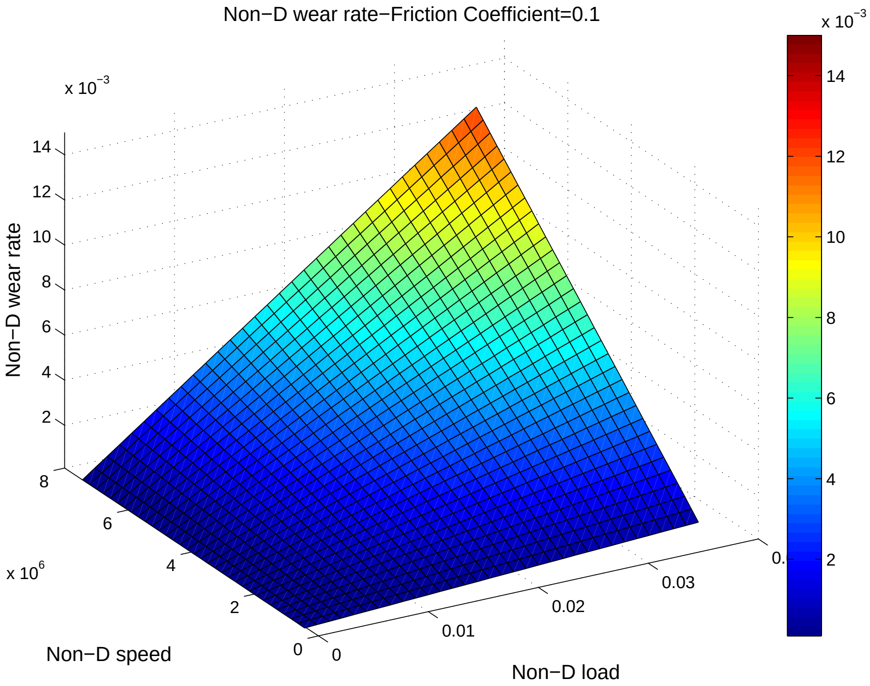

Figure 6.6: Non-dimensional wear rate for friction coefficient 0.1

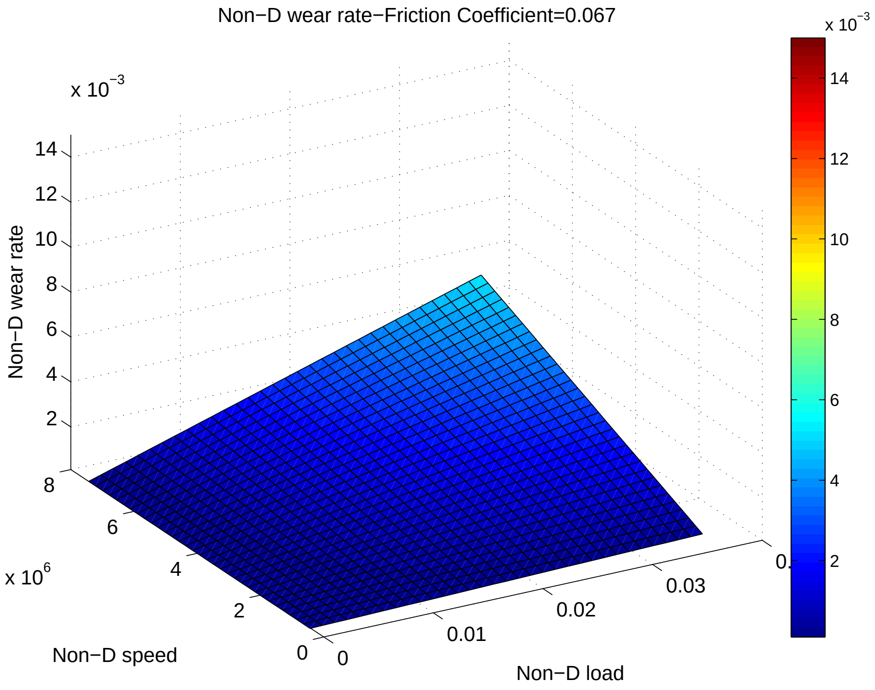

Figure 6.7: Non-dimensional wear rate for friction coefficient 0.067

the surface of $\mu = 0.067$ and reaches 33% higher values of friction power for the same normalized load and rotational speed.

In terms of the wear propagation, the 3D curves of non-dimensional wear rate against rotational speed and load are showed in Fig.6.6 and Fig.6.7. The case of the wear rate differentiates from friction power; increase in friction coefficient does not have a linear change in wear rate as it is appeared with friction. To have a better visualisation of the results, Figure 6.8 depicts the non-dimensional wear rate ratio $R = \dot{W}_{n,\mu=0.1}/\dot{W}_{n,\mu=0.067}$ against rotational speed and load. It is apparent that the parameters of load and rotational speed influence the evolution of wear. In particular, elevated values of these parameters accelerate the progression of wear further. Wear rate is affected by a combination of parameters and one of these is friction coefficient.

The interest should be dropped in the case of turbines in contact. The friction coefficient is basically defined by the material properties as well as the relative speed between the materials in contact and the subsequent temperature increase resulting in melting wear and the use of the melted material as lubricant between the contact areas. In the event of the turbines in contact, the high relative speed advises the use of a value of friction coefficient close to 0.067. Although, a friction coefficient equal to 0.1 is an extreme case, it demonstrates the effect of the friction coefficient in the cases of high rotational speed and load which are experienced during the first few milliseconds of the contact interaction between the turbine structures. Further FEA simulation can be carried out in order to provide correlations between the friction coefficient and the wear rate providing values ± 1-2% of 0.067 and update the maps. However, it is not believed that they will introduce more accurate resuls in the prediction of blade tangling occurence if experimental studies are not carried out for different relative speeds between areas in contact.

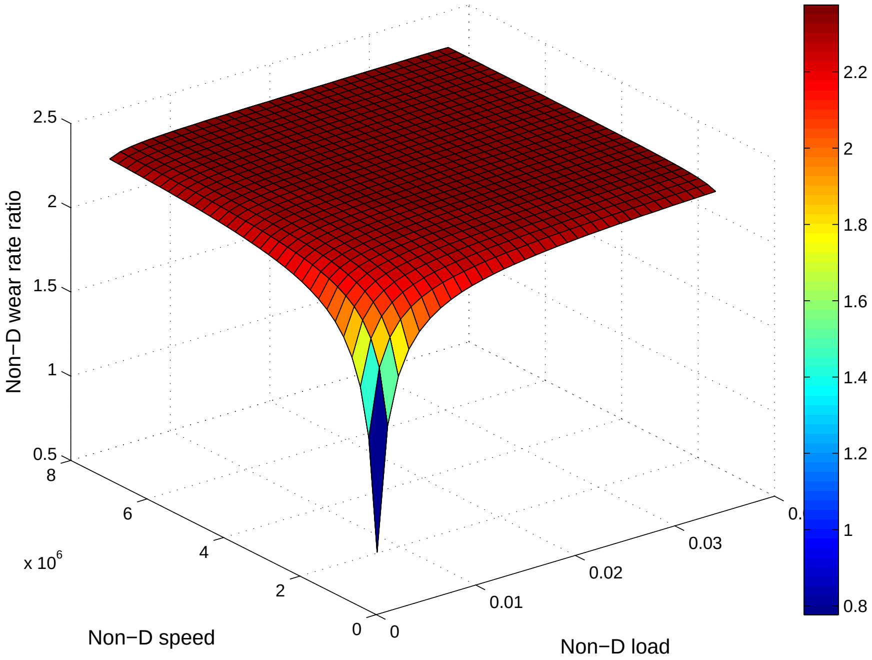

Figure 6.8: Wear rate ratio

6.2.3 Effect of inelastic collision

In the previous maps, the attention is drawn on the sliding interaction between the structures. Except for the sliding interaction, there is also the effect of the inelastic collision. The structures have an initial distance and the free rotor at the time of the contact gains an axial. The analysis of structural interaction becomes more challenging when apart from the rubbing between the structure, the high velocity impact between the structures needs to be included in the solution. Considering the interaction between turbines, there is a initial gap between the turbines before the shaft failure. At the moment the turbine is released and moves rearwards, the gas pressure difference imposes an acceleration on the turbine. Considering the distance and the imposed axial load, the axial velocity at the time of the contact can be estimated.

At the time of the impact, plastic deformation occurs at the interface contact area. After the impact, either the rotor structure rebounds or remains in contact with the static arrangement. The response of the turbine is dependent on the stiffness of the structure, the material characteristic and the conditions of the impact meaning the velocity at the time of the impact.

In the analysis of collision, stiffness of the structure has an essential role in the maps of the wear rate and the friction power. In real engine configuration, the NGVs are clamped at the tips. In the model of the seal segment and the disc interaction, the seal segment is fixed on a side in order to avoid dislocation. It is inevitable that the structure is stiffer than the reality. This has an effect on the response of the structures after the impact and consequently on the wear evolution.

A analysis is carried out aiming to quantify the displacement response of the disc and the vane due to the impact. The result presents that the loads acting on the free turbine due to the impingement of the hot gases are so high that there is not any subsequent bouncing of the free rotor. After the impact occurs, the surfaces of the lock-plate and platform remain in contact.

Figure 6.9 and 6.10 represent the non-dimensional maps of friction power and wear rate with respect to load and rotational speed. These maps are derived from a LSDYNA model which includes a damping coefficient which is responsible for dissipating part of the energy between the structures so that the rebound is prevented. In this manner the response of the structures approximates what happens in reality avoiding subsequent bouncing of the structure due to a stiff response. During impact, the kinetic energy is absorbed in local deformation,

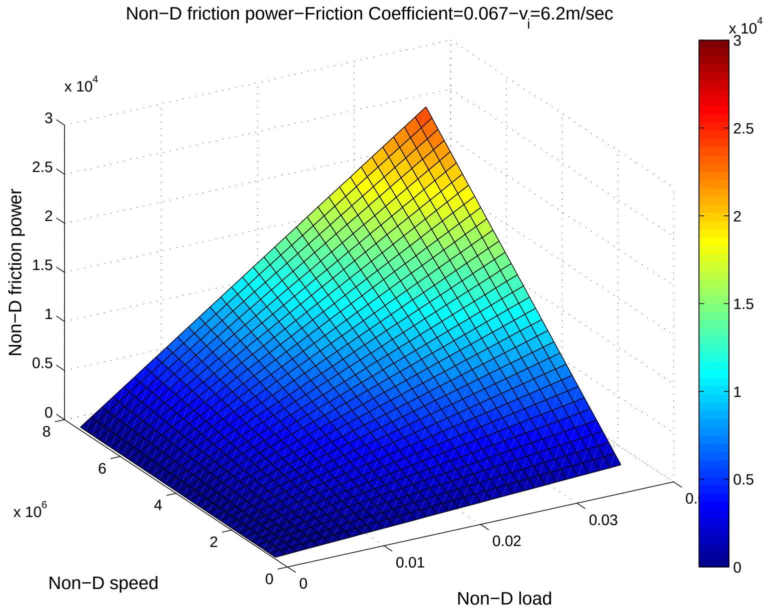

Figure 6.9: Non-dimensional friction power for friction coefficient 0.067-rotational speed 6.28m/sec

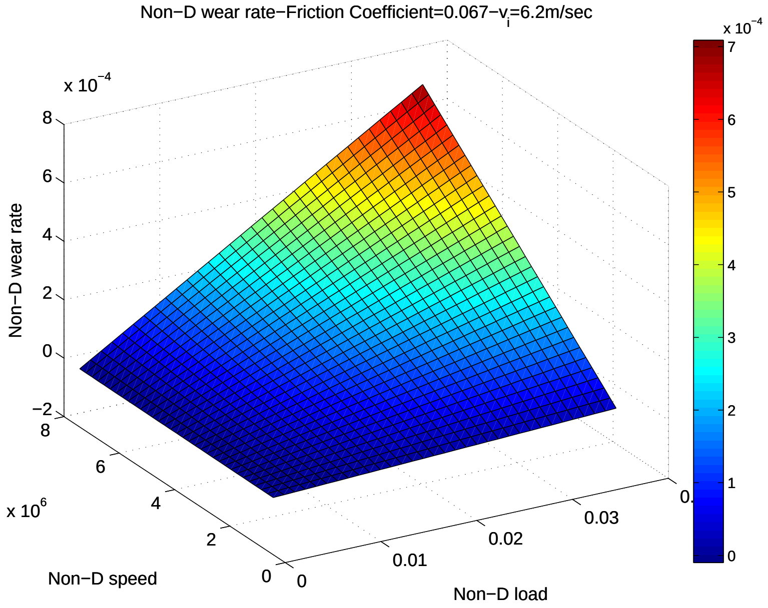

Figure 6.10: Non-dimensional wear rate for friction coefficient 0.067-rotational speed 6.28m/sec

elastic and plastic , of the two colliding bodies. The case of axial velocity equal to 6.28 m/sec has higher kinetic energy, therefore pressure at the contact interface has to be higher.

6.3 Summary

To sum up, this chapter introduces the maps of non-dimensional maps of wear rate and friction power against load and rotational speed. Using the process of linear regression and having a considerable amount of FEA samples, it is possible to provide a wear coefficient which represents the slope of the wear rate-friction power curve.

Furthermore, additional maps have been developed including the effect of the friction coefficient and the inelastic collision on wear rate and friction power. These maps can be implemented in the map database and included in the simulations of the analytical model when it is required by the analysis and the information of the event that need to be captured.

7

Discussion

In the preceding chapter, the development of the non-dimensional maps and the effect of some parameters on them are presented. The current chapter covers the implementation of theses maps to run the analytical model based on the generic methodology. The aim is to predict the occurrence of blade tangling, capture the wear propagation, estimate the rotational speed, torque, friction energy, validate the results against engine data, demonstrate cases that can lead to earlier occurrence of blade to vane interaction.

The motivation for the development of this methodology to capture the impact between turbines is driven by two aspects. From an industrial perspective, it is advantageous to have a generic model which can integrate the database provided from FEA simulations into a analytical tool with structural dynamics equations to address the impact between turbines. The main benefits of a generic methodology comprise the capability to capture the impact event and the wear propagation, the applicability in different engine geometries and failure scenarios, the convenience in use and integration with other codes. Considering the above features of the recommended methodology, it is possible to be used in the preliminary design of the engine.

In addition to the industrial viewpoint, from an academic perspective it is desirable to propose a generic methodology that can predict wear propagation. The generic methodology gives a better representation of the shaft failure event since this methodology is instructive in understanding the fundamental mechanisms of the impact and promising enough to provide adequate information of the conditions and the geometric characteristics that prevent the release of high energy debris.

7.1 Introduction to the applicability of WENSAT

In Chapter 4, the complete methodology of the Wear Estimation Numerical Analysis has been presented. WENSAT is a FORTRAN code which can be used to simulate the transient event of the impact between turbines following shaft failure. The model considers every time step as a quasi-steady condition and estimates the non-dimensional frictional power and the wear rate in every iteration. Numerous LSDYNA simulations of steady input conditions have been carried out in order to develop a grid of data in which the code can interpolate and extrapolate, if necessary to provide the appropriate values of the non-dimensional parameters.

The main inputs include the pressure difference form the gas path analysis. The IP turbine inlet and exit pressure are provided by BD 29 (§4.3). Knowing the pressure difference, the estimation of the load is based on the surface area of the turbine structure. Apart from the load, gas path analysis provides information about the torque of the the turbine after shaft failure. For the purpose of work, available data from two accidental shaft failure events during engine development process are used.

The geometric features of the interacted surfaces are of the essence for the analysis. Hence, a geometry of a real engine is taken into account. FEA analysis of the impact between turbines have shown that the material is failed from the seal segment and the platform while the material failure of the lock-plate can be considered negligible. Therefore, the wear is estimated for the seal segment and platform. Analytical geometric features are depicted in §4.3. The change of contact area and cumulative melted material volume with axial displacement are used as an input in WENSAT. Finally, the database of the non-dimensional wear rate and load maps derived from LSDYNA simulations have been employed and have the capability to capture the range of the load and the rotational speed given from engine data.

This chapter is devoted in investigating the capability of WENSAT to estimate the wear evolution and the occurrence of blade tangling as well as the friction energy, the driving torque and the rotational speed of the free turbine. Due to the absence of considerable amount of database for the case of blade tangling, its effect is not included in the calculation. The attention is focused on the appropriate prediction of the blade tangling occurrence which is presented to be a desirable feature in shaft failure event due to its effect on the rotational seed and the power of the free turbine. The analysis is carried out simulating the following cases:

- Engine A-Base Case
- Engine B-Effect of load
- Friction effect
- Effect of momentum

7.2 Engine A-Base case

The Engine A event is also employed for the assessment of the WENSAT predictions. This event has been extensively used in the parametric analysis in terms of analyzing the results. In addition, it has been used as a basis in the FE analysis and assisted in defining the simulation strategy and the modelling techniques of the LSDYNA model used for the creation of the non-dimensional and wear maps.

7.2.1 Input parameters

For the case of engine A, the axial load acting on the turbine and the applied torque as derived from the engine data are depicted in Fig.7.1. The particular event has been carried out simulated takeoff fuel spiking test. It had suffered a shaft failure on the first fuel spike at maximum power. After shaft failure the engine surged and ran down safely in stall showing no sigh of recovery.

As depicted in Fig.7.1, the load acting on the free turbine has a high value immediately after the event due to the sudden decoupling from the compressor, and it decreases sharply in the first 10% the event time. The curve of applied torque against time follows the same trend.

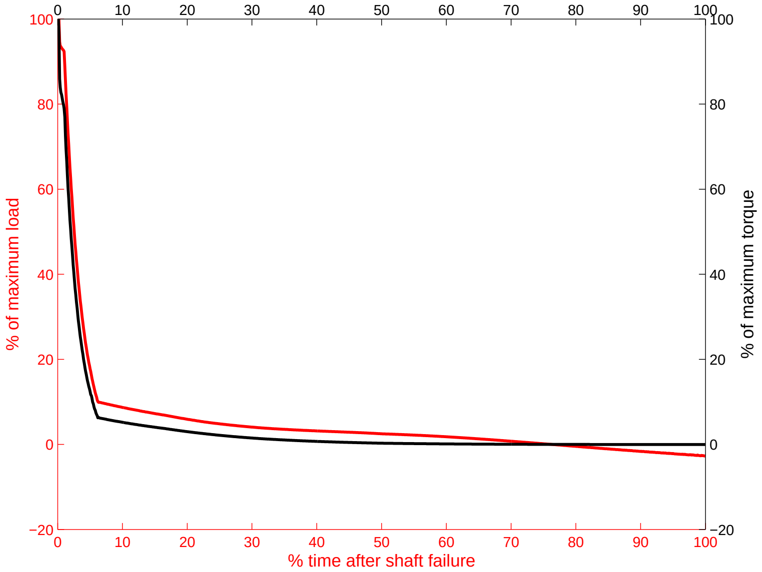

Figure 7.1: % of maximum load and applied torque versus time for the engine A

As aforementioned, a real engine geometric of the seal segment and platform has been provided and its structure is used in order to simulate the interaction between the lock-plate and the static arrangement. The change of contact area and the cumulative melted volume with respect to the axial displacement of the free turbine is depicted in Fig.7.2. The starting point of measuring the axial displacement of the free turbine is the initial location of the lock-plate.

The non-dimensional maps implemented in Engine A scenario are presented in Fig.6.5 and 6.6 and correspond to friction coefficient of 0.067. The assessment of the results need to be carried out with this value since it is the friction coefficient that has been derived from experiments at high temperature interaction of turbines (46). These maps consider as a predominant effect of wear propagation the sliding between the turbines, the effects of the impact is considered to be secondary and have a negligible effect because the system of the structure overwhelms any impact excitation within very short period preventing any rebound of the rotor.

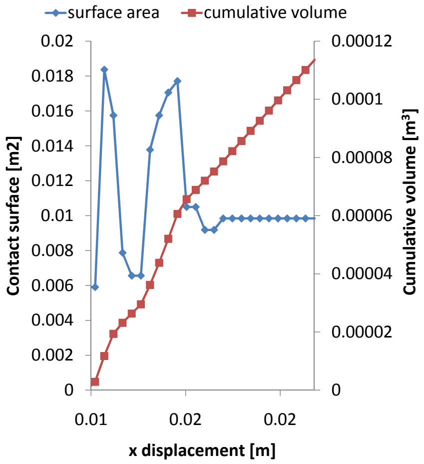

Figure 7.2: Contact area and cumulative volume loss with respect to the axial displacement of the free from the initial location

7.2.2 Estimation of non-dimensional parameters

Using the above inputs, the code calculates initially the non-dimensional parameters of load, rotational speed, friction power and wear rate against time. The normalized value of load derives from the Eq.7.1.

$$F_n = \frac{F}{A \cdot H_o} \tag{7.1}$$

The value of the contact area A is updated in every time step according to the axial displacement of the free rotor. The discretization of the structure into sections of equal volumes assist in estimating easily the contact surface at every axial position. An increase of the contact surface induce a decrease in the normalised load in accordance with Eq.7.1. The contact area is estimated as shown in Eq.7.2.

$$A = \pi \left(r_{out}^2 - r_{in}^2 \right) \tag{7.2}$$

In addition, the non-dimensional rotational speed is calculated according to the Eq.7.3.

$$v_n = \frac{v r_o}{\alpha} \tag{7.3}$$

As shown, the normalized rotational speed is dependent on the radius of the nominal contact area which is derived from Eq.7.4.

$$r_o = \left(\frac{A}{\pi}\right)^{0.5} \tag{7.4}$$

Therefore, an increase in the contact area provokes an increase in rotational speed. The same change in contact area modifies the value of the normalised load in a manner contrary to the one of the rotational speed.

The simulation of the failure event continues with a linear interpolation within the grid of the 3D friction power and wear rate maps and the calculation of friction power and wear rate with respect to the provided normalized values of load and rotational speed for the given time step is accomplished until the termination time.

The results of the analysis in terms of normalized load, rotational speed, friction power and wear rate are presented in Fiq.7.3. It is worth pointing out how the change in contact area affects the results. Regarding the curve of normalised load, there are visible peaks of the curve at 5% of simulation time, due to instantaneous change in contact area. The mass loss, the subsequent axial displacement leads to a change of coantact area affecting the non-dimensional parameters of the load and teh rotational speed. At the beggining of the event, the loading conditions are so intense resulting in a rapid evolution of wear. Therefore, a considerable amount of mass of the seal segment structure melts away allowing the axial displacement of the IP rotor. It is evident in Fig.7.2 that the contact area increases with displacement until a point and then decreases sharply again due to the geometric features of the structure. This steep decrease in the conact area is responsible for the above described instant rise of load and the corresponding drop of rotational speed.

After a particular time, at approximately 15% of event time, the effect of contact area is more obvious on the curve of the rotational speed where the normalised value is suddenly increased. Until 15% of the event time, the impact is localised between the lock-plate and the seal segment. At this specified time, an additional stuctural interaction occurs for the reason that the melting of the seal segment has led to an axial position of the free rotor where the impact between the lock-plate and the platform of the NGVs initialises. This means that the structural interaction is now held between not only the lock-plate and the seal segment but also as between the lock-plate and the platform and the contact area is once again increased with a consequent effect on the normalised roattaional speed.

To conclude, the geometric features of the structure influence the calculation of the normalised load and rotational speed and as a subsequent the calculation of the friction power and wear rate through the maps. It is apparent that normalised parameters and maps achieve the target of the a generic modelling approach independent of geometric characteristics. The most important outcome of this analysis is that the model can capture the changes in contact area and the normalised parameters have the potential to be implemented for the investigation of different engine architectures.

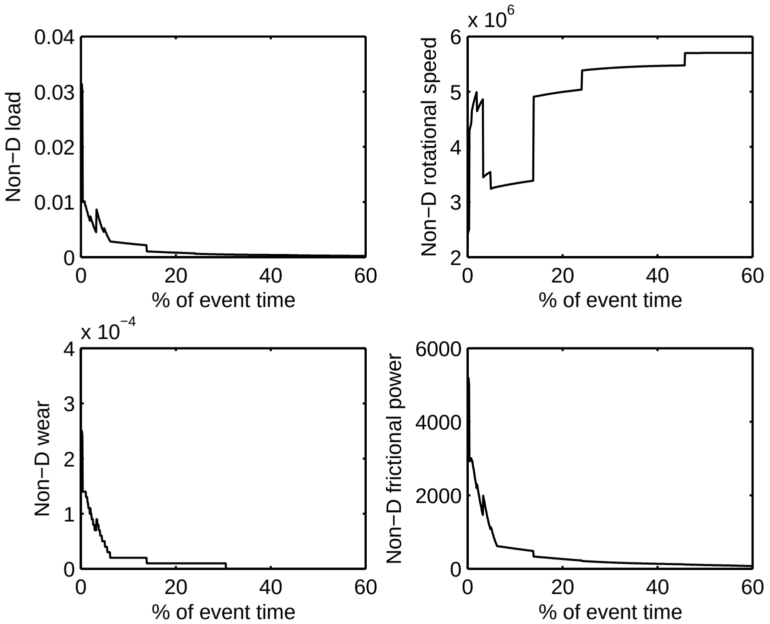

Figure 7.3: Non-dimensional values of load, rotational speed, wear rate and friction power

7.2.3 Comparison with real engine data

This section assesses the results provided by WENSAT with real engine data. The BD29 provides information about the rotational speed and the driving torque following a shaft failure event. The driving torque is estimated through a empirical equation of the friction load acting on the turbine scaled with pressure difference. The driving torque and the rotational speed are derived from Eq.7.5 and Eq.7.6, respectively.

$$T_{driv,j} = T_{applied,j} - T_{fric,j} \tag{7.5}$$

$$u_{j+1} = u_j + \frac{T_{driv,j}}{I} \cdot \Delta t \tag{7.6}$$

Equation 7.5 and 7.6 are employed also in WENSAT but the estimation of friction torque is based on 3D maps of non-D friction power derived from LS-DYNA simulations as presented in Chapter 4.4. In addition to the calculation of the torque and the rotational speed, the privilege of WENSAT is the estimation of the wear propagation and the axial displacement with respect to time.

Figure 7.4 represents the results of rotational speed, friction energy and driving torque of WENSAT and BD29. A good agreement is achieved provided evidence about the capability of the analysis to estimate the response of the free rotor after shaft failure. At the beginning, the rotational speed is highly increased with time due to the imposed driving torque. As the event progresses, the driving torque decreases mainly due to the reduction in applied torque as observed in Fig.7.1. The decrease in driving torque has an apparent effect on the rotational speed, whose derivative with time is minimized.

As discussed, the maps of blade tangling has not been introduced in the analysis because further LSDYNA simulation experiments of constant input conditions need to be carried out to enrich the database required for the development of maps. Therefore, the decrease of the rotational speed due to the blade tangling is not accounted in the analysis.

Figure 7.5 and 7.6 depict the displacement and the wear propagation with respect to time. These two curves are implicative because the displacement is estimated through the mass of the material after the impact. Before the impact,

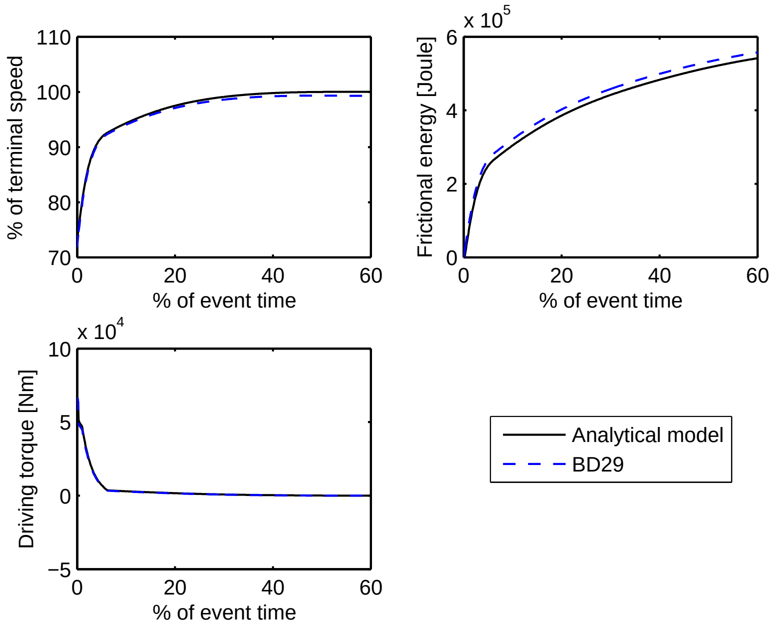

Figure 7.4: Results of rotational speed, friction energy and driving torque and comparison with BD29

the gap between the turbine rotor and stator is calculated with Eq.7.7 and after the impact the cumulative melted mass and volume loss are counted by Eq.7.8 and 7.9. Based on the volume of the melted material, the axial position of the free rotor is evaluated using the condition of Eq.7.11. In Eq.7.7-7.11, the subscript j symbolises the iteration while the subscript i reflects the point of the displacement as derived from the volume discretization.

$$x_{j+1} = x_j + \frac{1}{2} \cdot \frac{F_j}{m} \cdot \Delta t^2 \tag{7.7}$$

$$W_{j+1} = W_j + W_{n,j} \cdot \frac{u_j}{r \cdot \sqrt{\frac{A_j}{\pi}}} \cdot \alpha \cdot A_j \cdot \rho \cdot r \cdot \Delta t \tag{7.8}$$

$$V_{j+1} = \frac{W_{j+1}}{\rho} \tag{7.9}$$

$$V_{j+1} \geq V_{cum,xi} \tag{7.10}$$

$$x_{j+1} = x_{i+1} \tag{7.11}$$

In Fig.7.5 and 7.6, there are observed constant values of wear and displacement in some time periods. This is subject mainly to the discretization of the geometry of the seal segment into volume elements. A particular amount of mass needs to melt away according to the condition described in Eq.7.11 so that a further axial displacement of the free turbine is achieved.

Immediately after the Engine A scenario, the contact of the free rotor with the rear static structure is achieved after 0.3% of the event time as observed in Fig.7.5. When the contact occurs, the transition to a further axial position is dependent on the melted mass. Melting wear starts only if the temperature and the stress distribution on the interface area of the seal segment allows the material to melt away. To achieve this a certain amount of energy needs to be dissipated as heat. This energy limit is estimated through FEA for the particular initial material temperature of 1000K. If this energy limit is overcome, the wear progresses until the rotor is displaced axially at a new position. At every axial position, the same margin of the energy exists in order to have wear propagation. This energy limit is representative of the material, the volume discretization and the initial temperature while its value remains constant at every axial position for the reason that the rate of heat transfer consisting of conduction terms is low enough to allow this assumption. The effect of this energy limit is apparent on both displacement and wear curves where their evolution with time remains constant for time periods.

The slope of the wear curve is sufficiently high at the beginning of the contact due to the existence of high loading conditions at the contact interface. As the event progresses, the intense decrease of load and the moderate rise in rotational speed minimize the wear propagation and the rate of friction energy with time. In this way, the energy limit requires more time to be achieved. This indicates the reason for the increased time period of constant wear after approximately 45% of event time.

According to the wear estimation and the axial displacement, the blade to vane interaction is predicted to occur at 60% of the event time. Furthermore, the predicted time of blade tangling can be assessed by the vibration data of the engine A. The engine vibration data provides an indication of the progression of the events during a failure.

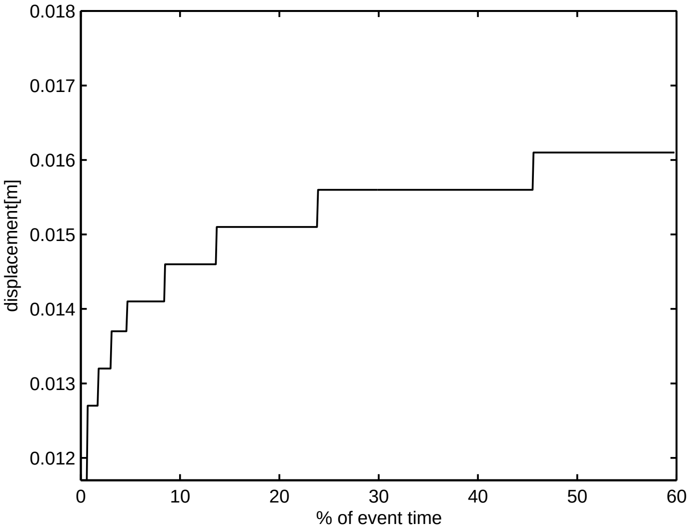

Figure 7.5: Displacement of the free turbine with respect to time after shaft failure

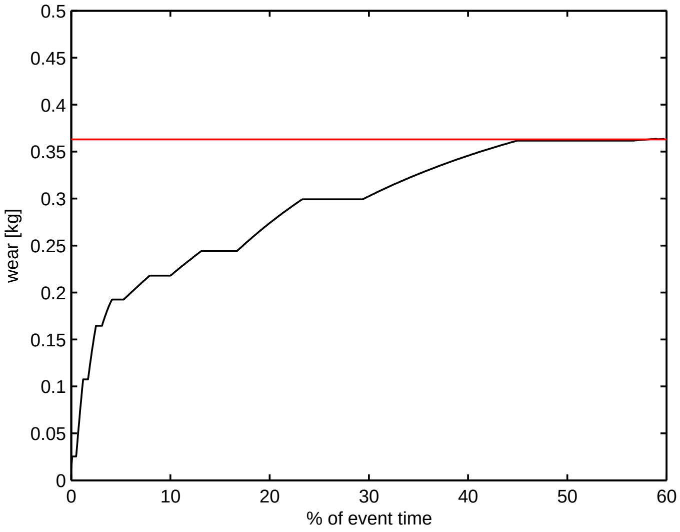

Figure 7.6: Wear propagation with respect to time after shaft failure

In the investigated case, the critical speed (critical speed is the speed at which the natural frequency of bending of the shaft coincides with the rotational speed) of the IPT shaft failure is above the actual speed meaning that the source of large amplitude vibration following shaft failure is an out of balance in the compressor or turbine parts of the system. As it is pointed out in the Fig.7.7 the signal of is dominated by low frequency immediately after the the shaft failure and surge event. As the compressor runs down the vibration amplitude decays. However, a sudden increase in the signal occurred after 65% of the event time. This is the signature of the free IP turbine which makes itself visible due to the unbalanced force imposed by the pattern of blade breakages. Considering that the load decreases sharply after the shaft failure, the load acting on the structure after the first impact denotes that some milliseconds are required in order to attain considerable blade failure due to blade tangling which can contribute to the turbine unbalance.

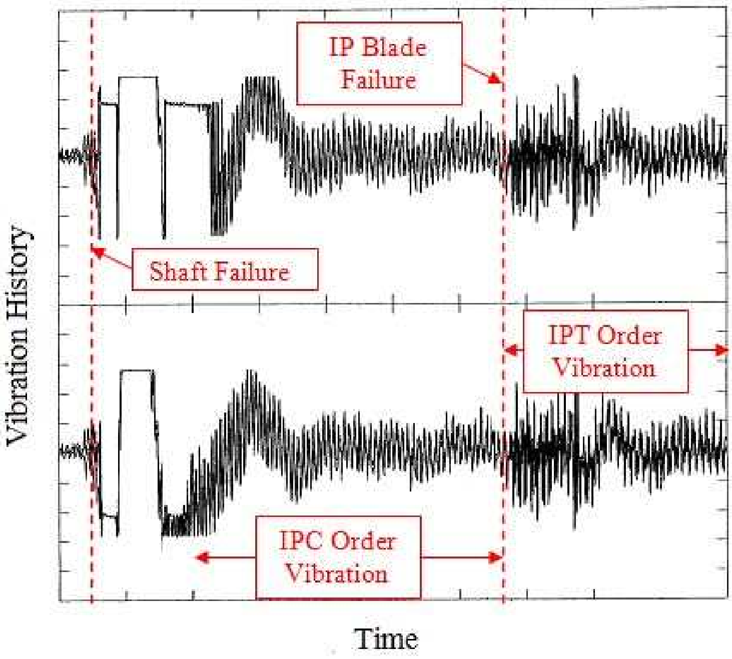

Figure 7.7: Vibration data for engine A

To sum up, good agreement between WENSAT and BD29 is achieved which indicates that the methodology is valid. Furthermore, the assessment of the analytical model with the vibration data increased the confidence on the predictions of WENSAT. The non-dimensional maps derived form LSDYNA simulations have been effectively implemented in the numerical model. The main asset of WENSAT is the capability to provide the wear propagation against time giving information about the axial position of the free rotor and the prediction of blade tangling occurrence.

7.2.4 Discussion

WENSAT enables the first blade to vane interaction to be estimated and the derived results have been assessed with real engine data. In the context of the generic modelling, the non-dimensional maps of friction power and wear rate in respect to normalized load and rotational speed provide satisfactory estimation of the friction energy, rotational speed and wear propagation. The discretization of the structure in finite volumes is capable of capturing the propagation of the wear on the seal segment and the platform of the NGVs and the rearwards movement of the free rotor.

Having Engine A scenario validated against engine data, it is possible to assess the effect of important parameters like load, friction coefficient, geometric features and collision in the evolution of wear propagation and the prediction of the first blade to vane interaction. Furthermore, the applicability of this tool in other engine scenarios is presented.

7.3 Engine B-Effect of load

This part is devoted in understanding how different input parameters of load and applied torque can induce different response of the free turbine influencing the wear propagation.

7.3.1 Input parameters

Fig.7.8 depicts the load as derived from the pressure difference in the main gas path and the applied torque on the free turbine. In this failure event, there is less vibration than the engine A scenario provoking the HP compressor to recover from surge and run until the engine surges again. The non-dimensional maps implemented are the same with the Engine A scenario.

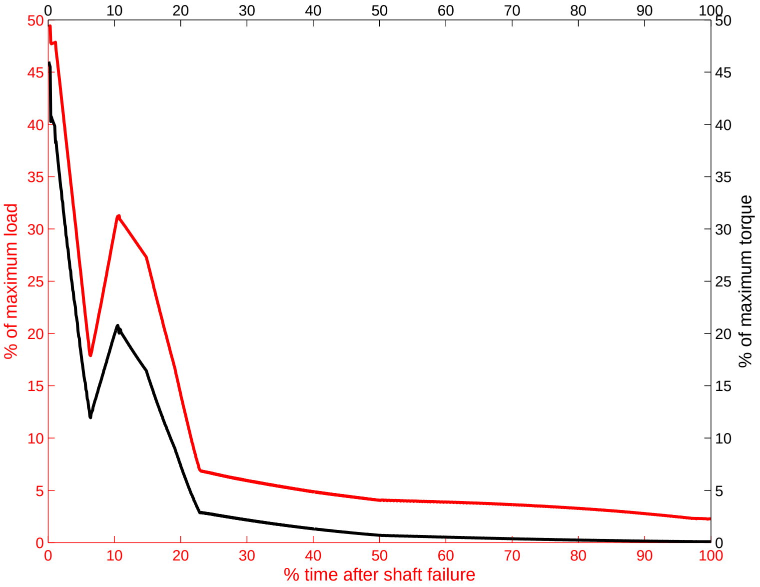

Figure 7.8: % of maximum load and applied torque versus time for the engine B

The curves of load and torque in Fig.7.8 are plotted in a percentage of the maximum load and torque attained in engine A. It is obvious that the free rotor of engine B has lower axial load and torque than the one of engine A scenario. The load is 50% less and it follows a downward trend until the first 5% of the event time. Afterwards, the second surge of the engine causes a rise in load which is then rapidly decreased to 5% of the maximual load of engine A in 20% of the event time.

Comparing the two engine scenarios, A and B, the trend of the load and torque of the engine B scenario differs from the engine A. In engine A, the load drops to the 5% of the maximul load within 10% of the event time without any sign of recovery. Although, in engine A scenario the applied load and torque attain higher values than B scenario, the occurrence of the second surge in the latter is expected to increase instantly the melted mass of the seal segment. It is of the essence to quantify the effect of the load and the torque in the wear propagation of the results.

7.3.2 Estimation of non-dimensional parameters

The diagrams of the non-dimensional parameters are represented in Fig.7.9. The impact leads to a high non-dimensional wear rate at the beginning, which drops up to a minimum value followed by an increases due to the recovery from the first surge of the engine. The same trend is also accompanied by the friction power.

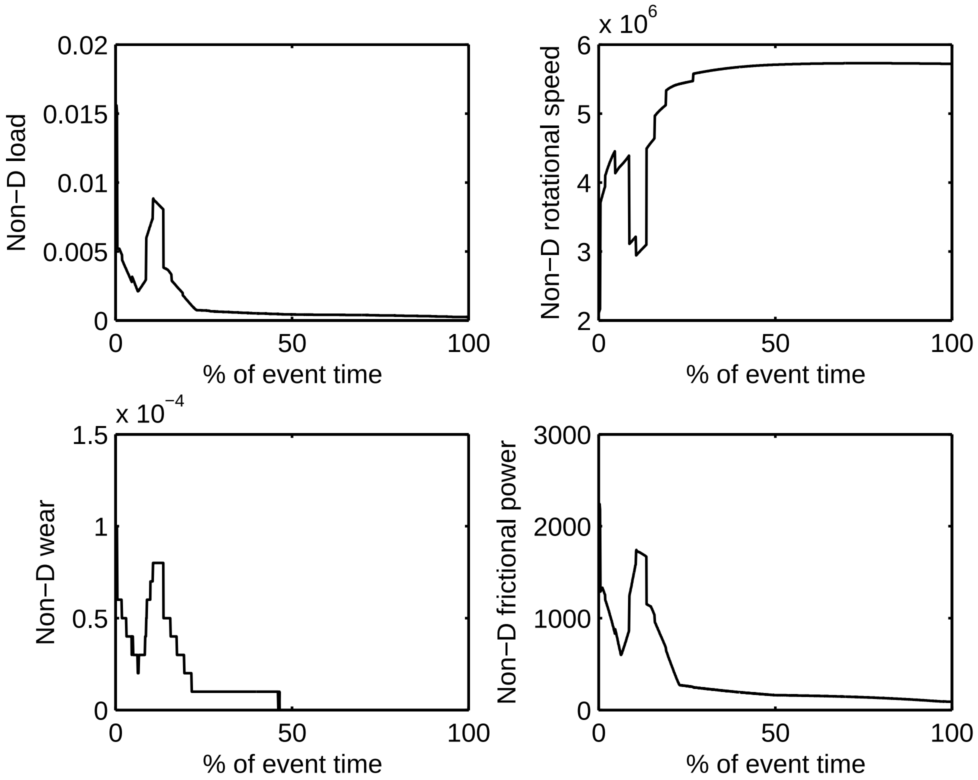

Figure 7.9: Non-dimensional values of load, rotational speed, wear rate and friction power

Comparison between the non-dimensional parameters of the engine scenario A and B lead to the following observations:

- The lower axial load acting immediately after the shaft failure event leads on the rotor of Engine B results in lower values of non-d wear rate and friction power and simultaneously higher rotational speed
- The non-D wear and friction power decreases against time in engine A scenario, however in the case of engine B the recovery provoke a rise in these values and a subsequent drop in rotational speed for the same time period. After the second surge, the load attains higher values than engine A scenario implying that the wear rate and the friction power are also increased.
- Instant peaks of Non-D load are derived in both cases as a consequence of the contact area change.

7.3.3 Comparison with real engine data

The analysis of engine B is performed for two reasons; firstly, to quantify the effect of different loading conditions on the evolution of the event and secondly, to evaluate the results with real engine data and understand the effect of the secondary air system dynamics on wear propagation and axial displacement of the free rotor. Figure 7.10 represents the comparison between the WENSAT results and the BD29. It can be observed that good agreement is achieved regarding rotational speed, friction energy and driving torque.

At first, a comparison between failure scenario of engine A and B gives a better view of the impacts and the effect of load on the progression of the events. In the scenario of engine A, it has been noticed an intense progression of wear from the beginning of the impact until the 10% of the event time. During this period of time, the load is high enough to preserve high friction power and after this period the gradient of wear decreases. From 10% until the occurence of blade interaction, the value of the load is approxiamately at the 95% of the maximum load and the wear propagation retards as observed in Fig.7.11.

The wear against time of the engine B follows a different pattern from Engine A scenario. The load acting on the turbine is lower by the order of 50% of the maximum load of engine A, therefore the wear propagation is not so severe immediately after the shaft failure. The second surge and, as a consequence, the increase of the loads applied on the free rotor, accelerate the progression of melting wear mechanism. The energy dissipated between the structures manages to heat the contact surface of the seal segment and platform quicker leading to blade tangling at about 20% of the simulation time.

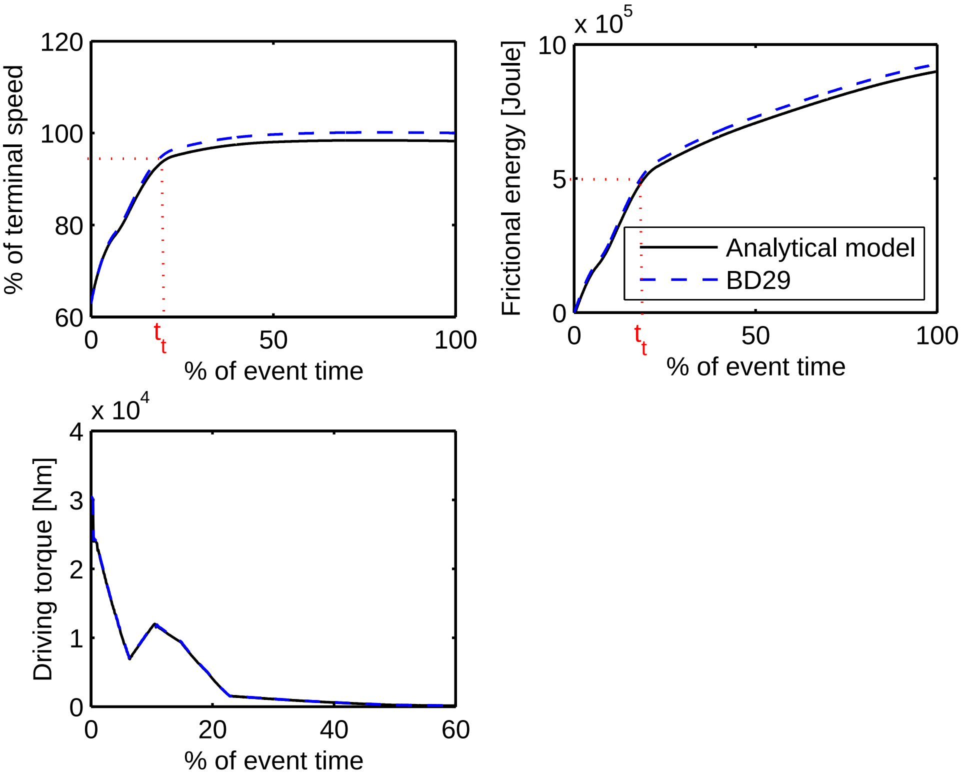

Figure 7.10: Results of rotational speed, friction energy and driving torque and comparison with BD29

The load applied on the free turbine in the particular simulation is derived directly from the main gas path without regard for the air system dynamic behaviour. According to engine data reported in (2), the LPT cavity is sealed due to the absence of the residual vibration which are apparent in the case of engine A allowing leakage between the cavity and the gas path downstream for the IP turbine disc. In case of engine B, the cavity pressure acts as a pressure in the forward direction resulting in lower average axial load on the free turbine whereas the blade failure occurs close to the end of the event at (100% of event time).

Considering only the applied load of the main gas, it would lead to a premature blade tangling occurrence as observed in Fig.7.11 and Fig.7.12. When blade tangling happens in this case, the rotational speed of the free turbine is lower and therefore the free turbine has attained less energy. After the occurrence of blade tangling, the power of the free turbine is further reduced due to the additional frictional power derived from blade to vane interaction. Furthermore, the analysis performed accounting only for the main gas path load shows that for the engine B the cavity pressure plays a significant role in the wear propagation contrary to engine A. In the engine B, the LPT cavity remains sealed from the rearward movement of the IPT disc, which means the axial load applied on the rotor is lower, limiting the frictional wear rate of the rear static structure. In this way, the wear progresses slower allowing blade tangling to occur later on.

In addition to vibration engine data and BD29, the terminal speed of the free turbine can be used as a validation process in order to evaluate the validity of the occurrence of blade tangling. The disc bore growth of engine B scenario (2) indicates a terminal speed 5% higher than the one predicted demonstrating that the secondary air system dynamics has an effect on the axial load and as a consequence the wear rate, the axial displacement and the prediction of the terminal speed.

The overestimation of the wear rate and the under-prediction of the terminal speed in engine B scenario are a consequence of not accounting in the axial load the cavity pressure. The integration of WENSAT in the SAS model developed for the purposes of shaft failure events can lead to an accurate estimation of the wear propagation and terminal speed. Therefore, engine B cannot be used for validation purposes. However, the engine B scenario contributed in the understanding of the critical role of the cavity pressure in wear propagation. An integration of WENSAT and Secondary Air System (SAS) model will contribute a lot in the analysis of shaft failure event and provide the capability to simulate events with both sealed and unsealed cavity.

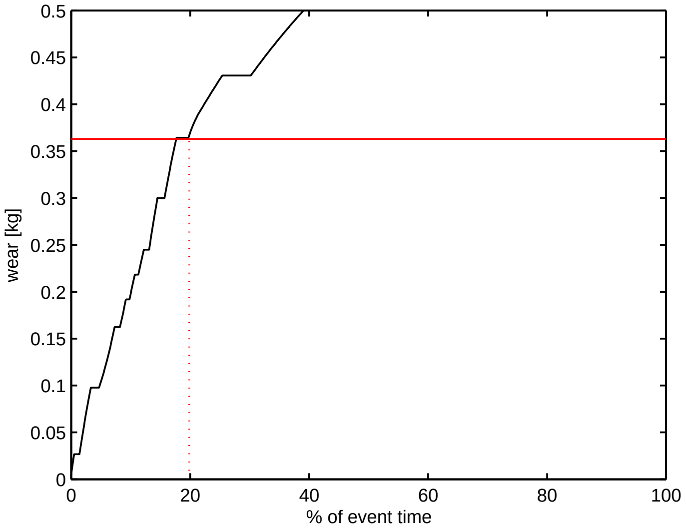

Figure 7.11: Wear propagation with respect to time after shaft failure

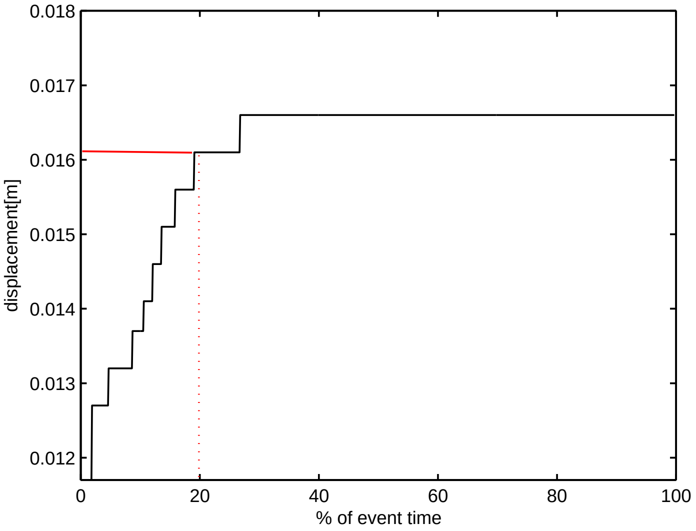

Figure 7.12: Displacement of the free turbine with respect to time after shaft failure

7.3.4 Discussion

The response of the non-dimensional parameters with time is presented showing the effect of the surge in wear rate and friction power. The results of rotational speed, driving torque, frictional energy and wear propagation are compared with engine data and the importance of secondary air system is reported with correspondence to the wear propagation.

The analysis performed highlights the importance of the secondary air dynamics system in the propagating of the shaft failure. According to (2), non including the cavity pressure can lead to an overestimation of the amount of friction by about one third. This explains why the terminal speed is predicted 5% lower than the data derived from the bore growth. This issue can be overcome by intergrating the wear estimation numerical analysis into the SAS (secondary air system dynamics code) and accounting for the cavity pressure.

7.4 Friction effect

Friction coefficient is one of the factors that has a significant effect on the estimation of the friction energy dissipated between the sliding surfaces. According to previous research reported in the public domain (47), the friction coefficient is not stationary and depends on time even for stationary experimental conditions. The friction coefficient varies with respect to the relative velocity between the sliding interface contact. In Fig.7.13 it is observed that the identified friction coefficient has a negative slope with respect to the relative velocity. From a theoretical point of view, it is dependent on the the load, kinematics, material and geometry parameters of the contact bodies.

The effect of the friction coefficient on the contact interface can be investigated in order to have a quantitative analysis of how a small change on the value can increase the friction power and accelerate wear. LSDYNA calculation have been run for a different friction coefficient within the limits imposed by the material type and the sliding conditions. For instance, the friction coefficient of nickel alloys rubbing under dry conditions and low velocity is equal to 0.2 while there is a exponential reduction with respect to the sliding speed. For the case of engine

A and B scenarios, the load, the rotational speed and the initial temperatures on the structures are high enough to conclude that there is melting wear and the friction coefficient is close to the minimum value of 0.067. However, the demand of developing a more generic tool that can give results for different friction coefficient and quantify the effect of its value on the evolution of the event triggered the investigation of friction coefficient 0.1.

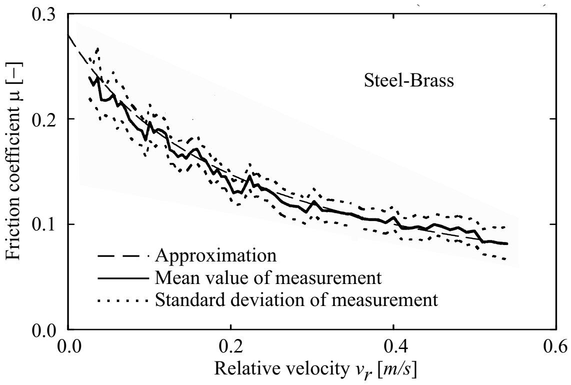

Figure 7.13: Friction coefficient versus relative velocity

7.4.1 Input parameters

In the event of shaft failure, the sliding velocity between the two turbines is very high resulting in melting wear. Since this occurs the expected friction coefficient is very low. Although, the base case simulation showed good estimation of the blade tangling occurrence regarding the vibration data, the effect of the friction coefficient on the evolution of the event needs to be reported in the present section aiming to provide information of the wear progression under higher friction coefficient of 0.1.

To investigate the effect of frictional coefficient, different maps developed through new LSDYNA simulations have been imported in WENSAT. The maps correspond to friction coefficient 0.1 and are presented in Chapter 6. The load and the torque applied on the free turbine are the same with the engine A scenario which has been validated with engine data and provided good agreement.

7.4.2 Comparison with engine A-base case

Figure 7.14 illustrates the non-dimensional parameters for friction coefficient 0.1 as well as the results of the base case. These plots can demonstrate how the values of the normalised load and rotational speed alter as the event progresses. The friction power and the wear rate have higher values accelerating the wear propagation. The result of this is depicted in the curves of normalised load and rotational speed. The sharp increase of wear rate encountered within the first 10% of the event time affect the cumulative melting mass. The corresponding peak of the normalised load demonstrates that the melted mass leads to the transition to the smaller contact area zone, where the seal segment has smaller thickness and the platform is not included in the contact yet.

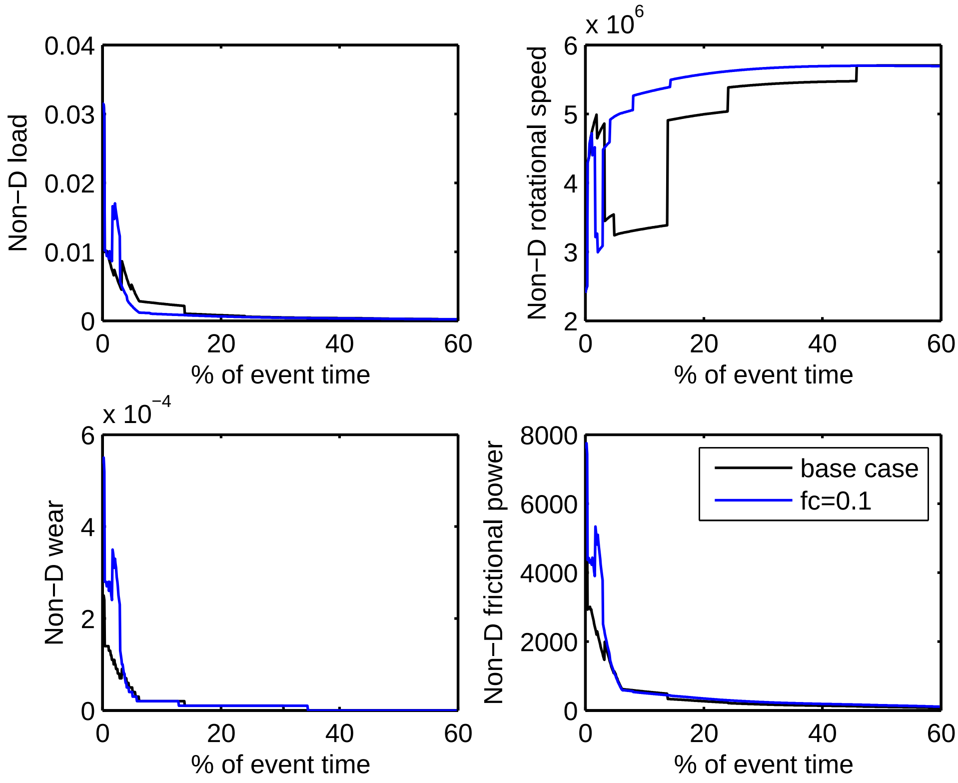

Figure 7.14: Non-dimensional values of load, rotational speed, wear rate and friction power

In view of higher friction coefficient, the transition is more intense leading to higher peak in the normalized value of load and thereafter is stabilized to a value close to the base case (Engine A scenario). Furthermore, the change of contact area is apparent in normalized rotational speed which decreases in less time and then reacquires values above 4.5e+6 after 5% of the event time. As it can be seen, the wear rate achieves very high values, in particular, at the beginning of the event, while the value is stabilized at an almost constant rate after 5% of the event time. This is also represented in terms of frictional power, due to the dependency of wear rate on the friction power.

Figure 7.15 represents the mass of the material which melts away after the crash. Mass changes rapidly with respect to the time. The mass limit of blade tangling occurrence is attained after 12% of the event time. Comparison between the base case of friction coefficient 0.067 and the case of 0.1, indicates that the minimum wear value for the occurence of blade tangling is 80% earlier. Considering that the friction coefficient increase is of the magnitude of 33 % it is obvious that it has a critical role in the propagation of the event and the estimation of blade tangling occurence.

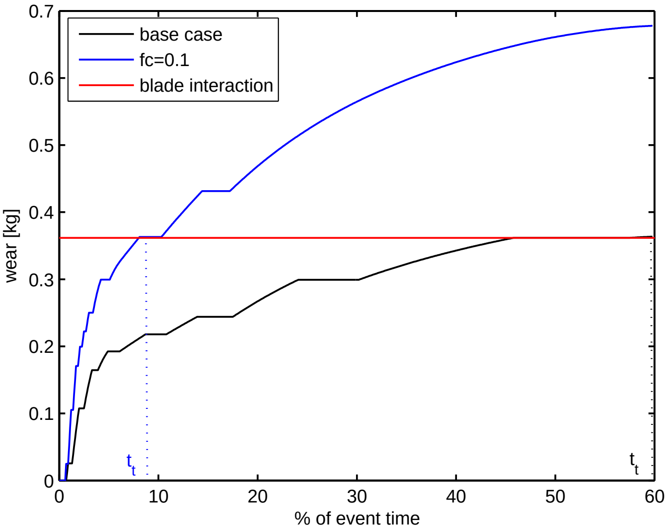

Figure 7.15: Wear propagation with respect to time after shaft failure

7.4.3 Discussion

The melting mass make allowance for the imminent downstream displacement of the free turbine. The main requirement after shaft failure is to limit the power of the free turbine as quickly as possible to an acceptable value. With higher frictional coefficient between the sliding surfaces, the frictional power is increased accelerating the wear so that blade tangling is achieved earlier. In the manner, the blade tangling takes place under lower rotational speed (approximately 7% lower than the engine A scenario) as observed in Fig.7.16

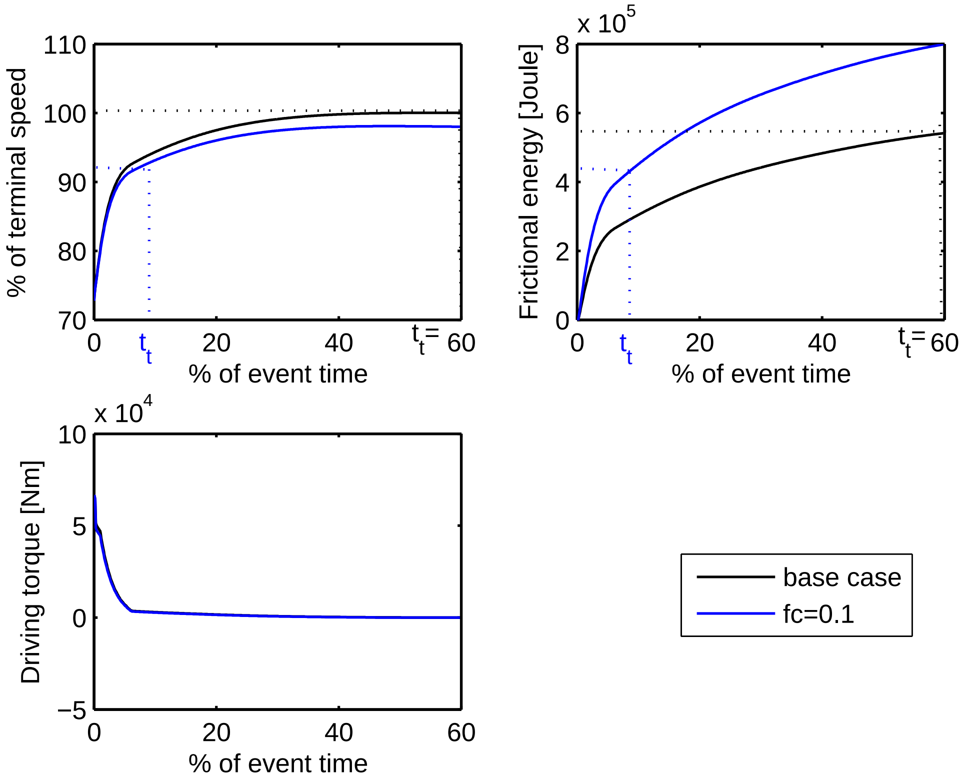

Figure 7.16: Results of rotational speed, friction energy and driving torque

To conclude, the friction coefficient has a considerable effect on the results. As aforementioned, it is dependent on the rotational speed and the material type. The friction coefficient between nickel and nickel alloy is lower than the friction coefficient between nickel and steel. Therefore, the sliding between different materials may result in accelerating the occurrence of blade tangling limiting the power of the free turbine earlier. An additional advantage involves the blade tangling under lower rotational speed. This would be a beneficial design characteristics since blade fragments will attain lower kinetic energy at the the time of the impact with the containment.

7.5 Geometric effect

With the evaluation of the numerical model predictions of engine A failure scenario against BD29 and vibration data from experiments and showing showing reasonably good agreement, the model is used to explore the affect of variable geometric characteristics.

The critical parameter in rubbing surfaces is the contact area, which is affected by the radius of the seal segment and the thickness of the structure. In order to understand how the structure changes two schematics of :

1. 5% decrease in radius
2. 10% decrease in seal segment and platform thickness

7.5.1 Input parameters

Engine A is used as a basis to accomplish the effect of the geometric characteristics on the behaviour of the free turbine. In the scenarios with modified geometric characteristics, the applied load and toque are identical to the engine A. In this manner, the results can be evaluated and a picture of the geometric effects on the behaviour of the free turbine can be given.

Figure 7.17 and 7.18 represent the change of the cumulative volume and the contact surface with respect to the axial displacement, respectively. It is obvious that for the same displacement the volume that need to melt away for the modified structures is less than the real geometry. Furthermore, the interface contact area changes with axial displacement due to the decrease in thickness and mean radius of the seal segment and platform.

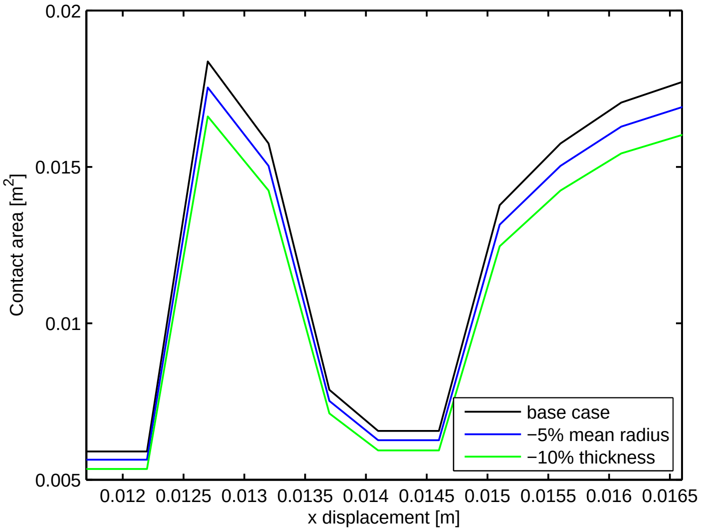

Figure 7.17: Contact area with respect to the axial displacement

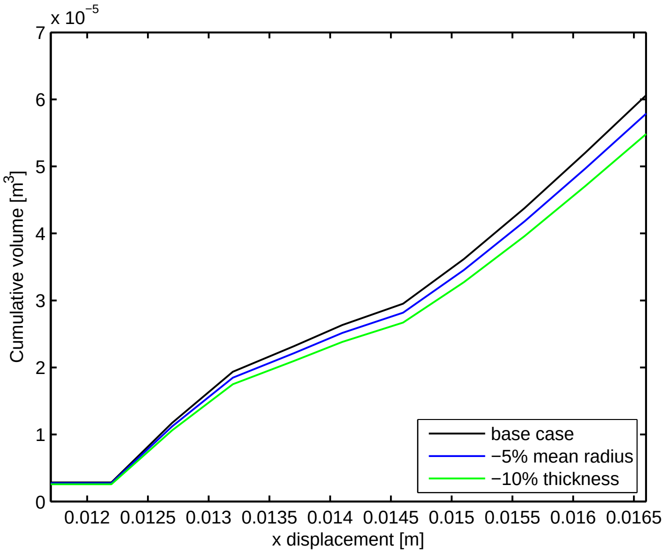

Figure 7.18: Cumulative volume melted away with respect to the axial displacement

7.5.2 Comparison with engine A-base case

The generic methodology has the potential to represent possible turbine architectures which enables fast transition to blade interaction affecting in this way the power of the free turbine. The estimation of the non-dimensional parameters are represented in Fig.7.19, while the evolution of wear propagation and the results of rotational speed, friction energy and torque is depicted in Fig.7.20 and Fig.7.21, respectively.

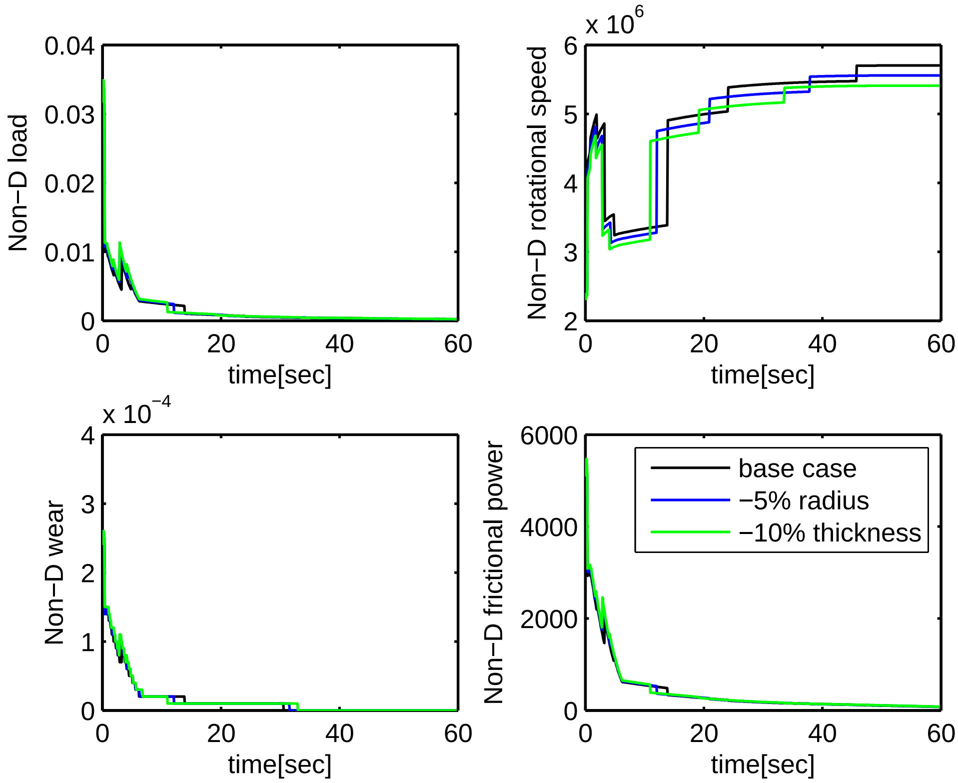

Figure 7.19: Friction coefficient versus relative velocity

It can be noted that even small modifications in the contact area can be beneficial for the shaft failure event in terms of earlier blade tangling. It is worth to point out the non-dimensional value of load is slightly higher for both geometric features while the rotational speed is also affected in an inverse way.

The next step is to reconsider if the small changes in terms of friction power and wear rate have an effect on the wear propagation and the frictional energy,

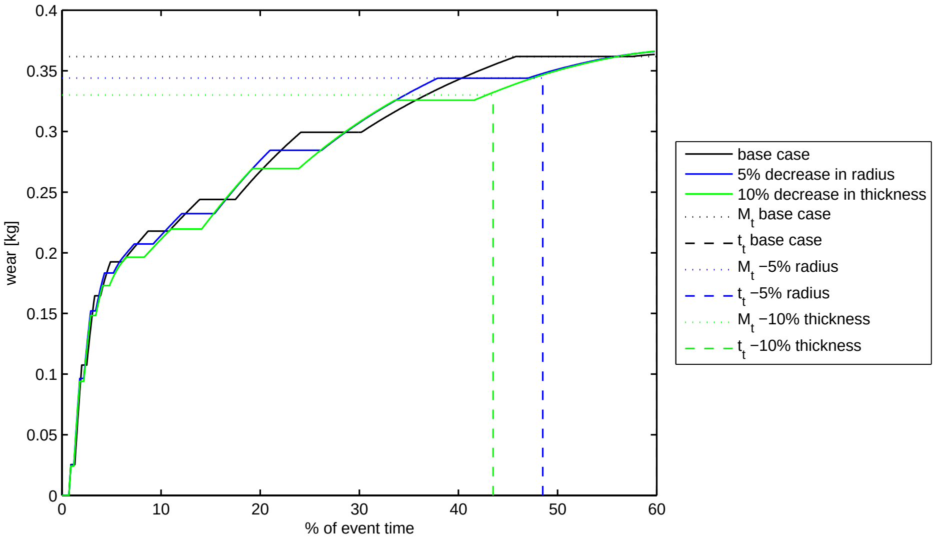

Figure 7.20: Wear propagation with respect to time after shaft failure

Cases	% Volume degradation	% Tangling time diminished
-5% radius	5%	20%
-10% thickness	10%	38%

Table 7.1: Geometric effects on cumulative melted volume and blade tangling

respectively. The prediction of wear propagation is shown in Fig.7.20. As mentioned, a decrease in the radius and the thickness of the seal segment and platform results in diminishing the volume loss that needs to melt away to have blade interaction. Table 7.1 represents in percentage the effect of the reduction in radius and thickness on the requirement of volume loss and the occurrence of blade tangling. As noticed, the blade interaction makes its appearance earlier. Considering these cases, it is highlighted the possibility of accelerating the blade interaction by imposing different contact area in terms of mean radius or thickness.

From the perspective of engine design, these modifications in turbine structure can prove to be favorable in the shaft failure event. Considering that earlier occurrence of blade tangling necessitates the higher friction power with a corresponding decrease in driving torque as observed in Fig.7.21. Additional advantage involves the reduction of the rotational speed when blade interaction is established. This is a positive aspect mainly because the blade fragments are ejected with lower rotational speed.

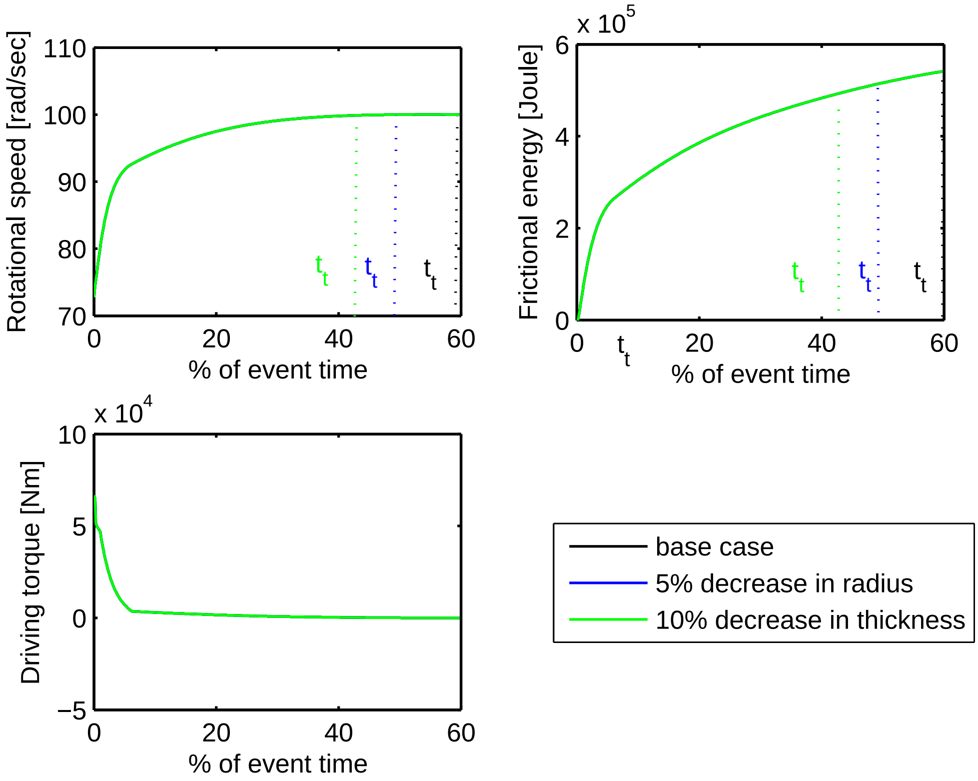

Figure 7.21: Results of rotational speed, friction energy and driving torque

7.6 Effect of momentum

7.6.1 Input parameters

This section aims to represent the effect of collision in the behaviour of the turbines in contact and as a result in wear propagation. Parametric studies showed that the bouncing of the free turbine accelerates the wear propagation. In this context, accounting for the axial movement of the turbine forward after the impact and the energy that is stored in the structures due to the conversion of the kinetic energy into internal energy of the material.

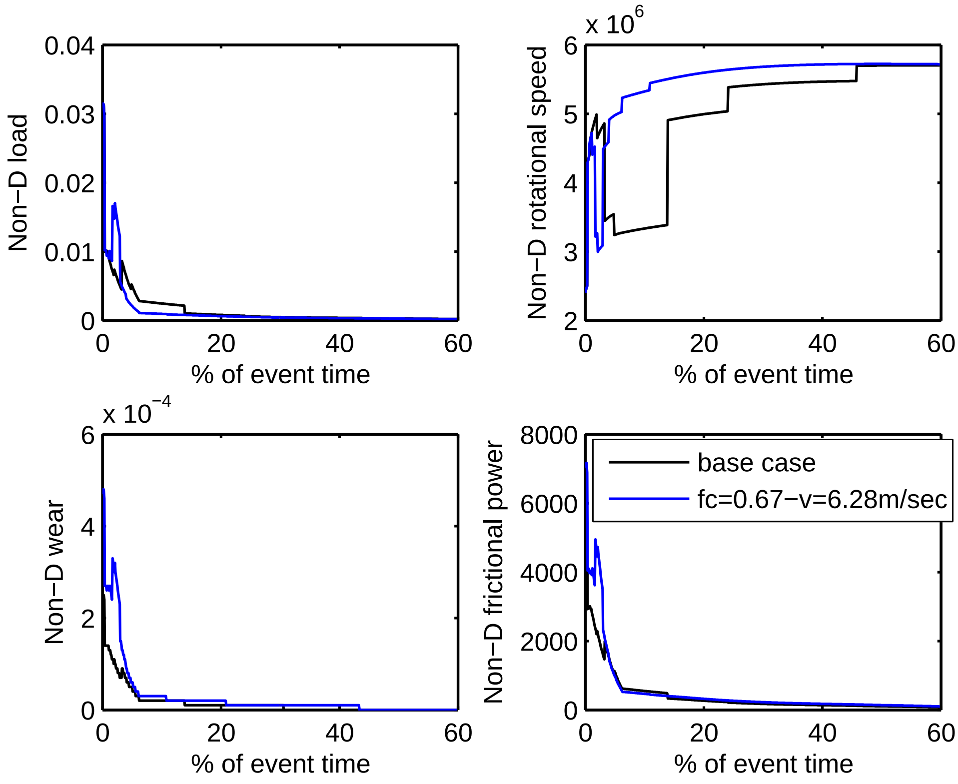

Figure 7.22: Non-dimensional values of load, rotational speed, wear rate and friction power

The maps of friction power and wear rate are derived taking into account LS-DYNA simulations in which there is axial velocity of 6.28 m/sec and a damping coefficient to avoid oscillation because of structural stiffness, as presented analytical in §3.2. The velocity of 6.28m/sec is derived from the axial velocity applied on the structure and the particular gap between the IP turbine and the following static arrangement.

The applied load and torque correspond to the engine A scenario. The results obtained from this analysis are compared to the base case in order to show how the momentum and the collision between the bodies can affect the wear estimation and the time of blade tangling occurrence.

7.6.2 Comparison with Engine A

Apart from the slide between the structures, which is the predominant mechanism of wear propagation, another aspect is the impulse between the structures before a force balance is achieved and the surfaces remain in contact. The model has the potential to be improved and account in a more accurate way the transition to a state of equilibrium. The integration of the generic model into a multidisciplinary can be beneficial for the understanding of collision between the bodies and the effect of momentum.

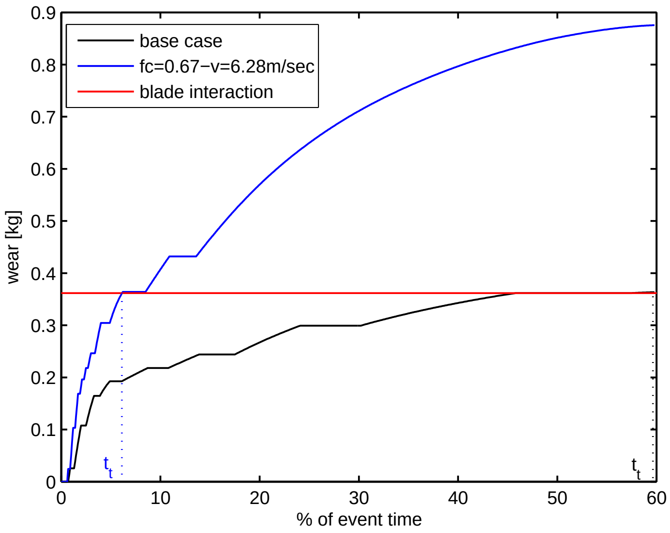

Figure 7.23: Wear propagation with respect to time after shaft failure

At the time of the first impact, the free turbine has a high kinetic energy from the axial velocity and the rotational speed imposed and therefore momentum. This implies that part of the kinetic energy is converted into internal energy of the colliding bodies. This comes in contrast to the base cased in which the axial velocity is considered to be moderate and hence it is assumed that the two bodies remain collided and the momentum of the free turbine has a negligible role in the wear mechanism. In case of an imposed axial velocity which could facilitate a rebound of the free turbine and a fast transition to a state of force equilibrium, a subsequence of inelastic collisions occurs increasing the pressure distribution on the contact interface. In this event, the deformation of the material increases and the failure criterion is reached earlier provoking higher mass failure as observed in Fig. 7.23.

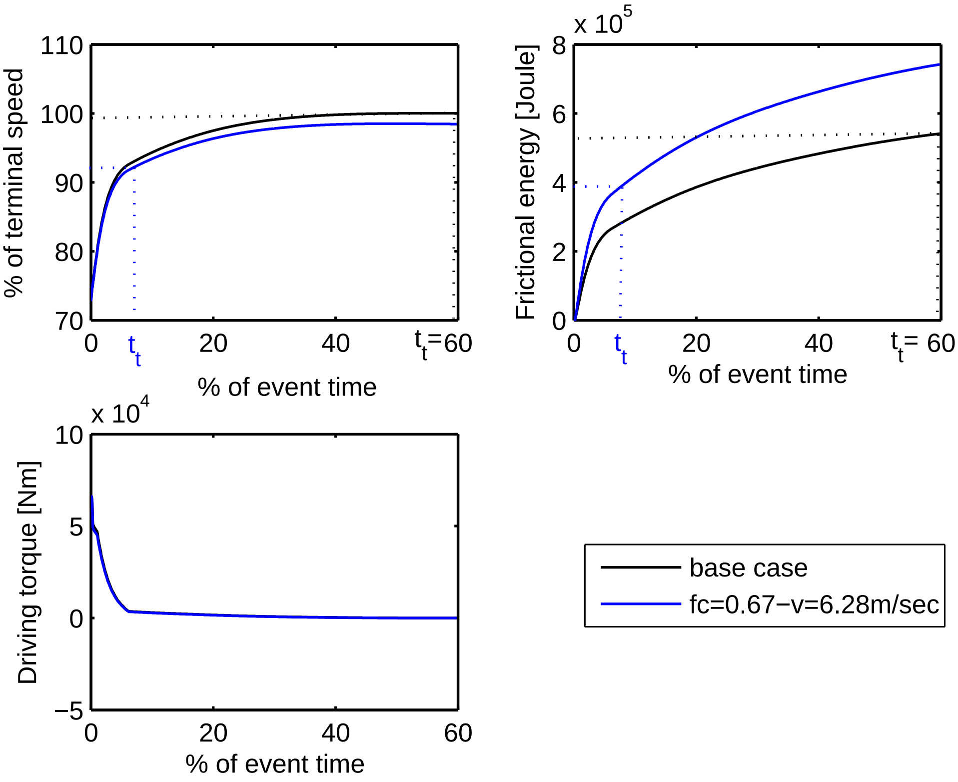

Figure 7.24: Friction coefficient versus relative velocity

It is evident in Fig. 7.24 that the momentum of the free rotor at the time of the impact causes higher wear rate and friction power. This is apparent especially during a period of 5% of the time of the event when the applied load gains excessive values. This behaviour is reflected also in the evolution of wear against time in Fig. 7.23. The momentum of the free rotor facilitates the quick melting of the mass of the seal segment and platform provoking blade tangling occurence within 5% of the event time. This implies that the power of the free turbine is affected quicker due to blade tangling. The occurence of blade tangling is achieved when the rotational speed apporaches 90% of the terminal speed of the base case. The power of the turbine will be limited within acceptable values in less time and the fragment of the turbine blades as a result of the blade tangling will obtain lower kinetic energy preventing the release of high energy debris due to uncontacined failure.

7.6.3 Discussion

The momentum of the free turbine can facilitate the wear propagation and the blade tangling occurrence. The high kinetic energy of the turbine is converted into internal energy of the structures increasing the temperature and the stresses on the interface surface. When the velocity of the free turbine at the time of the impact is high, mass loss is precipitated leading to blade tangling. Therefore, the existence of high amplitude vibration of the structure can accommodate the safety of the event avoiding high debris release.

7.7 Summary

This section has presented the applicability of the methodology on real engine scenarios. Based on real engine data of two accidental scenarios, the applicability of the methodology has been shown.

In the first scenario, Engine A, the WENSAT was capable to capture the dynamic of the event accurately. The results of the simulation have been assessed with available real engine data, based on turbine vibration and growth of the disc bore and shown good agreement. This engine gave confidence about the applicability of the methodology and its capability to capture the impact between turbines. Generally speaking, the tool has been verified through validation with real engine data.

Furthermore, this tool facilitates the study of the effect of geometric configuration, friction coefficient and collision on the progress of the event. Engine A scenario has been used as a base case for quantifying the influence of geometric features and boundary conditions on wear propagation blade tangling occurrence.

In the scenario of engine B, the simulation results provided evidence of blade tangling earlier than real engine data. In the particular engine scenario, the pressure in the LPT cavity is sufficient and is a basic requirement to be taken into account to avoid overestimation of the wear. The gap between the structures is sealed due to absence of residual vibrations therefore the pressure in the cavity need to be included in the calculations because it affects the axial load acting on the free rotor. If the estimation of axial load is included the pressure cavity, its value would have been lower decelerating the mass loss and as a consequence blade tangling occurrence.

WENSAT is a code which is based on structural dynamic equations and the maps derived from a thermo-structural analysis using a nonlinear explicit finite element solver. Generally speaking, this tool has been developed in order to be effectively integrated with tools which simulate the aero-thermodynamic phenomena occurring into the gas turbine engine for the prediction of shaft failure event.

8

Conclusions

A FE numerical modelling of the impact between turbines after shaft failure and an extensive quantitative study of the parameters affecting this impact has been conducted. A modelling methodology is developed in the view of optimizing computational resources. Extensive parametric studies on the mechanical modelling of turbines' impact have emphasized the importance of carrying out thermo-mechanical analysis.

The simulation strategy using LSDYNA solver have been, thereafter, used in developing a generic modelling approach. The generic modelling approach is able to simulate transient events of turbines' impact following a shaft failure event. The key findings from each chapter are summarised in the following sections.

8.1 Simulation strategy

Turbines in contact is a complex problem to analyse. An insight into the prevailing phenomena of the impact can be achieved through the FE analysis. Non linear finite element analysis solver, LSDYNA, has the potential to capture the impact between the structures and facilitates the estimation of the heat dissipated as friction between the structures, the increase of temperature on the contact interface and the material failure.

The main outcome of the simulation strategy are summarized:

- The geometry of turbines in contact is divided into two key areas: the interaction between lock-plate and seal segment /platform and the blade to vane interaction

- The recommended simulation strategy manage to offset the computational penalty

- The simulation strategy assisted in defining a generic methodology

8.2 Parametric studies of mechanical models

- An analytical presentation of the boundary conditions and the modelling features have been provided. Generally speaking, the parametric studies provided a better insight into the understanding of the impact, gave confidence about the applicability of FEA solver in simulating severe impacts between turbines where temperature has a significant role.

- The attention has been focused in the modelling techniques that need to be adopted in cases of severe impact between metals. Challenges arose during the development of the methodology. A significant challenge is the avoidance of zero energy modes called hourglass. Existence of high hourglass energy can lead to misleading results in terms of energy. Hourglass energy means that a element can be deformed without dissipating any energy therefore the structure responds as it has no or little stiffness. LSDYNA has various algorithms for inhibiting hourglass modes.

- Damping effect is linked to the stiffness of the structure. Excessive loads applied on the system of structures has as a result the rebound of the structure and the system gains an equilibrium after few milliseconds. LSDYNA has the capability to damp the continuous bouncing by means of applying a damping coefficient on the static structure to consume part of the energy in order to behave as the real structure of the NGVs with clamped vanes at the tip. This is also one of the advantages of the code which assist in the proposed simulation strategy where the structure of the turbines are divided into two key areas. The commands of the LSDYNA software facilitate this division and the user has the flexibility to account all the important aspects of the analysis with less computational effort.

- Mesh sensitivity studies have proven to be necessary for FEA, although the results by means of rotational speed, sliding energy and driving torque remain unaffected. Depending on the analysis performed, the mesh size is of the essence in deriving accurate results by means of stress distribution. In case of the mechanical model, the mesh element of 5e-06 kg have proven to give a good fidelity in the structure and to provide accurate results. A further improvement of the meshing, increased the computational time while there was not any visible change in the accuracy of the results.

8.3 Parametric studies of thermo-mechanical models

The mechanical model of lock-plate to seal segment interaction managed to give a picture of the impact between turbines. However, the mechanical model was incapable to simulate wear propagation or material failure. The stresses applied on the structure lead to a strain which could not reach the maximum strain of the nickel alloy material. Hence, an additional parameter proven to have a critical role in wear propagation. This parameter was temperature.

Generally, when two surfaces slid under high loading conditions, the friction energy is dissipated between structures as heat. Therefore, a compulsory demand is that the model need to capture temperature effects. The development of a model which involves thermo-mechanical analysis have been carried out. An excessive parametric studies performed to analyse their influence on the temperature distribution and the wear propagation. The main outputs involve:

- The performance of thermo-mechanical analysis is a compulsory requirement for the impact between turbines. Wear propagation can be captured only if the model accounts for temperature distributions in addition to the stress, strains and strain rate effects.

- Parametric studies, based on the knowledge gained from mechanical analysis, have been carried out in the view of understanding how critical parameters affect wear propagation and temperature increase.

- Material Johnson Cook has the potential to simulate the wear propagation based on the stresses, temperature and strain rate assigned to the structures.

- The failure of the material begins early after the first interaction. The pressure acting on the surface of the seal segment facilitates the increase in stresses and temperature leading to a fast wear propagation.

- Damping is of the essence in the case of thermo-mechanical analysis. As mentioned in mechanical model, the structure is stiffer that the real structure of the NGVs. Therefore, the damping of the system is applied in the view of eliminate continuous axial vibrations of the free rotor. The parametric studies showed that not accounting for the damping of the oscillation can lead to overestimation of the wear progression. Hence, damping control needs to be encompassed in a thermo-mechanical model to capture the material failure based on the response of the real engine.

- Mesh size affects the failure of the material. Special attention is required in order to identify the proper mesh size for the impact analysis. In the context of this work, mesh sensitivities studies have been performed to decide about the mesh density based on results of temperature and stress distribution on the contacted surfaces.

8.4 Generic modelling

FE solver is proven to be the most promising way of analyzing severe impacts, however few challenges arose regarding its applicability in long events. To overcome these challenges, a generic methodology is developed which manages to combine LSDYNA results with structural analysis calculations. The main features of the generic methodology comprise:

- Capability to capture the impact event and the wear propagation:

- Applicability in different engine geometries and loading conditions
- Convenience in use
- Quick enough for preliminary design
- Easily integrated with other tools

8.5 Evaluation of LSDYNA results

The lack of previous knowledge of modelling techniques in such severe impact of turbines in conjunction with the absence of experimental data on the interaction between turbines provoke a troublesome issue in FEA results' evaluation. The answer to the assessment of the modelling emerged from an extensive literature survey regarding available experimental data of ballistic impact scenarios and pin-on-disc interactions under high sliding velocities.

8.5.1 Pin on disc analysis

Pin on disc interaction assisted in understanding the applicability of the non dimensional parameters and provided evidence that the thermo-mechanical analysis is able to predict the mass that melts away due to high temperature distribution on the sliding surfaces. The main contribution of the pin-on-disc experiments is highlighted below:

- Sliding conditions affect the surface temperature and wear propagation
- The constitutive model of Johnson Cook is capable of capturing the melting wear through element deletion
- Non dimensional maps can be used in order to compare the results with available experimental data on pin on disc even if the geometric features and the material characteristics differ
- Results of LSDYNA simulation showed good agreement with the semi-empirical numerical models which have been calibrated against experimental data.

- Pin on disc simulations assisted in the development of the generic methodology while the validation of the simulation results with the experimental data provided evidence about the capability of the FEA solver to estimate wear propagation

8.5.2 Ballistic impact

Ballistic impact analysis have been carried out to quantify possible simulation errors in the estimation of the response of the structures after impact. In addition, they have been used to assess the importance of contact definition and observe possible error in the modelling strategy. The main conclusions derived from this analysis are summarised below:

- Contact definitions needs to be defined carefully in accordance with the demands of the impact. Simulation errors are possible to lead to misunderstanding of the impact and the response of the structures

- Simulation errors are included in the analysis to present the effect of element interpenetration and soft material response in the estimation of axial position, kinetic energy and internal energy of the impactor

- The knowledge gained through the ballistic tests can assist in the comprehension of the impact while the modelling techniques validated with respect to experimental data on ballistic experiments which have been conducted to analyse the capability of the aircraft casing to withstand fragments of high kinetic energy

8.6 Applicability of the research to estimate the response of real events

The generic model has the potential to be applied to simulate the turbines in contact during the shaft failure event. The most significant asset of the numerical model is its applicability in simulating different scenarios including structures of varied geometric features. The numerical tool of the map based approach has the potential to investigate the shaft failure event from the structural interaction point of view and can be implemented as a tool to quantify the effect of structural interaction in the behavior of the free turbine.

8.6.1 Engine failure A-Validation with real engine data

WENSAT enables the first blade to vane interaction to be estimated and the derived results have been assessed with real engine data. In the context of the generic modelling, the non dimensional maps of friction power and wear rate with respect to normalized load and rotational speed have been implemented as a database. This is vitally important as it enables the predictions to be applied accounting for the geometric featured of the structure. Vibration data available for the case of engine A indicate that in terms of blade tangling occurrence, the estimation is valid.

The discretization of the structure in finite volumes was able to capture the propagation of the wear on the seal segment and the platform of the NGVs and rearward displacement of the free rotor. WENSAT is employed to understand the effect of load, friction coefficient, geometric features and collision in the progression of the event.

8.6.2 Engine failure B

The response of the non-dimensional parameters with time is presented showing the effect of the surge in wear rate and friction power. The results of rotational speed, driving torque, frictional energy and wear propagation are compared with engine data and the importance of secondary air system is reported with correspondence to the wear propagation.

The analysis performed highlights the importance of the secondary air dynamics system in the propagating of the shaft failure. According to (2), non including the cavity pressure can lead to an overestimation of the amount of friction by about one third. This explains why the terminal speed is predicted 5% lower than the data derived from the bore growth. This issue can be overcome by integrating the wear estimation numerical analysis into the SAS (Secondary Air System dynamics code) and accounting for the cavity pressure.

8.6.3 Friction coefficient

The friction coefficient has a considerable effect on the results. The sliding between different materials may result in accelerating the occurrence of blade tangling limiting the power of the free turbine earlier. An asset of higher friction coefficient involves the occurrence of blade tangling under lower rotational speed. This would be a beneficial design characteristics since blade fragments will attain lower kinetic energy at the the time of the impact with the containment.

8.6.4 Geometric effects

Modification in the seal segment thickness and mean radius are proven to be beneficial for the evolution of the shaft failure event. A decrease in the thickness or the mean radius accelerates the occurrence of blade tangling. Considering that earlier occurrence of blade tangling necessitates the higher friction power with a corresponding decrease in driving torque. Additional advantage involves the reduction of the rotational speed when blade interaction is established. This is a positive aspect mainly because the blade fragments are ejected with lower rotational speed.

8.6.5 Impact effect

The momentum of the free turbine can also facilitate the wear propagation and the blade tangling occurrence. The high kinetic energy of the turbine is converted into internal energy of the structures increasing the temperature and the stresses on the interface surface. When the velocity of the free turbine at the time of the impact is high, mass loss is precipitated leading to blade tangling. Therefore, the existence of high amplitude vibration of the structure in axial direction can accommodate the safety of the event avoiding high debris release.

8.7 Recommendations for future work

Various methodologies for simulating turbine structures in contact following a shaft failure event have been investigated over the last three years using FE analysis. The analysis has been focused on:

- the development of 3D models of the turbines in contact able to capture thermo-mechanical structure interaction leading to wear and ultimate failure
- the definition of a generic approach using non-dimensional parameters and a map based scheme to derive the evolution of wear, dislocation and rotational speed with time

The scheme developed so far has demonstrated a lot of potential. It can predict the occurrence of blade tangling reasonably well (compared against engine vibration data from a shaft failure event). This implies/necessitates that the evolution of wear and dislocation with time are also reasonably well predicted. Moreover, the calculated terminal speed attained seems to align well against Rolls-Royce data for the same event.

More work on the subject is necessary in order to enhance further the current understanding of the nature and evolution of shaft failure events, the nature of the impact between engine components, the estimation of the energy loss due to the various structural/thermal interactions and their combined effects on the rotational speed of a free running turbine. Further work should also take into consideration different engine architectures.

In the following paragraphs, areas of interest relating to the shaft failure scenario are concisely presented:

8.7.1 Impact of blade fragments on the turbine casing and the adjacent blades

Blade tangling during over-speed may lead to the release of blade fragments. Blade fragments can be either parts of the rotor tips or even complete blades. Depending on the energy and the size of the fragments released, the turbine casing will either be capable of containing these fragments or might fail at areas of high pressure.

Similar modelling techniques (to the ones already developed within the context of this work) can be implemented to predict the response of the engine's casing taking into account fragments of different size, weight, velocity, energy and direction. The characteristics of the fragments will be directly related to the applied torque on the rotor, due to the impingement of hot gas, and the interaction with the static arrangement (impact with adjacent rotor blades and casing) after release. A consistent analysis can be performed in order to estimate the effect of the blade fragments on the turbine casing. Such an analysis could point out the conditions under which a non-containment failure would occur or how it could be prevented.

Furthermore, extreme scenarios of disc bursting can be simulated. The case of disc burst due to over-speed conditions and its interaction with the containment can be simulated to provide understanding of the impact and quantify the loss in translational and rotational energy while getting through the casing.

8.7.2 Orbit of the rotor

The unbalanced force induced by the ejection of blades may result in the rotor orbiting. The remaining blades begin to contact with the containment case with a combination of impact and rub. As a consequence, the blade tips can deform or even fail while the rotor can slow down due to the rubbing of the tips on the casing.

The analyses conducted so far have neglected the effects of any unbalanced forces that may arise due to blade/disc fragmentation. A further analysis including the orbit of the turbine wheel can provide information about its effect on terminal rotational speed and the interaction of the remaining blades with the casing.

8.7.3 Engine geometry

The geometric characteristics of the structures in contact seem to play a significant role in the determination of the blade tangling, blade failure mode and the size of the blade fragments released. Different engine architectures can be investigated to provide a better insight into the areas that are vulnerable from the axial displacement of the turbine rotor. So far the investigations conducted considered only one scenario based on a particular engine geometry i.e. that the first contact interaction occurs between the lock-plate of the disc and the seal segment. Modern turbine architectures allow for a more direct contact of the seal segment with the IPT blade roots. This may lead to the rapid release of a considerable amount of blades from the root.

8.7.4 Numerical algorithm

For a truly predictive/generic capability, the map-based scheme already developed can be further expanded to include the effects of blade tangling, rotor orbiting and blade release mode in the calculation of the frictional power, moment of inertia, driving torque etc.

References

[1] INTERNET SOURCE. *www.iasa.com.au*. 2010. vi, 1

[2] A. L. ROWE. **Shaft failure review - Large fan engines**. *Performance technical Report, Rolls-Royce,PTR90865*, 2003, p.p.1134-1138. vi, 12, 14, 16, 17, 18, 19, 20, 84, 137, 138, 140, 161

[3] D. MCCARTHY. **Types of rotor failure and characteristics of fragments**. *A workshop held at the Massachusetts Institute of Technology,NASA CP-2017,p.p.65-92*, 1977. vi, 23, 24

[4] J. D. REID AND N. R. HISER. **Friction modelling between solid elements.** *International Journal of Crashworthiness, Vol. 9, No. 1, pp. 65-72*, 2004. vi, 26, 28

[5] Q. E. SUN. **Shear Locking and Hourglassing in MSC Nastran, ABAQUS, and ANSYS**. 2006. vi, 29, 30

[6] S. HALE. **The use of LS-DYNA models to predict containment of disk burst fragments**. 10^{th} *International LS-DYNA Users Conference*, 2008. vi, 31

[7] H. UETZ AND J. FOHL. **Wear as an energy transformation process**. *Wear 49*, 1977,p.p.253-264. vii, 33

[8] F.E. KENNEDY. **Thermomechanical phenomena in high speed rubbing**. *Wear,59,p.p.149-163*, 1980. vii, 34

[9] S.C. LIM AND M.F. ASHBY. **Wear-mechanism maps**. *Acta metall.,Vol.35,No.1,p.p.1-24*, 1987. vii, viii, 35, 36, 92, 94, 101, 102

[10] G.R. JOHNSON AND W.H. COOK. **Fracture characteristics of three metal subjected to various strains, strain rates, temperatures and pressures**. *Engineering Fracture Mechanics, Vol.21,No.1,p.p.31-48*, 1985. vii, 63, 64

[11] Ambur, D. R., Jaunky, N., Lawson, R. E., Knight, N. F. Jr.. **Numerical simulation for high-energy impact of thin plates**. *International Journal of Impact Engineering, Vol.25,p.p.683-702*, 2001. viii, xi, 105, 106

[12] N. F. Jr. Knight, N. Jaunky, Robin E., D Lawson, and R. Ambur. **Penetration simulation for uncontained engine debris impact on fuselage-like panels using LS-DYNA**. *Finite Elements in Analysis and Design*, **36**:99–133, 2000. viii, 22, 103, 106

[13] K. N. Singh, Klingbeil D., and Sievert R. **Simulation of ballistic impact tests under various conditions for a nickel-base superalloy**. *J.Phys.IV France, Vol.134,p.p. 299-304*, 2006. xi, 65, 66, 103

[14] L. Witek. **Failure analysis of turbine disc of an aero engine**. *Engineering Failure Analysis,Vol.13, p.p.9-17*, 2003. xi, 25, 46, 65

[15] P. Duo and D. Nowell. **Predictive Numerical Modelling of foreign object damage**. *8th International LS-DYNA Users Conference*. 22

[16] K. Carney, M. Pereira, D. Revilock, and P. Matheny. **Jet engine fan blade containment using two alternate geometries**. *4th European LS-DYNA Users Conference*. 22

[17] G Toussaintia, A. Gakwaya, D. Nandlallb, A. Caulfeild, and A. Shahkarami. **Numerical modelling methodology for an advanced lightweight debris containment system**. *23RD INTERNATIONAL SYMPOSIUM ON BALLISTICS*, TARRAGONA, SPAIN 16-20 APRIL 2007. 22, 103

[18] M.J. Stallone, V. Gallardo, A.F. Storace, L.J. Bach, G. Black, and E.F. Gaffney. **Plastic deformation and sliding friction of metals**. *AIAA Journal, Vol.21(8)*, 1983, p.p.1134-1138. 22

[19] N. Cosme, D. Chevrolet, and J. Bonini. **AIAA 2002-1666, April 2002**. *AIAA 2002-1666*, 2002. 22

[20] Y.N. Shmotin, V.G. Gabov, A.A. Ryabov, S.S. Kukavon, and V. Rechkin. **Numerical Analysis of Aircraft Fan Blade-out**. *AIAA 2006-4620*, 2006. 22

[21] K.S. Carney, C. Lawrence, and D.V. Carney. **Aircraft engine blade-out dynamics**. *7th International LSDYNA Users Conference,Detroit*, 2002. 22

[22] C. Lawrence, K. Carney, and V. Gallardo. **Simulation of Aircraft Engine Blade-Out Structural Dynamics**. *NASA / TM-2001-210957/REV1*, 2001. 22

[23] M. Heidari, D. Carlson, S. Sinha, R. Sadeghi, C Heydari, H. Bayoumi, and J. Son. **An efficient multi-discriplanary simualtion of engine fan-blade out event using MD Nastran**. *49th AIAA/ASME/ASCE/AHS/ASC Structures,Structural Dynamics and Materials*, 7-10 April,2008,Schaumburg, IL. 23

[24] S. Sarkar and S. N. Alturi. **Effects of multiple blade interaction on the containment of blade fragments during a rotor failure**. *Finite Elements in Analysis and Design*, 1996. 24

[25] A. Kraus and J. Frischbier. **Containment and Penetration simulation in case of blade loss in a low pressure turbine**. *DYNAmore LSDYNA Forum*, 2002. 24

[26] D.A. Shokey, J.H. Giovanola, J.W. Simons, D.C. Erlich, R.W. Klopp, and S.R. Skaggs. **Advanced armor technology:application potential for engine fragment barriers for commercial aircraft**. *U.S.Department of Transportation Federal Aviation Administration*, **DOT/FAA/AR-97/53**, 1997. 25, 103

[27] J.A. Zukas and D.R. Scheffler. **Practical aspects of numerical simulations of dynamic events: effects of meshing**. *International Journal of Impact Engineering 24*, 2000,p.p.925-945. 25

[28] J. O. Hallquist. **LS-DYNA Theory Manual. Livermore Software Technology Corporation, Livermore, CA**. LS-DYNA Theory Manual. Livermore Software Technology Corporation, Livermore, CA. 26, 28, 29, 32, 46, 49, 67

[29] T.J.R. Hughes. **The finite element method : Linear static and dynamic finite element analysis**. *Dover Publicatios, INC*, 2000. 29, 45

[30] T. Belytschko, W.K. Liu, and B. Moran. **Nonlinear finite elements for continua and structures**. *John Wiley and Sons, LTD*, 2001. 30

[31] J. O. Hallquist. **LS-DYNA KEYWORD User's Manual. Livermore Software Technology Corporation, Livermore, CA**. 2007. 30, 45, 49

[32] B. Bhushan. **Principles of Tribology**. *Modern Tribology Handbook, Volume one*, 2000. 35

[33] M.F. Ashby and S.C. Lim. **Wear mechanic maps**. *Scripta Mettalurgica, Vol.24,p.p805-810*, 1990. 37, 93

[34] R.S. Montgomery. **Friction and wear at high sliding speeds**. *Wear, Vol.36,p.p.275-298*, 1976. 37, 93, 101

[35] P. Capozzi. **Friction/Wear Modelling of a Free-Running Turbine Wheel during Shaft Failure**. *MSc Thesis, Cranfield University, School of Engineering*, 2008. 56, 67

[36] J.R. Barber and M. Ciavarella. **Contact mechanics**. *International Journal of Solids and Structures 37*, 2000,p.p.29-43. 57

[37] I. Rojo. **Friction/Wear Modelling of a Free-Running Turbine Wheel during Shaft Failure**. *MSc Thesis, Cranfield University, School of Engineering*, 2009. 60, 67, 69

[38] R. Pardo de Santayana. **Wear/friction of turbine rotor and stator during shaft failure**. *MSc Thesis, Cranfield University, School of Engineering*, 2010. 82

[39] J. F. Archard. **Contact and rubbing of flat surfaces**. *Journal of Applied Physics, Vol.24,p.p.225-249*, 1999. 92, 111

[40] F.H. Kinsella and T.H.C Childs. *Inst. Mech. Engrs. Conf.*, 1978,p.p.55. 92, 101

[41] D.A. Rigney and J.P. Hirth. **Plastic deformation and sliding friction of metals**. *Wear,53,p.p.345-370*, 1979. 92

[42] A.D. Sarkar. **Friction and wear**. *Academic Press*, 1980. 92

[43] J. F. Archard. **The temperature of the rubbing surfaces**. *Wear, Vol.2,p.p.438-455*, 1958. 93

[44] Y.A. Cengel. **Heat transfer :A practical approach**. *McGraw-Hill*, 1997. 93

[45] Mueller R.B. Lundin, S.J. **Advanced aircraft materials, engine debris penetrationtesting**. *U.S.Department of Transportation Federal Aviation Administration*, **DOT/FAA/AR-03/37**, 2005. 103

[46] D. McMillan. **BR715 LP Turbine-Assessment of coefficient of friction for overspeed protection**. *Technical report*, 1997. 110, 113, 124

[47] E. Rabinowicz. **Friction and wear of materials**. *John Wiley and Sons, Inc.,second edition*, 1995. 140

APPENDIX A

A.1 Ballistic impact partial key file

```
*KEYWORD 90000000
*TITLE
$# title
LS-DYNA keyword deck by LS-Prepost

*CONTROL_CONTACT
$#  slsfac    rwpnal    islchk    shlthk    penopt    thkchg     orien
enmass
  0.008000     0.000         0         0         1
$#  usrstr    usrfrc     nsbcs    interm     xpene     ssthk      ecdt
tiedprj
         0         0         0         0     0.000         0         0
0
$#   sfric     dfric       edc       vfc        th     th_sf    pen_sf
     0.000     0.000     0.000     0.000     0.000     0.000     0.000
$#  ignore    frceng   skiprwg    outseg   spotstp   spotdel   spothin
         0         0         0         0         0         0     0.000

*CONTROL_ENERGY
$#    hgen      rwen    slnten     rylen
         2         2         2         2

*CONTROL_HOURGLASS
$#     ihq        qh
         1  0.100000

*CONTROL_OUTPUT
$#   npopt    neecho    nrefup    iaccop     opifs    ipnint    ikedit
iflush
         0         0         0         0     0.000         0         0
0
$#   iprtf    ierode     tet10    msgmax    ipcurv
         0         0         2        50

*CONTROL_PARALLEL
$#    ncpu    numrhs     const      para
         4         0         2

*CONTROL_TERMINATION
$#  endtim    endcyc     dtmin    endeng    endmas
  0.001000

*CONTROL_TIMESTEP
$#  dtinit    tssfac      isdo    tslimt     dt2ms      lctm     erode
ms1st
     0.000  0.600000         0     0.000     0.000         0         1
$#  dt2msf   dt2mslc     imscl
     0.000         0         0
```

```
*DATABASE_GLSTAT
$$DATABASE_OPTION -- Control Cards for ASCII output
$#      dt    binary      lcur     ioopt
 1.0000E-5         1

*DATABASE_MATSUM
$#      dt    binary      lcur     ioopt
 1.0000E-5         1

*DATABASE_BINARY_D3PLOT
$#      dt      lcdt      beam     npltc
 2.5000E-5
$#   ioopt
         0

*CONTACT_ERODING_SURFACE_TO_SURFACE_ID
$HMNAME GROUPS       1contact
$HWCOLOR GROUPS       1       3
$#     cid
title
         1
$#    ssid      msid     sstyp     mstyp    sboxid    mboxid       spr
mpr
         3         1         3         3
$#      fs        fd        dc        vc       vdc    penchk        bt
dt
     0.000     0.000     0.000     0.000     0.000         0     0.000
0.000
$#     sfs       sfm       sst       mst      sfst      sfmt       fsf
vsf
     0.000     0.000     0.000     0.000     0.000     0.000     0.000
0.000
$#    isym    erosop      iadj
         0         1         1

*PART
$# title

$HMNAME COMPS       1target
$HWCOLOR COMPS       1       4
$#     pid     secid       mid     eosid      hgid      grav    adpopt
tmid
         1         1         5         2

*SECTION_SOLID
$HMNAME PROPS       1solid
$#   secid    elform       aet
         1         1

*MAT_JOHNSON_COOK
$HMNAME MATS       5material 15
$#     mid        ro         g         e        pr       dtf        vp
         5 2780.00002.8000E+10     0.000     0.000     0.000  0.000000
$#       a         b         n         c         m        tm        tr
epso
 3.6900E+8 6.8400E+8  0.730000  0.008300  1.700000 775.00000 300.00000
1.000000
```

```
$#      cp        pc     spall        it        d1        d2        d3
d4
 875.00000         0  0.000000     0.000  0.112000  0.123000  1.500000
0.007000
$#      d5
     0.000

*EOS_GRUNEISEN
$HMNAME PROPS       2eos
$#   eosid         c        s1        s2        s3     gamao         a
e0
         2 5240.0000  1.338000     0.000     0.000  2.000000  0.460000
$#      v0
  1.000000

*PART
$# title

$HMNAME COMPS       2target_frame
$HWCOLOR COMPS       2       3
$#     pid     secid       mid     eosid      hgid      grav    adpopt
tmid
         2         1         3

*MAT_PLASTIC_KINEMATIC
$HMNAME MATS       3steel
$#     mid        ro         e        pr      sigy      etan      beta
         3 7750.00002.0700E+11  0.300000 2.4100E+9 1.0300E+9  0.230000
$#     src       srp        fs        vp
     0.000     0.000     0.000  1.000000

*PART
$# title

$HMNAME COMPS       3projectile
$HWCOLOR COMPS       3      21
$#     pid     secid       mid     eosid      hgid      grav    adpopt
tmid
         3         1         2

*MAT_PLASTIC_KINEMATIC
$HMNAME MATS       2titanium
$#     mid        ro         e        pr      sigy      etan      beta
         2 4430.00001.1000E+11  0.300000 8.2700E+8 2.0700E+9  0.200000
$#     src       srp        fs        vp
     0.000     0.000     0.000  1.000000

*SECTION_SOLID
$HMNAME PROPS       3solid_target
$#   secid    elform       aet
         3         2
```

```
*MAT_PLASTIC_KINEMATIC
$HMNAME MATS       1aluminium
$#     mid        ro         e        pr      sigy      etan      beta
         1 2770.00006.8900E+10  0.300000 3.4500E+8 6.8900E+8  0.200000
$#     src       srp        fs        vp
     0.000     0.000  0.200000  1.000000

*MAT_PIECEWISE_LINEAR_PLASTICITY
$HMNAME MATS       4aluminium_mat24
$#     mid        ro         e        pr      sigy      etan      fail
tdel
         4 2770.00006.8900E+10  0.300000 3.4500E+8 6.8900E+8  0.200000
1.0000E-8
$#       c         p      lcss      lcsr        vp
 40.000000  5.000000         0         0  1.000000

*INITIAL_VELOCITY_GENERATION
$HMNAME LOADCOLS       1initial velocity
$HWCOLOR LOADCOLS       1       3
$#nsid/pid      styp     omega        vx        vy        vz
         3         2     0.000 95.097603
$#      xc        yc        zc        nx        ny        nz     phase
     0.000     0.000     0.000     0.000     0.000     0.000         0
*ELEMENT_SOLID
$#   eid     pid      n1      n2      n3      n4      n5      n6      n7
n8
   37181       1    1150    1152    1145    1146   37622   37623   37624
37625
....................................................

*NODE
$#   nid               x               y               z      tc      rc
      29           0.000       0.4064000       0.3386667
....................................................
*END
```

A.2 Pin on disc partial key file

```
*KEYWORD MEMORY=900000000
*TITLE
$# title
LS-DYNA keyword deck by LS-Prepost

*CONTROL_CONTACT
$#  slsfac    rwpnal    islchk    shlthk    penopt    thkchg     orien
enmass
  0.100000     0.000         1         0         0         0         1
0
$#  usrstr    usrfrc     nsbcs    interm     xpene     ssthk      ecdt
tiedprj
         0         0         0         0  4.000000         0         0
0
$#   sfric     dfric       edc       vfc        th     th_sf    pen_sf
     0.000     0.000     0.000     0.000     0.000     0.000     0.000
$$  IGNORE    FRCENG   SKIPRWG    OUTSEG   SPOTSTP   SPOTDEL   SPOTHIN
$#  ignore    frceng   skiprwg    outseg   spotstp   spotdel   spothin
         0         1         0         0         0         0     0.000
$#    isym    nserod    rwgaps    rwgdth     rwksf      icov    swradf
ithoff
         0         0         0     0.000  1.000000         0     0.000
0
$#  shledg
         0

*CONTROL_ENERGY
$#    hgen      rwen    slnten     rylen
         2         2         2         2

*CONTROL_PARALLEL
$#    ncpu    numrhs     const      para
         4         0         2         0

*CONTROL_SOLUTION
$$    SOLN
$#    soln       nlq     isnan     lcint
         2         0         0         0

*CONTROL_TERMINATION
$#  endtim    endcyc     dtmin    endeng    endmas
  0.100000         0     0.000     0.000     0.000
*CONTROL_THERMAL_NONLINEAR
$#  refmax       tol       dcp    lumpbc    thlstl    nlthpr    phchpn
        10 1.0000E-4     0.000         0     0.000         0     0.000
```

```
*CONTROL_THERMAL_SOLVER
$#   atype     ptype    solver     cgtol       gpt    eqheat     fwork
sbc
         1         1         3 1.0000E-4         1  1.000000  1.000000
0.000

*CONTROL_THERMAL_TIMESTEP
$#      ts       tip       its      tmin      tmax     dtemp      tscp
lcts
         0  1.000000 6.1700E-8     0.000     0.000 100.00000  0.500000
0

*CONTROL_TIMESTEP
$#  dtinit    tssfac      isdo    tslimt     dt2ms      lctm     erode
ms1st
     0.000  0.900000         0     0.000     0.000         0         0
0
$#  dt2msf   dt2mslc     imscl
     0.000         0         0

*DATABASE_GLSTAT
$$DATABASE_OPTION -- Control Cards for ASCII output
$#      dt    binary      lcur     ioopt
 1.0000E-4         1         0         0

*DATABASE_MATSUM
$#      dt    binary      lcur     ioopt
 5.0000E-4         1         0         0

*DATABASE_TPRINT
$#      dt    binary      lcur     ioopt
 5.0000E-4         1         0         0

*DATABASE_BINARY_D3PLOT
$#      dt      lcdt      beam     npltc    psetid
 1.0000E-4         0         0         0         0
$#   ioopt
         0

*DATABASE_BINARY_INTFOR
$#      dt      lcdt      beam     npltc    psetid
  0.005000         0         0         0         0

*BOUNDARY_PRESCRIBED_MOTION_RIGID
$HMNAME LOADCOLS       1boundary
$HWCOLOR LOADCOLS       1       3
$#     pid       dof       vad      lcid        sf       vid     death
birth
         5         5         0         1 46193.000         0     0.000
0.000


*LOAD_SEGMENT_SET
$HMNAME LOADCOLS       3LoadSegSet_3
$HWCOLOR LOADCOLS       3       3
$#    ssid      lcid        sf        at
         2         1 1.0000E+8     0.000
```

```
*LOAD_SURFACE_STRESS
$#     pid
         6
$#  lscid1    lscid2    lscid3    lscid4    lscid5    lscid6    lscid7
lscid8
         0         0         0         0         0         0         0
0
$#  uscid1    uscid2    uscid3    uscid4    uscid5    uscid6    uscid7
uscid8
         0         0         0         0         0         0         0
0

*CONTACT_AUTOMATIC_SURFACE_TO_SURFACE_ID
$HMNAME GROUPS       2ASurf2Surf_2
$HWCOLOR GROUPS       2       3
$#     cid
title
         2
$#    ssid      msid     sstyp     mstyp    sboxid    mboxid       spr
mpr
         6         5         3         3         0         0         1
1
$#      fs        fd        dc        vc       vdc    penchk        bt
dt
  0.130000     0.000     0.000 4.5700E+6 20.000000         0
0.0001.0000E+20
$#     sfs       sfm       sst       mst      sfst      sfmt       fsf
vsf
  1.000000  1.000000     0.000     0.000  1.000000  1.000000  1.000000
1.000000

*PART
$HMNAME COMPS       5disc
$HWCOLOR COMPS       5       4
$# title
disc
$#     pid     secid       mid     eosid      hgid      grav    adpopt
tmid
         5         1         1         0         0         0         0
4

*SECTION_SOLID
$HMNAME PROPS       1section_ring
$#   secid    elform       aet
         1         1         0

*MAT_RIGID
$HMNAME MATS       1mat_rigid
$#     mid        ro         e        pr         n    couple         m
alias
         1 7850.00002.1000E+11  0.300000     0.000     0.000     0.000
$#     cmo      con1      con2
  1.000000         7         5
$#lco or a1        a2        a3        v1        v2        v3
     0.000     0.000     0.000     0.000     0.000     0.000
```

```
*PART
$HMNAME COMPS       6pin
$HWCOLOR COMPS       6       5
$# title
pin
$#     pid     secid       mid     eosid      hgid      grav    adpopt
tmid
         6         1         2         2         1         0         0
4

*MAT_JOHNSON_COOK
$HMNAME MATS       2mat 15
$#     mid        ro         g         e        pr       dtf        vp
         2 7850.00007.6900E+10     0.000     0.000     0.000  1.000000
$#       a         b         n         c         m        tm        tr
epso
 9.1000E+8 5.8600E+8  0.260000  0.014000  1.030000 1800.0000 300.00000
1.000000
$#      cp        pc     spall        it        d1        d2        d3
d4
 465.00000 -1.000E+6  1.000000     0.000 -0.800000  2.100000 -0.500000
0.002000
$#      d5
  0.610000

*EOS_LINEAR_POLYNOMIAL
$HMNAME PROPS       2EOS1_2
$#   eosid        c0        c1        c2        c3        c4        c5
c6
         2     0.0002.1000E+11     0.000     0.000     0.000     0.000
0.000
$#      e0        v0
     0.000     0.000

*PART
$HMNAME COMPS       7pin_upper
$HWCOLOR COMPS       7       6
$# title
pin_upper
$#     pid     secid       mid     eosid      hgid      grav    adpopt
tmid
         7         1         5         0         0         0         0
4

*MAT_RIGID
$HMNAME MATS       5rigid_pin
$#     mid        ro         e        pr         n    couple         m
alias
         5 7850.00002.1000E+11  0.300000     0.000     0.000     0.000
$#     cmo      con1      con2
  1.000000         5         7
$#lco or a1        a2        a3        v1        v2        v3
     0.000     0.000     0.000     0.000     0.000     0.000
*HOURGLASS
$HMNAME PROPS       1HourGlas_1
$#    hgid       ihq        qm       ibq        q1        q2    qb/vdc
qw
```

```
         1         4  0.100000         0  1.500000  0.060000  0.100000
0.100000

*MAT_PLASTIC_KINEMATIC
$HMNAME MATS       3MATL3_3
$#     mid        ro         e        pr      sigy      etan      beta
         3 7850.00002.1000E+11  0.300000 7.9200E+82.1000E+10  1.000000
$#     src       srp        fs        vp
 40.000000  5.000000     0.000  1.000000

*MAT_THERMAL_ISOTROPIC
$HMNAME MATS       4MATT1_1
$#    tmid       tro     tgrlc    tgmult      tlat      hlat
         4     0.000     0.000     0.000 1800.0000 2.1000E+9
$#      hc        tc
 465.00000 41.000000

*INITIAL_TEMPERATURE_SET
$HMNAME LOADCOLS       4InitialTemp_3
$HWCOLOR LOADCOLS       4       4
         3 900.00000         0

*DEFINE_CURVE
$HMNAME CURVES       1LoadCurve_1
$HWCOLOR CURVES       1       3
$HMCURVE     2    2 LoadCurve1
$#    lcid      sidr       sfa       sfo      offa      offo    dattyp
         1         0  1.000000  1.000000     0.000     0.000         0
$#                a1                  o1
               0.000           1.0000000
           5.0000000           1.0000000

*SET_NODE_LIST
$$
$$ Sets Defined In HyperMesh
$$
$HMSET
$HMNAME SETS       3nodes_all
$#     sid       da1       da2       da3       da4
         3     0.000     0.000     0.000     0.000
$#    nid1      nid2      nid3      nid4      nid5      nid6      nid7
nid8
     84295     84296     84297     84298     84299     84300

*SET_NODE_LIST
$HMSET
$HMNAME SETS       4Set_4
$#     sid       da1       da2       da3       da4
         4     0.000     0.000     0.000     0.000
$#    nid1      nid2      nid3      nid4      nid5      nid6      nid7
nid8
    347891    347892    347893    347894    347895    347896 .........
...................................................
```

```
*SET_SEGMENT
$HMNAME CSURFS       2segment
$HWCOLOR CSURFS       2      37
$#     sid       da1       da2       da3       da4
         2     0.000     0.000     0.000     0.000
$#      n1        n2        n3        n4        a1        a2        a3
a4
    347905    347903    347904    347904     0.000     0.000     0.000
0.000
....................................................
*ELEMENT_SOLID
$#   eid     pid      n1      n2      n3      n4      n5      n6      n7
n8
  291997       6 1015324 1015329 1015367 1015366  310208  310209  310210
310211
...................................................
*NODE
$#   nid               x               y               z      tc      rc
   84295           0.000       0.0092781       0.0168094       0       0
...................................................
*END
```

A.3 Thermo-mechanical analysis partial input key file: Lock-plate to seal segment interaction

```
*KEYWORD
*TITLE
$# title
LS-DYNA keyword deck by LS-Prepost

*CONTROL_CONTACT
$#  slsfac    rwpnal    islchk    shlthk    penopt    thkchg     orien
enmass
  0.100000     0.000         1         0         0         0         1
0
$#  usrstr    usrfrc     nsbcs    interm     xpene     ssthk      ecdt
tiedprj
         0         0         0         0  4.000000         0         0
0
$#   sfric     dfric       edc       vfc        th     th_sf    pen_sf
     0.000     0.000     0.000     0.000     0.000     0.000     0.000
$#  ignore    frceng   skiprwg    outseg   spotstp   spotdel   spothin
         1         1         0         0         0         0     0.000
$#    isym    nserod    rwgaps    rwgdth     rwksf      icov    swradf
ithoff
         0         0         1     0.000  1.000000         0  1.000000
0
$#  shledg
         0

*CONTROL_ENERGY
$#    hgen      rwen    slnten     rylen
         2         2         2         2

*CONTROL_HOURGLASS
$#     ihq        qh
         6  0.300000

*CONTROL_MPP_DECOMPOSITION_AUTOMATIC

*CONTROL_NONLOCAL
$#     mem
        20

*CONTROL_PARALLEL
$#    ncpu    numrhs     const      para
         8         0         2         0

*CONTROL_SOLUTION
$#    soln       nlq     isnan     lcint
         2         0         0         0

*CONTROL_TERMINATION
$#  endtim    endcyc     dtmin    endeng    endmas
  0.035000         0     0.000     0.000     0.000
```

```
*CONTROL_THERMAL_NONLINEAR
$#  refmax       tol       dcp    lumpbc    thlstl    nlthpr    phchpn
       100 1.0000E-6  0.500000         0     0.000         0     0.000

*CONTROL_THERMAL_SOLVER
$#   atype     ptype    solver     cgtol       gpt    eqheat     fwork
sbc
         1         1        12 1.0000E-4         1  1.000000  1.000000
0.000

*CONTROL_THERMAL_TIMESTEP
$#      ts       tip       its      tmin      tmax     dtemp      tscp
lcts
         0  1.000000 1.0000E-6     0.000     0.000 100.00000  0.500000
0

*CONTROL_TIMESTEP
$#  dtinit    tssfac      isdo    tslimt     dt2ms      lctm     erode
ms1st
     0.000  0.900000         0     0.000     0.000         0         0
0
$#  dt2msf   dt2mslc     imscl
     0.000         0         0

*DATABASE_GLSTAT
$#      dt    binary      lcur     ioopt
  0.002000         1         0         1

*DATABASE_MATSUM
$#      dt    binary      lcur     ioopt
  0.002000         1         0         1

*DATABASE_BINARY_D3PLOT
$#      dt      lcdt      beam     npltc    psetid
 5.0000E-4         0         0         0         0
$#   ioopt
         0

*DATABASE_BINARY_INTFOR
$$ DT/CYCL      LCID
$#      dt      lcdt      beam     npltc    psetid
 2.0000E-4         0         0         0         0

*LOAD_SURFACE_STRESS
$#     pid
        12
$#  lscid1    lscid2    lscid3    lscid4    lscid5    lscid6    lscid7
lscid8
         0         0         0         0         0         0         0
0
$#  uscid1    uscid2    uscid3    uscid4    uscid5    uscid6    uscid7
uscid8
         0         0         0         0         0         0         0
0
        13
         0         0         0         0         0         0         0
0
```

```
         0         0         0         0         0         0         0
0

*CONTACT_AUTOMATIC_SURFACE_TO_SURFACE_ ID
$#     cid
title
         1
$#    ssid      msid     sstyp     mstyp    sboxid    mboxid       spr
mpr
        13        12         3         3         0         0         1
1
$#      fs        fd        dc        vc       vdc    penchk        bt
dt
  0.067000     0.000     0.000 5.6580E+8 20.000000         0
0.0001.0000E+20
$#     sfs       sfm       sst       mst      sfst      sfmt       fsf
vsf
  1.000000  1.000000     0.000     0.000  1.000000  1.000000  1.000000
1.000000
$#      cf      frad       htc     gcrit      gmax   cd_fact    bc_flg
algo
     0.000     0.000     0.000     0.000     0.000  1.000000

*PART
DISC

$#     pid     secid       mid     eosid      hgid      grav    adpopt
tmid
         5         1         7         0         0         0         0
1

*SECTION_SOLID
$HMNAME PROPS       1disc_solid
$#   secid    elform       aet
         1         1

*MAT_RIGID
$HMNAME MATS       7disc rigid material
$#     mid        ro         e        pr         n    couple         m
alias
         7 8220.00001.6890E+11  0.281000     0.000     0.000     0.000
$#     cmo      con1      con2
  1.000000         5         5
$#lco or a1        a2        a3        v1        v2        v3
     0.000     0.000     0.000     0.000     0.000     0.000
*PART
PART OF RING

$#     pid     secid       mid     eosid      hgid      grav    adpopt
tmid
         8         1        13         0         0         0         0
1
```

```
*MAT_PLASTIC_KINEMATIC
$HMNAME MATS      13IN718
$#     mid        ro         e        pr      sigy      etan      beta
        13 8220.00001.6890E+11  0.281000 9.8000E+8 8.7740E+9  1.000000
$#     src       srp        fs        vp
     0.000     0.000     0.000     0.000

*PART
PART OF RING

$HMNAME COMPS      10Part_10
$HWCOLOR COMPS      10       5
$#     pid     secid       mid     eosid      hgid      grav    adpopt
tmid
        10         1        13         0         0         0         0
1

*PART
LOCK-PLATE JOHNSON COOK

$#     pid     secid       mid     eosid      hgid      grav    adpopt
tmid
        12         1        10         1         0         0         0
1

*MAT_JOHNSON_COOK
$HMNAME MATS      10MATL15_10
$#     mid        ro         g         e        pr       dtf        vp
        10 8220.00006.0810E+10     0.000     0.000     0.000  1.000000
$#       a         b         n         c         m        tm        tr
epso
 1.1500E+9 1.3050E+9  0.600000  0.007500  1.300000 1570.0000 300.00000
1.000000
$#      cp        pc     spall        it        d1        d2        d3
d4
 445.00000 -1.000E+6  1.000000     0.000 -0.013400  0.025525  0.300000
0.070000
$#      d5
  2.500000

*EOS_LINEAR_POLYNOMIAL
$HMNAME PROPS       1EOS1_1
$#   eosid        c0        c1        c2        c3        c4        c5
c6
         1     0.0001.6890E+11
$#      e0        v0
     0.000  1.000000

*PART
SEAL SEGMENT JOHNSON COOK

$HMNAME COMPS      13Part_13
$HWCOLOR COMPS      13       7
$#     pid     secid       mid     eosid      hgid      grav    adpopt
tmid
        13         1        10         1         0         0         0
1
```

```
*PART
FIXING

$HMNAME COMPS      15Part_15
$HWCOLOR COMPS      15       8
$#     pid     secid       mid     eosid      hgid      grav    adpopt
tmid
        15         1        12         0         0         0         0
1

*MAT_RIGID
$HMNAME MATS      12fixing rigid material
$#     mid        ro         e        pr         n    couple         m
alias
        12 8220.00001.6890E+11  0.281000     0.000     0.000     0.000
$#     cmo      con1      con2
  1.000000         7         7
$#lco or a1        a2        a3        v1        v2        v3
     0.000     0.000     0.000     0.000     0.000     0.000

*MAT_RIGID
$HMNAME MATS      11ring rigid material
$#     mid        ro         e        pr         n    couple         m
alias
        11 8220.00001.6890E+11  0.281000     0.000     0.000     0.000
$#     cmo      con1      con2
     0.000         0         0
$#lco or a1        a2        a3        v1        v2        v3
     0.000     0.000     0.000     0.000     0.000     0.000

*MAT_THERMAL_ISOTROPIC
$HMNAME MATS       1MATT1_1
$#    tmid       tro     tgrlc    tgmult      tlat      hlat
         1     0.000     0.000     0.000 1570.0000 2.7800E+5
$#      hc        tc
 445.00000 24.000000

*INITIAL_TEMPERATURE_SET
$HMNAME LOADCOLS       3InitialTemp_3
$HWCOLOR LOADCOLS       3       3
$#    nsid      temp       loc
         6 1000.00000

*INITIAL_VELOCITY_GENERATION
$HMNAME LOADCOLS       4initial velocity
$HWCOLOR LOADCOLS       4       7
$#nsid/pid      styp     omega        vx        vy        vz
         5         1 756.20001
$#      xc        yc        zc        nx        ny        nz     phase
     0.000     0.000     0.000  1.000000

*DEFINE_CURVE
$HMNAME CURVES       5torque
$HWCOLOR CURVES       5       4
$HMCURVE     1    3 torque
$#    lcid      sidr       sfa       sfo      offa      offo    dattyp
         5         0  1.000000  1.000000
```

```
$#                 a1                  o1
                    …
                    …

*DEFINE_CURVE
$HMNAME CURVES      10net axial load
$HWCOLOR CURVES      10       8
$HMCURVE     1    1 net axial load
$#    lcid      sidr       sfa       sfo      offa      offo    dattyp
        10         0  1.000000  1.000000
$#                 a1                  o1
                    …
                    …

*DEFINE_CURVE
$HMNAME CURVES
$HWCOLOR CURVES      12       8
$HMCURVE     1    1 net axial load
$#    lcid      sidr       sfa       sfo      offa      offo    dattyp
        12         0  1.000000  1.000000
$#                 a1                  o1
                    …
                    …
*SET_NODE_LIST
$$
$$ Sets Defined In HyperMesh
$$
$HMSET
$HMNAME SETS       6all nodes
$#     sid       da1       da2       da3       da4
         6
$#    nid1      nid2      nid3      nid4      nid5      nid6      nid7
nid8
   1025865   1025864   1025863   1025862   1025861   1025860   1025859
1025858

*SET_PART_LIST
$HMSET
$HMNAME SETS       5all rotating
$#     sid       da1       da2       da3       da4
         5
$#    pid1      pid2      pid3      pid4      pid5      pid6      pid7
pid8
         5        12

*ELEMENT_SOLID
$#   eid     pid      n1      n2      n3      n4      n5      n6      n7
n8
  723978      10  939331  939333  939332  939330  939334  939337  939336
939335 ...................................................
```

```
*SET_PART_LIST
$HMSET
$HMNAME SETS       5all rotating
$#     sid       da1       da2       da3       da4
         5
$#    pid1      pid2      pid3      pid4      pid5      pid6      pid7
pid8
         5        12

*ELEMENT_SOLID
$#   eid     pid      n1      n2      n3      n4      n5      n6      n7
n8
  723978      10  939331  939333  939332  939330  939334  939337  939336
939335...................................................


*NODE
$#   nid               x               y               z      tc      rc
  ..................................................
*END
```

A.4 Structural analysis partial input key file:

Blade to vane interaction

```
*KEYWORD  90000000
*TITLE
LS-DYNA keyword deck by LS-Prepost

*CONTROL_TERMINATION
$$  ENDTIM    ENDCYC     DTMIN    ENDENG    ENDMAS
      0.05

*CONTROL_HOURGLASS
$$     IHQ        QH
         6       0.1

*CONTROL_BULK_VISCOSITY
$$      Q1        Q2       IBQ
       1.5      0.06        -2

*CONTROL_DYNAMIC_RELAXATION
$$  NRCYCK     DRTOL    DRFCTR    DRTERM    TSSFDR    IRELAL     EDTTL
IDRFLG
       2501.0000E-03       0.9       0.0       0.0         1      0.04
1

*CONTROL_PARALLEL
$$    NCPU    NUMRHS      ACCU
         4         0         2         0

*CONTROL_OUTPUT
$$   NPOPT    NEECHO    NREFUP    IACCOP     OPIFS    IPNINT    IKEDIT


*CONTROL_ENERGY
$$    HGEN      RWEN    SLNTEN     RYLEN
         2         2         2         2

*CONTROL_ACCURACY
$$ OSU           INN    PIDOSU
         1                   0

$$DATABASE_OPTION -- Control Cards for ASCII output
*DATABASE_GLSTAT
1.0000E-05         1
*DATABASE_MATSUM
1.0000E-04         1
*DATABASE_NCFORC
1.0000E-04         1
*DATABASE_RCFORC
1.0000E-04         1
*DATABASE_SLEOUT
1.0000E-04         1
*DATABASE_BINARY_D3PLOT
$$ DT/CYCL      LCDT      BEAM     NPLTC
2.0000E-04
```

```
         0
*DATABASE_BINARY_D3DRLF
$$ DT/CYCL
       1.0
*DATABASE_BINARY_INTFOR
$$ DT/CYCL      LCID
2.0000E-05
*DATABASE_EXTENT_BINARY
$$   NEIPH     NEIPS    MAXINT    STRFLG    SIGFLG    EPSFLG    RLTFLG
ENGFLG

$$  CMPFLG    IEVERP    BEAMIP     DCOMP      SHGE     STSSZ    N3THDT
IALEMAT

$$ NINTSLD   PKP_SEN    SCLP                MSSCL     THERM
                                                 0         0

*DEFINE_COORDINATE_SYSTEM
         2       0.0       0.0       0.0       1.0       0.0       0.0
       0.0       1.0       0.0

*NODE
  301246       0.0301561      -0.0171179       0.5608974
  301249       0.0305885      -0.0183477       0.5610197
$# title
$#     pid     secid       mid     eosid      hgid      grav    adpopt
tmi
$# title
$#     pid     secid       mid     eosid      hgid      grav    adpopt
tmi
$# title
$#     pid     secid       mid     eosid      hgid      grav    adpopt
tmi
$#     mid        ro         e        pr         n    couple         m
alia
$#     cmo      con1      con2
$#lco or a1        a2        a3        v1        v2        v3

*MAT_RIGID
$HMNAME MATS       1rigid
         1    8180.01.8400E+11       0.3       0.0       0.0       0.0
      -1.0         0     11011
         0

*MAT_RIGID
$HMNAME MATS       2material rigid
         2    8180.01.8400E+11       0.3
      -1.0         0    000011
         0

*MAT_PIECEWISE_LINEAR_PLASTICITY
$HMNAME MATS       3mat24
         3    8180.01.8400E+11       0.3723000000.8.7000E+09      0.28
      7.42     19.74         0         0
$$ HM Entries in Stress-Strain Curve =         2
       0.0      0.28
723000000.1.0750E+09
```

```
*PART
NGV RIGID PART
$HMNAME COMPS      24solid ngv
$HWCOLOR COMPS      24       6
$#     pid     secid       mid
        24         1         2

NGV TIP DEFORMABLE
$HMNAME COMPS      25ngv tip
$HWCOLOR COMPS      25       7
$#     pid     secid       mid
        25         1         3

IPT BLADE TIP DEFORMABLE
$HMNAME COMPS      22tip_itp
$HWCOLOR COMPS      22      25
$#     pid     secid       mid
        22         1         3

IPT BLADE TIP RIGID
$HMNAME COMPS       9solid_ipt
$HWCOLOR COMPS       9      49
$#     pid     secid       mid
         9         1         1

*SECTION_SOLID
$HMNAME PROPS       1prop
         1         1

*INITIAL_VELOCITY_RIGID_BODY
$HMNAME LOADCOLS       1initial velocity
$HWCOLOR LOADCOLS       1      17
         9       0.0       0.0       0.0  1021.442

*INITIAL_VELOCITY_GENERATION
$HMNAME LOADCOLS       2velocity deformable
$HWCOLOR LOADCOLS       2      17
         2         1  1021.442
 -0.042034-6.821E-161.3750E-14       1.0

$$ Base Accelerations and Angular Velocities
*LOAD_BODY_RX
$HMNAME LOADCOLS       6LoadBody_6
$HWCOLOR LOADCOLS       6       3
         2       1.0           -0.042034-6.821E-161.3760E-14

*LOAD_BODY_PARTS
$HMNAME LOADCOLS       6LoadBody_6
$HWCOLOR LOADCOLS       6       3
         2

*BOUNDARY_PRESCRIBED_MOTION_RIGID
$HMNAME LOADCOLS       3rigid translation
$HWCOLOR LOADCOLS       3       8
         9         1         2         3       1.0         0
```

```
*LOAD_RIGID_BODY
         9         5         1  0.006607         0

*CONTACT_ERODING_SURFACE_TO_SURFACE_ID
$HMNAME GROUPS       3contact
$HWCOLOR GROUPS       3       6
         3
        22        25         3         3
       0.7       0.2      0.25       0.0      20.0
       0.0       0.0       0.0       0.0       0.0       0.0       0.0
0.0
         0         1         1
         2       0.1         0     1.025       0.0         2
       0.0         0         0         0         0         0       0.0
0.0
         2

*ELEMENT_SOLID
  559651      24  301256  301257  777071  777064  591480  591480  910777
910777...................................................

$$
$$ Sets Defined In HyperMesh
$$
*SET_NODE_LIST
$HMSET
$HMNAME SETS       1node
         1
    ...................................................

*SET_NODE_LIST
$HMSET
$HMNAME SETS       3only 22
         3
$$ ...................................................

$$ Sets Defined In HyperMesh
$$

*SET_PART_LIST
IPT BLADE
$HMSET
$HMNAME SETS       2deformable
         2
        22         9

*BOUNDARY_SPC_NODE
$HMNAME LOADCOLS       5LoadRigidBdy_2
$HWCOLOR LOADCOLS       5       4
    930280         0         1         1         1         1         1
1
```

```
*DEFINE_CURVE
$HMNAME CURVES       1torque
$HWCOLOR CURVES       1       5
$HMCURVE     1    2 torque
         1         0       1.0       1.0       0.0       0.0         0
                 0.0             74.1808
               0.002               73.47
*DEFINE_CURVE
$HMNAME CURVES       2dynamic relaxation
$HWCOLOR CURVES       2       3
$HMCURVE     1    3 dynamic relaxation
         2         1       1.0       1.0       0.0       0.0         0
                 0.0            1021.442
                 0.5            1021.442
*DEFINE_CURVE
$HMNAME CURVES       3axial translation
$HWCOLOR CURVES       3       3
$HMCURVE     1    1 axial translation
         3         0       1.0       1.0       0.0       0.0         0
                 0.0 1.0000000000000E-03
               0.004         0.001114648
               0.006         0.001158877
               0.008         0.001218194
*DEFINE_CURVE
$HMNAME CURVES       4axial2
$HWCOLOR CURVES       4       3
$HMCURVE     1    2 axial2
         4         0       1.0       1.0       0.0       0.0         0
                 0.0 1.0000000000000E-03
               0.004 1.0439480000000E-03
               0.006 1.0562550000000E-03
               0.008 1.0719450000000E-03
*DEFINE_CURVE
$HMNAME CURVES       5axial3
$HWCOLOR CURVES       5       4
$HMCURVE     1    3 axial3
         5         0       1.0       1.0       0.0       0.0         0
                 0.0 1.0000000000000E-03
               0.004 1.0000220000000E-03
               0.006 1.0000580000000E-03
*END
```